Fakulteit Ingenieurswese, Bou-omgewing & IT

Faculty of Engineering, Built Environment & IT

School of Engineering

Department of Materials Science and Metallurgical Engineering

NIN 890: Dissertation 890

Evaluation of HCFeMn and SiMn Slag Tapping Flow Behaviour Using Physicochemical Property Modelling and Analytical Flow Modelling

by

J. Muller

Supervisor: Prof. P.C. Pistorius
Co-supervisor: Dr. J.H. Zietsman

Date of Submission: 9 March 2015

UNIVERSITEIT VAN PRETORIA
UNIVERSITY OF PRETORIA
YUNIBESITHI YA PRETORIA

Denkleiers • Leading Minds • Dikgopolo tša Dihlalefi

ABSTRACT

The tapping of slag and metal is a key operational aspect in high-carbon ferromanganese (HCFeMn) and silicomanganese (SiMn) production. Tapping behaviour can be influenced by taphole design and the physicochemical properties of the tapped slag and metal. Unfavourable behaviour includes difficulties during taphole opening, and sluggish or intermittent slag flow. The slags of interest here consist mostly of components in the CaO-MnO-SiO_2-Al_2O_3-MgO system, but differ greatly in MnO content and basicity due to the different operating practices.

To evaluate the flow behaviour of these slags from submerged arc furnaces (SAFs) the latest physicochemical property models were applied to model viscosity, thermal conductivity, density, and heat capacity as functions of temperature and typical HCFeMn and SiMn slag compositions. These property values were applied in a simplified model of flow through the coke bed and taphole with an inlet pressure specified. Based on a model from the literature (Iida *et al.* 2008), a model was formulated with spherical-radial flow through the coke bed, being independent of the length of the fluid path through the coke bed.

The effect of variation in the slag-metal ratio was investigated, with the focus on tap streams consisting of only slag. The estimated flow rates were comparable to those reported elsewhere (Kadkhodabeigi 2011) and found to be dependent mostly on slag viscosity, which was generally lower for the typical SiMn slags due to their composition and higher operating temperature. Furthermore, in most of the cases considered it was estimated that the flow through the taphole would develop into laminar flow, with the pressure drop predominantly over the coke bed. Flow rates were found to be highly dependent on the taphole diameter and coke bed void fraction, and to lesser extent on the taphole length and coke bed particle diameter.

Keywords: taphole, high-carbon ferromanganese, silicomanganese, physicochemical properties

TABLE OF CONTENTS

LIST OF SYMBOLS

SYMBOL	DESCRIPTION	UNITS
A_W, A_E	Arrhenius and Weimann pre-exponential constants	$P.K^{-1}$
C_p	Heat capacity	$J.kg^{-1}.K^{-1}$
D	Particle diameter	m
d	Pipe (taphole) diameter	m
E	Activation energy	$J.mol^{-1}$
f	Friction factor	
H	Enthalpy	$J.kg^{-1}$
h	Height of fluid (slag, metal) above the taphole	m
K	Viscosity ratio of the dispersed phase relative to the continuous phase	
k	Thermal conductivity	$W.m^{-1}.K^{-1}$
L	Length	m
MM	Molar mass	$kg.kmol^{-1}$
M	Mass flow rate	$kg.s^{-1}$
NBO	Mole fraction of non-bridging oxygen	
P	Pressure	Pa
Q	Degree of polymerisation	
q	Heat flux	$W.m^{-2}$
R	Ideal gas constant	$J.mol^{-1}.K^{-1}$
r	Radius	m
Re_D	Reynolds number for flow in a circular duct	
T	Absolute temperature	K
TBO	Mole fraction tetragonal-bonded oxygen	
u	x-direction velocity	$m.s^{-1}$
V	Volumetric flow rate	$m^3.s^{-1}$
V_m	Molar volume	$m^3.kmol^{-1}$
w	Mass fraction	
X	Mole fraction	
x	x-direction length	m
x_e	Entry length for fully developed laminar flow	m
α	Thermal expansion coefficient	K^{-1}
Δ	Change in variable	
ε	Void fraction	
φ	Volume fraction metal	
$\emptyset$	Volume fraction solids	
φ_m	Model fitting parameter	
ρ	Density	$kg.m^{-3}$
τ	Shear stress	Pa
μ	Dynamic viscosity	Pa.s

SUBSCRIPTS

app	Referring to the apparent property value for developing laminar flow
avg	Average of property values
$continuous$	Referring to the continuous phase
$corr$	Referring to the corrected property value
$dispersed$	Referring to the dispersed phase
eff	Effective
far	Referring to some far position in relation to the taphole diameter
g	Variable value at the glass transition temperature
liq	Liquid
$metal$	Referring to the property of the metal
r, R	Relative
$mixture$	Referring to the property of the mixture
$slag$	Referring to the property of the slag
$taphole$	Referring to the taphole
$turbulent$	Referring to the property for turbulent flow

ABBREVIATIONS

ASTM	American Society for Testing and Materials
BO	Bridging oxygen
CFD	Computational fluid dynamics
FeMn	Ferromanganese
HCFeMn	High-carbon ferromanganese
LCFeMn	Low-carbon ferromanganese
LCSiMn	Low-carbon silicomanganese
MCFeMn	Medium-carbon ferromanganese
NBO	Non-bridging oxygen
NBO/TBO	Non-bridging oxygen to tetragonal-bonded oxygen
SAF	Submerged arc furnace
SG	Specific gravity
SiMn	Silicomanganese
SR	Slag ratio (effectively the fraction slag in tap stream)
TBO	Tetragonal-bonded oxygen
ULCSiMn	Ultra-low-carbon silicomanganese
VOF	Volume of fluid
2D	Two-dimensional
3D	Three-dimensional

LIST OF FIGURES

viii

LIST OF TABLES

ix

1   Introduction

1.1   Background

Manganese ferroalloys can be classified into ferromanganese (FeMn) with varying carbon contents (high, medium, and low), and silicomanganese (SiMn) (Habashi 1997). High-carbon ferromanganese (HCFeMn) and SiMn are mostly produced in submerged-arc electric furnaces (SAFs). The removal of slag from the furnace by means of tapping through a taphole is a key operational aspect. Operational difficulties can be experienced during tapping, such as difficulties during slag taphole opening and sluggish or intermittent slag flow. Tapping difficulties are compensated for by typically increasing the operating temperature, changing the slag chemistry, or lancing open tapholes. These practices cause increased refractory damage over time, as well as other adverse effects on the process and equipment.

The slags produced in the FeMn and SiMn processes differ in their chemical composition and temperature due to differences in the process and thermodynamic conditions necessary to produce these alloys. Furthermore, the qualities of the ores are expected to vary over time and with switching between different ore feeds, requiring frequent adjustment in the raw material recipes. These differences affect the process energy demand, relating back to the process operating temperatures. Depending therefore on which manganese alloy is produced, and what operating practice is followed, as well as on other possible process disturbances, the slag chemical compositions and temperatures do not remain constant.

The behaviour of material around the taphole and associated refractory sub-systems is related to the physicochemical properties of manganese-bearing slags, which are determined by the temperature and chemical composition of the slags. Slag properties such as viscosity, thermal conductivity, density and surface tension are important process variables that also influence operational aspects such as reaction kinetics, slag-metal separability, and overall process operability. The typical slags produced in FeMn and SiMn processes are described by the $CaO-MnO-SiO_2-Al_2O_3-MgO$ slag system, which comprises the major components found in the slags.

The design of the furnace refractory lining, and more specifically the tapblock, determines the flow of heat from the tapped slag and in turn the temperature profile in the tapstream. Typical lining and taphole refractory configurations are used in the production of manganese ferroalloys. A typical taphole configuration is the insulating type, where ceramic refractories are utilized with low thermal conductivity that limits heat losses (Brun 1982). Carbon-based refractories with high thermal conductivities, which result in a high heat flux that promotes the formation of protective freeze linings, have been adopted in recent times (Hearn *et al.* 1998). Configurations also exist where ceramic refractories are used in the majority of the furnace, in conjunction with a carbon tapblock.

1

1.2 Key questions

This research aimed to answer the following key questions:

1. What are the primary factors affecting tapped slag flow rate in the processes producing HCFeMn and SiMn slags at the typical process conditions (e.g. slag chemical composition, temperature, refractory design, production practices)?

2. What are the sensitivities of the relevant important slag physicochemical properties to variations in chemical composition and temperature, and what are the differences for the processes producing HCFeMn and SiMn when considering typical chemical compositions and temperatures?

3. Can tapping flow rates be modelled utilizing knowledge of the relevant measurable parameters, and estimations of model parameters that are difficult to measure?

4. How is tapping flow affected by variations in model parameters representing the primary factors, and what are the differences for the processes producing HCFeMn and SiMn when considering the typical operating conditions of each?

1.3 Research outline

To address the identified key questions, the following aspects have been researched, and form the outline of this thesis:

1. Introduction to this study, providing the definition and background.

2. Literature review of the production of manganese alloys (HCFeMn, SiMn) in SAFs, tapping flow modelling, and slag physicochemical property modelling.

3. Modelling of slag physicochemical properties for typical HCFeMn and SiMn slags identified, formulating the metallurgical system and applying models from the literature. Slag properties evaluated are solidus and liquidus temperatures, viscosity, thermal conductivity, density, and heat capacity. Results for varying temperature and chemical compositions are provided in the form of graphs (as functions of temperature and basicity) and pseudo-ternary diagrams. Results include a set of physicochemical properties of the HCFeMn and SiMn slags considered at the typical process temperatures, used later in tapping flow modelling.

4. An analytical tapping flow model from literature is applied that models flow through a coke bed and taphole of a blast furnace, given a total pressure drop. An improved tapping flow model is formulated, making corrections to the model from the literature, and replacing the linear flow through the coke bed with a spherical-radial flow model. Model parameters are changed to resemble typical SAF conditions. Model parameters are varied to evaluate tapping flow and study the effect of slag fraction in the tapstream, variation in coke bed particle properties, and variation in taphole dimensions.

2

2 Literature review

2.1 Production of manganese alloys

2.1.1 Overview

Manganese (Mn) is an element abundant in the earth's crust, found in nature as minerals containing various Mn oxides and other compounds, including hydroxides, carbonates, etc. Manganese-bearing ore is transformed into manganese alloys through carbothermic reduction. The major use of manganese alloys is in steel production. Of this, the majority is added as an alloying component to increase the toughness, strength, and hardness of the steel. Manganese is also used as an additive in steelmaking to remove unwanted oxygen and sulphur from crude steel (Olsen *et al.* 2007). Of the manganese alloys produced, 90% is used in the steelmaking industry, with the other 10% in the battery and chemicals industries, and as additions to copper and aluminium alloys (Habashi 1997).

Steels with various grades are produced that require different amounts of manganese to be added, and therefore different grades of manganese alloys are produced. Mn alloys are classified as ferromanganese (FeMn), containing low percentages of silicon, and silicomanganese (SiMn). Each of these Mn alloys can be produced with varying carbon contents, classified into high-carbon (HC), medium-carbon (MC), low-carbon (LC), and ultra-low-carbon (ULC) FeMn or SiMn. The standard specifications for these manganese alloys are summarised in Table 1 (ASTM 1999).

Table 1 ASTM standard specification for ferromanganese (A99-82) and silicomanganese (A483-64) alloys (ASTM 1999).

	Grades	Chemical composition (wt.%)				
		Mn	C (max.)	Si (max.)	P (max.)	S (max.)
HCFeMn	Grade A	78–82	7.5	1.2	0.35	0.05
	Grade B	76–78	7.5	1.2	0.35	0.05
	Grade C	74–76	7.5	1.2	0.35	0.05
MCFeMn	Grade A	80–85	1.5	1.5	0.3	0.02
	Grade B	80–85	1.5	1.0	0.3	0.02
	Grade C	80–85	1.5	0.7	0.3	0.02
	Grade D	80–85	1.5	0.35	0.3	0.02
LCFeMn	Grade A	85–90		2.0	0.2	0.02
	Grade B	80–85	0.75	5.0–7.0	0.3	0.02
SiMn	Grade A	65–68	1.5	18.5–21.0	0.2	0.04
	Grade B	65–68	2.0	16.0–18.5	0.2	0.04
	Grade C	65–68	3.0	12.5–16.0	0.2	0.04

2.1.2 Production processes and practices

Manganese alloys are produced by the carbothermic reduction of manganese-oxide-bearing ores using carbonaceous reductants (typically coke) and fluxes, with silica also being added to produce SiMn. HCFeMn is converted through oxygen blowing to MCFeMn, and MCSiMn is converted to LCSiMn. FeMn and SiMn are produced mostly in electric furnaces, and in some cases FeMn is still produced in blast furnaces (Habashi 1997). The advantages of electric furnaces over blast furnaces for the

3

production of manganese include lower coke consumption (some of the energy requirement being supplied by electricity), increased tolerance to lower coke qualities (up to 70% coal is used in South Africa), lower dust losses, and more flexibility in producing different alloy grades (Habashi 1997). It is also reported that electric furnaces can be used for producing either FeMn or SiMn interchangeably (Olsen *et al.* 2007).

Discard Slag Practice:
(Basic slag operation)

Mn ores
Basic fluxes (CaO,MgO) → HCFeMn Electric Furnace → Slag: 15-20% MnO
Coke
Electricity → HCFeMn
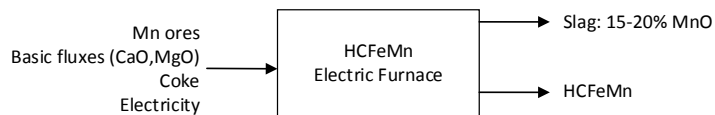
High-MnO Slag Practice:
(Duplex operation)

Silica
Coke
Ore
Electricity

Mn ores
Basic fluxes (CaO,MgO) → HCFeMn Electric Furnace → Slag: 30-50% MnO → SiMn Electric Furnace → Slag: 5% MnO
Coke
Electricity

HCFeMn ↓   MCSiMn ↓

Metal Oxygen Refining   Ladle Refining

MCFeMn ↓   LCSiMn ↓
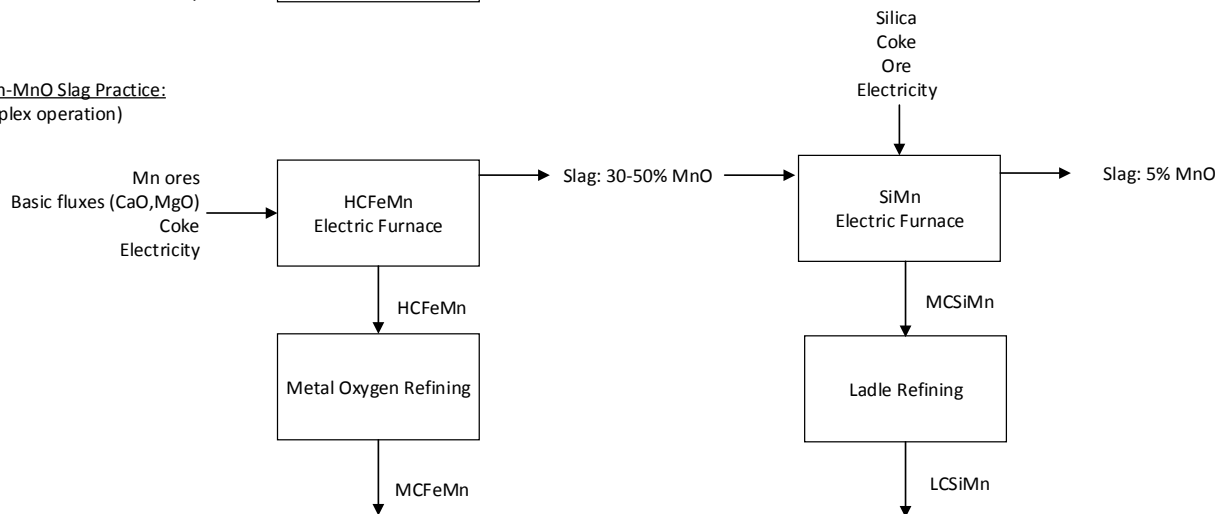
Figure 1 Overview of typical process routes for producing HCFeMn, MCFeMn, and SiMn according to the discard or high-MnO slag practices (Olsen *et al.* 2007).

In the production of HCFeMn in SAFs, two practices are followed, the discard slag practice and the high-MnO slag practice (Olsen *et al.* 2007) as illustrated in Figure 1. In the discard slag practice, HCFeMn and SiMn alloys are produced from ores and reductants with a slag containing 15 to 20% MnO in the case of HCFeMn and 9% MnO in the case of SiMn. The slag, with its low MnO contents, is discarded onto slag dumps. This practice, which is also called the basic slag operation, requires basic fluxes (CaO, MgO) to be added to the feed to increase the slag basicity. In South Africa both HCFeMn and SiMn are produced by smelting ores and reductants in SAFs following the discard slag practice. Manganese recoveries are typically around 80%, with the balance of the manganese units lost in the slag and in fumes reporting to the offgas.

In countries other than South Africa the slag from the HCFeMn processes contains typically 30 to 50% MnO. In the high-MnO slag practice this slag is used as primary feedstock together with ores, reductants, quartz, and other fluxes to produce SiMn, also in SAFs (Olsen *et al.* 2007). The final slag from the SiMn production contains only around 5% MnO, and increased overall recoveries of 85 to 90% are achieved. This practice uses less coke and fluxes than the discard slag practice.

4

2.1.3 Ferromanganese production

FeMn is produced in electric furnaces with power ratings typically ranging from 75 to 90 MVA. The furnaces used are mostly circular with diameters from 2 to 20 m, and have three electrodes, each of which is coupled to a separate electrical phase (Habashi 1997). To produce FeMn, manganese-bearing ores are continuously fed with coke and basic fluxes into the furnaces. The ores used vary in chemical composition, with blending ratios adjusted according to their Mn/Fe ratios in order to obtain an alloy product of the desired manganese grade.

Typical design parameters of such furnaces are summarised in Table 2. The burden resistivity is low in the production of FeMn, and low voltages and high currents are therefore required to obtain sufficient electrode penetration. To limit process temperatures and metal vapourisation, electrode current densities are decreased through the use of larger diameter electrodes. Furnaces in which specifically FeMn is produced are reported to be larger compared to other ferroalloy furnaces, to accommodate the required larger electrodes (Habashi 1997).

Table 2 Summary of typical design parameters of furnaces producing manganese alloys (Habashi 1997).

Furnace	Units	Elkem Sauda	Temco Bellbay	Samancor Meyerton M10	Samancor Meyerton M4
Inside shell diameter	m	12.5	10	16	9.8
Shell height	m	6	5.2	8	5.7
Electrode diameter	m	1.9	1.4	1.9	1.2
Tapholes		1 slag, 2 metal	1 slag, 2 metal	1 slag, 2 metal	1 slag, 2 metal
Power input rating	MW	30	13	46	20

Several important chemical reactions occur to produce the FeMn alloy as material moves downward in the electric furnace. Around mid-way in the furnace the highly endothermic Boudouard reaction occurs where carbon from the coke bed zone reacts with CO_2 gas to produce CO according to Equation [1] (Olsen *et al.* 2007). This reaction occurs from approximately 800°C, and its extent influences the carbon and electrical energy requirements.

$$C(s) + CO_2(\text{g}) = 2CO(g) \qquad [1]$$

Higher oxides of manganese that enter the furnace dissociate in the presences of CO gas at temperatures above 981°C (Olsen *et al.* 2007):

$$2MnO_2(s) = Mn_2O_3(s) + \frac{1}{2}O_2(g) \qquad [2]$$

$$6Mn_2O_3(s) = 4Mn_3O_4(s) + O_2(g) \qquad [3]$$

5
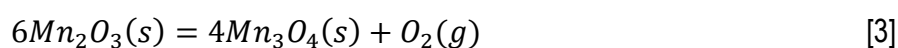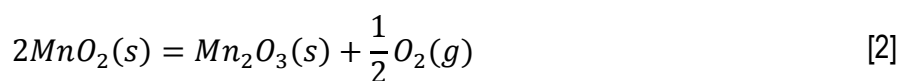
The higher oxides are pre-reduced by CO to Mn_3O_4 and MnO, with these exothermic reduction reactions releasing energy that heats the charged materials. These heterogeneous reactions occur in the pre-reduction zone where higher oxides (solid) react with CO gas from the coke bed (Olsen *et al.* 2007).

$$2MnO_2(s) + CO(g) = Mn_2O_3(s) + CO_2(g) \qquad [4]$$

$$3Mn_2O_3(s) + CO(g) = 2Mn_3O_4(s) + CO_2(g) \qquad [5]$$

$$Mn_3O_4(s) + CO(g) = 3MnO(s) + CO_2(g) \qquad [6]$$
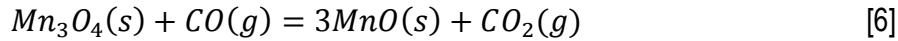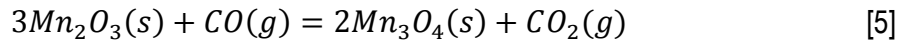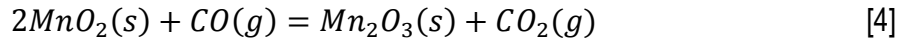
The coke bed zone is situated lower in the furnace, starting slightly below the tips of the electrodes (Olsen *et al.* 2007). In this zone the ores and fluxes (limestone, dolomite) start to melt together while carbon remains solid, with temperatures increasing to above 1250 to 1300°C. Here, reduction of MnO dissolved in the slag phase in contact with solid carbon occurs. Electrical energy supplied to the furnace through the electrodes provides for the energy demand, including losses, the energy required for heating and melting, and this highly endothermic reduction reaction:

$$MnO(l) + C(s) = Mn(l) + CO(g) \qquad [7]$$
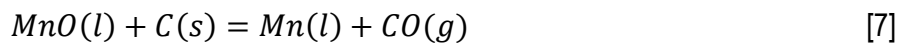
The hot gases from the above reactions are rich in CO and exit at the top of the furnace at approximately 290°C (Habashi 1997). These gases are cleaned in cyclones and venturi scrubbers, and some energy can be recovered as electricity. In the case of open furnaces, gases are withdrawn with fans and cleaned in bag filter systems. This causes the gas to be mixed with air in the open part of the furnace to fully combust.

The ores also introduce SiO_2 and Al_2O_3, and some CaO and MgO, into the process. These components report mostly to the slag. The ash from the coke consists mostly of SiO_2 and Al_2O_3, while the fluxes can contribute CaO and MgO, and possibly SiO_2 in cases where the basicity has to be decreased. The slag chemical composition, expressed in term of its basicity, is dependent on the amounts of major components (CaO, MgO, Al_2O_3, and SiO_2) in the ores and fluxes. The slag MnO content depends on the degree of reduction, and is strongly dependent on process temperature, which relates directly to the overall process efficiency. Slag basicity influences the process by affecting the slag liquidus temperature and the slag MnO activity, which influences the resulting fraction of MnO in the slag (Olsen *et al.* 2007). Depending on the production practice, a specific MnO content would be aimed for.

The amount of slag produced per ton of FeMn can vary between 500 to 1000 kg, with tap temperatures typically between 1400 to 1500°C. The temperature of the metal is around 50°C lower than that of the slag (Olsen *et al.* 2007).

6

Typical plant process data from HCFeMn-producing SAFs is summarised in Table 3, provided by Olsen *et al.* (2007). Plants A and B use the high-MnO slag practice, operated with slag MnO contents above 40%. Plant C follows the discard slag practice where a slag MnO content of 14.3% is achieved. This is also reflected in the recoveries reported, with plant C obtaining the higher recovery of 91.4%. It does not, however, consider overall recoveries, with the slags from plant A and B used further in the production of SiMn, thus increasing the overall manganese recovery. The slag basicities, as calculated as a function of the major slag components, also differ. Plant A is operated with a very high-basicity slag, while plant C has an intermediate basicity, and plant B a very low basicity. In the latter case, acidic Comilog ores and sintered fines were used with no fluxes, resulting in a very low slag basicity.

Table 3 Typical operating parameter values of plants producing HCFeMn in SAFs (Olsen *et al.* 2007).

Parameter	Units	Plant A	Plant B	Plant C
Furnace load	MW	30	33.3	
Operating time	%	98%	98.9%	
Alloy production	$t.d^{-1}$	294	395.5	
Slag production	$kg.t^{-1}$ alloy	640		660
Specific energy consumption	$kWh.t^{-1}$ alloy	2400	2152	3395
Fixed carbon	$kg.t^{-1}$ alloy	360	306	
Electrode consumption	$kg.t^{-1}$ alloy	12	6.6	
Mn recovery (saleable)	%	76.7%	81.5%	91.4%
Metal composition (%'s)	Mn	78.8	78.7	
	Fe	13.2	12.7	
	C	7	6.7	
	Si	0.04	0.8	0.8
	P	0.16	0.19	
Slag composition (%'s)	MnO	40.3	42.7	14.3
	SiO_2	22.8	18.3	22.7
	Al_2O_3	12.5	28.2	19.6
	CaO	16.7	2.8	32.5
	MgO	6.3	0.98	5.4
	BaO	1.1	1.2	2.6
	K2O		3.3	
	Basicity*	1.79	1.0	1.23

* Basicity = $(CaO+MgO+MnO)/(Al_2O_3+SiO_2)$

2.1.4 Silicomanganese production

SiMn is produced in electric furnaces by carbothermic reduction, similar to FeMn. Unlike FeMn, blast furnaces are not used to produce SiMn. The furnaces used range between 15 and 40 MVA, and typically produce 80 to 220 tons of alloy per day (Olsen *et al.* 2007). In some cases only manganese ores are used, but the SiMn production process often forms part of the high-MnO HCFeMn production practice, where the slag is used as feed together with manganese ores, silica, and coke (Figure 1).

The SiMn process also differs from FeMn in that higher operating temperatures are necessary to achieve the required degree of silicon reduction (Olsen *et al.* 2007). To achieve levels of 20% silicon in

7

the alloy, temperatures of between 1600 and 1650°C are required, due to SiO_2 being more stable than MnO in the slag. This is also necessary to achieve the low levels of MnO in the slag that are required for it to be discarded. The power input required is higher, between 3500 and 4500 kWh.t^{-1} alloy. This is the result of higher slag volumes and the alloy silicon content.

In the SiMn process, the higher manganese oxides are also pre-reduced with CO in the pre-reduction zone (Equations [4], [5], and [6]), while CO gas is produced in the coke bed zone through the Boudouard reaction (Equation [1]). Temperatures increase above 1600°C in the coke bed zone, and the reduction of the molten mixture containing MnO proceeds according to Equation [7]. Reduction of SiO_2 proceeds according to the overall reaction in Equation [8], producing silicon in the metal phase (Olsen *et al.* 2007).

$$SiO_2(l) + 2C(s) = Si(l) + 2CO(g) \hspace{3cm} [8]$$
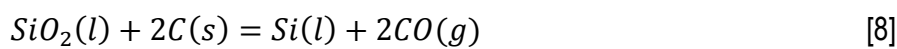
At silicon concentrations above 18%, graphite is replaced as the stable phase in the alloy by silicon carbide, SiC, and SiO_2 is reduced according to Equation [9] (Olsen *et al.* 2007):

$$SiO_2(l) + 2SiC(s) = 3Si(l) + 2CO(g) \hspace{3cm} [9]$$
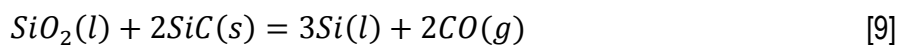
The reduction of SiO_2 (Equations [8] and [9]) also involves the formation and consumption of gaseous SiO, due to SiO_2 in the slag phase reacting with metallic Si or carbon (Olsen *et al.* 2007).

The reduction of SiO_2 by Mn in the alloy also occurs according to Equation [10], which proceeds faster than the reduction of MnO and SiO_2 by carbon (Equations [7] and [8]). As a result, a partial slag-metal equilibrium is established and the net reduction rates are limited by the carbothermic reduction reactions (Olsen *et al.* 2007).

$$SiO_2(l) + 2Mn(l) = Si(l) + 2MnO(l) \hspace{3cm} [10]$$
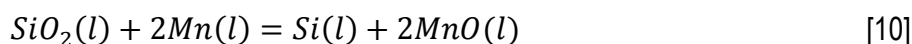
The slag chemistry and temperature determine the extent to which SiO_2 and MnO are reduced to the alloy, and it is reported that increased CaO contents negatively affect the silicon content of the alloy (Habashi 1997).

Between 1000 to 1500 kg of slag is produced per ton of SiMn, with tap temperatures typically between 1550 to 1650°C. The temperature of the metal is around 50°C lower than that of the slag (Olsen *et al.* 2007).

Typical plant process data from a SiMn-producing SAF is summarised in Table 4, provided by Olsen *et al.* (2007). In this operation specifically, HCFeMn slag is used as primary feedstock, with manganese ore, coke, silica (as quartz), dolomite, and recycled SiMn metal skulls. A significantly greater amount of

8

slag is produced, and the specific energy consumption is higher, compared to typical HCFeMn furnaces (Table 3). The slag includes approximately 2% by mass of entrained alloy.

Table 4 Typical operating parameter values of a plant producing SiMn (Olsen *et al.* 2007).

Parameter	Units	Plant A
Furnace load	MW	27
Operating time	%	99%
Alloy production	$t.d^{-1}$	175
Slag production	$kg.t^{-1}$ alloy	1225
Specific energy consumption	$kWh.t^{-1}$ alloy	3500
Coke consumption	$kg.t^{-1}$ alloy	360
Electrode consumption	$kg.t^{-1}$ alloy	30
Mn recovery (saleable)	%	88%
Metal composition (%'s)	Mn	70.5
	Fe	8.1
	C	1.5
	Si	19.2
	P	0.05
Slag composition (%'s)	MnO	8.1
	SiO_2	43.3
	Al_2O_3	15.0
	CaO	20.2
	MgO	8.6
	Basicity*	0.64

* Basicity = $(CaO+MgO+MnO)/(Al_2O_3+SiO_2)$

2.1.5 Furnace tapping

Metal and slag have to be tapped on a regular basis from SAFs producing HCFeMn and SiMn. Tapholes are located in the sidewalls towards the bottom of these furnaces, and are typically located at an offset angle of 60° relative to each other. These tapholes are used for tapping both slag and metal (Habashi 1997). Some furnaces have separate tapholes for slag and metal, with the slag tapholes 0.5 to 1 m above the metal tapholes (Olsen *et al.* 2007). This assists with the separation of the slag and metal, particularly in larger furnaces, but intermixing always occurs to some extent during the tapping process. Typically, two metal tapholes are installed (Table 2) and are used alternately, thus extending the lining life.

Drills and mud guns are typically used to open and close tapholes (Mølnås 2011). In cases where drilling is not available, or difficulty is experienced with drilling open the hole, oxygen lancing is used. Lancing has a more destructive effect on the refractory material around the taphole, exposing it to higher temperatures than it would normally be subjected to by contact with the tapstream.

Although slag and alloy are produced continuously, both HCFeMn and SiMn furnaces are tapped intermittently at regular intervals of typically 2 to 3 hours, with taps lasting for 20 to 40 minutes (Mølnås 2011). Typical amounts of alloy tapped are 30 to 50 tons of HCFeMn, and 10 to 30 tons of SiMn (Olsen

9

et al. 2007). Using the operational data of HCFeMn and SiMn furnaces (Table 3 and Table 4), average slag and metal tapping rates are estimated and presented in Table 5. Tapping rates were estimated by assuming a typical tap time of 20 minutes and a taphole diameter of 100 mm.

Table 5 Derivation of expected slag and metal flow rates and velocities using typical industrial slag production data (Table 3 and Table 4).

Parameter	Units	HCFeMn, high-MnO slag		SiMn
Furnace power	MW	30	33.3	27
Alloy production	$t.d^{-1}$	294	395.5	175
Slag rate	$kg\ slag.t^{-1}$ alloy	640	640	1225
Alloy produced in 2 hours	t alloy	24.5	33.0	14.6
Slag produced in 2 hours	t slag	15.7	21.1	17.9
Alloy density	$kg.m^{-3}$	5612	5612	4449
Slag density	$kg.m^{-3}$	3300	3300	2700
Alloy tapping mass flow rate (20 minute tap time)	$kg.s^{-1}$	20.4	27.5	12.2
Slag tapping mass flow rate (20 minute tap time)	$kg.s^{-1}$	13.1	17.6	14.9
Total tapping mass flow rate	$kg.s^{-1}$	33.5	45.0	27.0
Alloy volumetric tapping rate (20 minute tap time)	$m^3.s^{-1}$	0.0036	0.0049	0.0027
Slag volumetric tapping rate (20 minute tap time)	$m^3.s^{-1}$	0.0040	0.0053	0.0055
Total volumetric tapping rate	$m^3.s^{-1}$	0.0076	0.0102	0.0082
Average volume fraction slag		0.52	0.52	0.67
Alloy velocity (100 mm taphole)	$m.s^{-1}$	0.463	0.623	0.348
Slag velocity (100 mm taphole)	$m.s^{-1}$	0.504	0.678	0.702
Total fluid velocity (100 mm taphole)	$m.s^{-1}$	0.967	1.301	1.050

After tapping, slag and metal have to be separated, either because a single taphole is used or due to intermixing of slag and metal resulting from tapping through separate tapholes (Olsen *et al.* 2007). Post-taphole separation is achieved by exploiting the density difference between slag and metal, similar to the separation that occurs inside the furnace. One option is to use a skimmer plate to force the slag and metal to flow in different directions. Alternatively, cascade tapping is applied where the tapstream flows into a metal ladle, and the slag then overflows into multiple slag pots. Slag remaining in the metal ladle is manually removed after tapping.

2.1.6   Furnace refractory linings

The furnace refractory lining is a major component of the furnace assembly. The maximisation of its lifetime is crucial for the overall process performance in terms of productivity and profitability. Great effort is put into the material selection, design, and installation of furnace refractory linings to ensure that the lining provides acceptable performance under conditions causing thermal, chemical, and mechanical wear (Olsen *et al.* 2007). Other internal aspects that must also be considered include the accommodation of thermal stresses, thermal expansion, and differential movement (Hearn *et al.* 1998). Compared to the production of iron, manganese ferroalloy production requires more specialised refractory systems, due mainly to the higher operating temperatures (Brun 1982). Important refractory

sections of the furnace that have to be considered includes the furnace roof, sidewalls, tapblock area, and hearth. Unique conditions in each of these sections have to be considered in the design and operation of the refractories used here.

Manganese ferroalloy furnaces are operated with different types and combinations of refractories, including carbon blocks, ceramics, and carbon-based pastes (Hearn *et al.* 1998). The ceramics that have been used include silicon carbide, fire clay, alumina, and magnesia (Brun 1982). Lining designs have evolved over the years, and can be classified as being either of the "insulating" type or of the "conductive" type (Hearn *et al.* 1998).

With "insulating" linings, ceramic refractories are used that have lower thermal conductivities, limiting heat losses from the furnace. In processes where the metal is close to carbon saturation, a combination of carbon- and ceramic-based refractory linings is applied (Olsen *et al.* 2007). Carbon blocks or carbon-based ramming paste are used on the inside of the furnace below some distance above the maximum slag level. Ceramic refractories are used behind these carbon linings, extending up to the roof.

The refractory layout of a typical "insulating" lining is shown on the left-hand side of Figure 2 (De Kievit *et al.* 2004). The sidewall and floor are composed primarily of 55% Al_2O_3 andalusite ceramic refractory bricks. Around the tapblock area, silicon carbide refractories are used, with the floor filled with a hearth paste. In this case the tapblock itself is a carbon block.
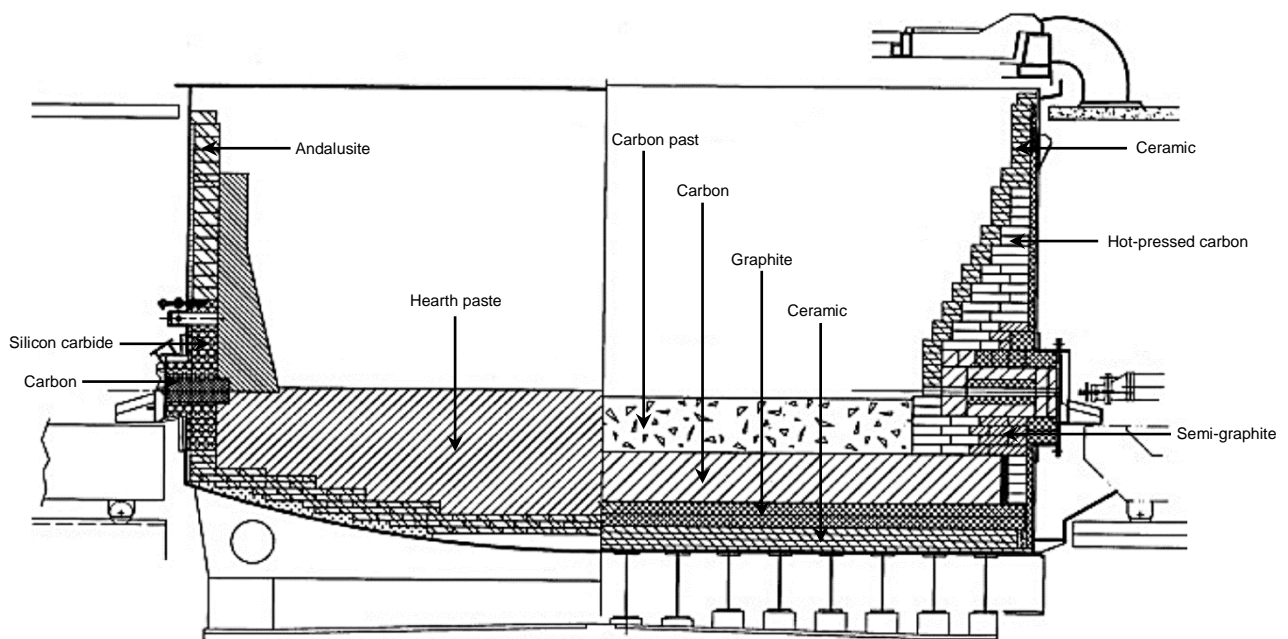
Figure 2 Furnace cross-sections around the tapblock area showing a typical "insulating" layout on the left, and a "conductive" lining layout on the right (De Kievit *et al.* 2004).

"Conductive" linings, which are a more recent development, utilise graphite and hot-pressed carbon refractories throughout the lining (Hearn *et al.* 1998). These carbon-based materials have significantly higher thermal conductivities than ceramic-based refractories, and these designs are combined with

11

effective cooling of the furnace exterior. This results in hot-face temperatures around the slag layer that are below the slag liquidus temperatures, causing slag to "freeze" and form a protective layer on the inside layer of ceramic refractories, which lowers the heat losses in this area. In operation an equilibrium is reached with regard to wear of the refractory at the slag-wall interface, which is not possible with "insulating" type of linings. The lower temperatures also inhibit the temperature-dependent chemical reactions, preventing chemical attack of the refractories. The "conductive" lining concept has been successfully applied to both HCFeMn and SiMn furnaces (Hearn *et al.* 1998).

The refractory layout of a typical "conductive" lining is are shown on the right-hand side of Figure 2 (De Kievit *et al.* 2004), and also in Figure 3 (Duncanson and Toth 2004). Both figures show hot-pressed carbon blocks installed between the hot-face ceramic layer and a graphite refractory layer on the inside of the steel shell. Figure 2 also shows that the tapblock area is different from the rest of the sidewall lining, with a combination of graphite and carbon of different grades applied.
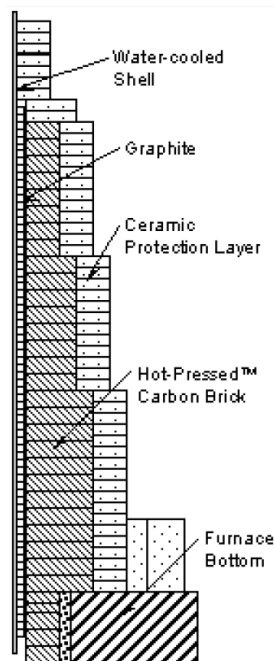
Figure 3 Sidewall cross section of "conductive" refractory lining (Duncanson and Toth 2004).

2.2   Furnace tapping modelling

Literature on the modelling of tapping from HCFeMn and SiMn SAFs is scarce, although several studies are reported for iron-producing blast furnaces. Some of the literature deemed relevant is discussed below. Table 6 summarises the furnace and commodity, the methodologies followed, and the most important findings for each of these studies.

Nishioka et al. (2005):

The drainage rate of a slag and iron mixture was modelled over time using a pressure drop equation with an assumed friction factor and the transient in-furnace pressure as inlet boundary condition, which

12

was simulated with a comprehensive 3D CFD model of the blast furnace hearth. The effect of the packed bed coke particle diameter on the iron flow was included. Slag and iron were treated as a fully dispersed mixture, with density and viscosity as the means of those of the individual liquids. From plant measurements and model estimations it was concluded that the taphole condition is the dominant factor in determining the drainage rates, with flow rate increasing as the taphole wears from tapping. The drainage rate was found to be less dependent on decreasing taphole length and taphole surface roughness. It was also concluded that the packed bed coke particle diameter at the taphole hot-face strongly influences the residual amounts of slag and iron, with an increase in the packed bed coke particle diameter resulting in lesser slag residual amounts and greater metal residual amounts. It was ultimately concluded that to minimize residual slag amounts, the drainage rate should be optimized by controlling the taphole condition by utilizing a mud with a lower wear rate, as it is not possible to control the coke particle diameter to influence flow rate. It was proposed to control the taphole condition to obtain higher initial drainage rates that increase less rapidly during the tap, as opposed to lower initial drain rates that increase rapidly due to the clay having a higher wear rate.

Desai and Lenka (2007):

To simulate tapping from a blast furnace, a physical model was set up on a 1:10 scale using water as fluid and non-wettable Thermocol (polystyrene) balls to simulate the packed coke bed. A convex fluid top surface was observed, with increasing taphole length causing the liquid top surface to be brought down, gas blow-out to be delayed, and decreasing residual fluid amounts. Blast pressure (simulated with compressed air) and the initial fluid height were found to affect the initial tapping rate, but the residual fluid amounts were not affected as the final surface shapes remained unchanged. Compared to the work by Nishioka *et al.* (2005), where it was concluded that the residual ratios can be controlled by taphole diameter, Desai and Lenka (2007) showed the residual ratio to be more dependent on taphole length or angle.

Iida *et al*. (2008):

This study was aimed at identifying dominant factors that control drainage rate and explaining the influence of hearth temperature on tapping times, in addition to variations in taphole diameter. The influence of blast furnace hearth temperature and variation in the permeability of the packed coke bed were considered in conjunction with taphole length and diameter in order to model the transient drainage rate behaviour from an iron blast furnace taphole. This work followed that by Nishioka *et al.* (2005), and argued that hearth temperatures are observed to influence tapping times and need to be considered. The transient drainage rate behaviour was subsequently modelled with a pressure drop equation representing the fluid path through the packed coke bed and taphole, assuming the blast pressure only as boundary condition at the start of the fluid path. The changes in coke particle diameter

13

and void fraction were estimated over time, considering dissolution into the metal (driven by the actual and saturation carbon content in metal) and the reaction with FeO in slag (driven by slag temperature). Taphole enlargement rate due to wear was also included as a model parameter, and was determined by calibrating the model results with actual plant data. Slag and iron were treated as a fully dispersed mixture, with density and viscosity as the means of the individual liquids. The model results indicated that the degree of carbon saturation in the metal controls the drainage rate, which can therefore be linked to the hearth temperature. At higher hearth temperatures, carbon solubility increases and the low-permeability zone is expected to decrease, resulting in a higher metal bath level and a longer metal path and travelling time to the taphole. This leads to a higher level of carbon saturation and therefore less consumption of the packed coke bed, in which case the coke permeability and subsequent tapping rate would not notably increase, as opposed to lower hearth temperatures.

Leu (2010):

The phenomena investigated were the initial metal tapping and delayed slag tapping from a blast furnace where gas would blow out of the taphole while the slag-metal interface was above the taphole. A 3D CFD model was developed that included gas, slag, and metal. The results indicated that the fluid distribution and gas blowing out of the taphole can be estimated even when the slag-metal interface is above the level of the taphole, and that the slag delay observed on actual furnaces can be accurately estimated. These observations were confirmed with a physical water model incorporating a controlled pressure drop, in which gas would be entrained in the drained water through the taphole while the water level was still above the taphole level.

Kadkhodabeigi *et al.* (2010):

A 3D CFD model was developed of tapping a SAF producing ferrosilicon, which included multiphase flow of gas and slag through porous media and used the volume of fluid (VOF) methodology to track the gas-liquid interface. The domain was divided into zones representing partially reacted charge material with different permeabilities inside the furnace. These included a crater zone that forms around the tip of an electrode, which has a specific pressure and is filled with metal up to a certain height.

The model results confirmed the direct relationship between tapping rate and packed bed permeability. Results indicated that the initial tapping rate increases significantly with crater pressure, but that gas would start blowing out of the taphole sooner, resulting in higher residual amounts of metal. Good correlations were found between the modelled results and actual plant measurements of tapping times and total amounts tapped. It was, however, apparent that industrially observed variations cannot be conclusively explained by changes in the initial metal height, but are likely to be caused by variations in

crater pressure. This implies that crater pressures can then be estimated from total weights tapped alone.

Shao (2013):

More recently, a series of papers was published that reported on models incrementally developed to study slag and iron flow in the hearth bottom and taphole of a blast furnace. These models estimated taphole flow patterns and focused on how they influence hearth performance. A CFD model was developed first, based on a pressure balance and a modified turbulence model, which aimed at improving the understanding of iron flow in the furnace hearth and the effect on erosion. Fully developed turbulent flow was estimated in a relatively small region of the hearth close to the taphole, indicating that turbulence modelling needs to accommodate both high and low flow rates. A more advanced drainage model was then developed that considered the effect of taphole condition (length and diameter) on hearth performance. This model could be used to track the slag delay variations and to estimate the deadman porosity using actual tap data. The VOF method was then incorporated to estimate taphole flow patterns and the interface shape of two immiscible liquids (slag and iron), with the hearth being modelled as a finite volume that generates inlet boundary conditions. Separated flow was found to be dominant when slag and iron flow rates are comparable, and partially dispersed flow when there are larger differences in the flow rates of these two fluids. An integrated tap cycle model was developed to estimate flow rate evolution and changes in liquid levels during the tap, based on the two-fluid model and assuming fully stratified flow. Final improvements to the CFD model included the consideration of interfacial forces between the slag and metal, using the VOF method combined with the two-fluid method to estimate immiscible fluid flow in the hearth and taphole. The interfacial forces were found to significantly affect the tapping rates and the interface angle near the taphole.

Table 6 Summary of selected taphole flow modelling studies.

Reference	Furnace, commodity	Methodology	Conclusions
Nishioka *et al.* (2005)	Blast furnace, iron	- 2D model to investigate slag-iron interface shape using volume of fluid (VOF) method - validated with a physical model - 3D CFD transient model estimating slag and iron flow in furnace hearth - Pressure drop model for taphole using modelled in-furnace pressure as boundary condition, validated with plant data - Estimate slag and iron transient drain rates and end state residual ratios - Validated in 2D with a physical model, and in 3D with actual plant data - Variation in coke particle diameter of packed bed considered - Fully dispersed flow assumed with perfectly mixed slag and metal – mean values of density and viscosity assumed for slag and iron	- Taphole conditions dominant in determining drain rates – increase with taphole diameter; less dependent on taphole length and the assumed friction factor - Residual amounts of slag and iron are influenced by the coke particle diameter Smaller coke particles – more residual slag; less residual metal – residual amounts of slag and metal cannot both be decreased - Drain rate should be managed with the taphole condition (as the coke particle diameter cannot be controlled) – mud with lower wear rate should be used having a higher initial drain rate of slag and more consistent throughout tap
Desai and Lenka (2007)	Blast furnace, iron	- Physical model of blast furnace tapping on a 1:10 scale - Water as fluid and a packed bed of non-wetted Thermocol (polystyrene) balls used, assuming fully dispersed slag and metal - Downward pressure from compressed air was used to simulate blast pressure - Evaluated the effect of blast pressure, taphole length, diameter, and angle, and initial liquid height - Residual fraction of fluid was estimated - Deadman shape assumed constant	- Residual fraction of fluid decreases with taphole length, bringing down the convex fluid surface and delaying gas blow-out - Fluid residual ratio decreases with taphole angle – delayed gas blow-out; smaller effect compared to taphole length - Taphole diameter has less effect on residual ratio (compared with length and angle) - Blast pressure and initial height has no effect on residual ratio – increased initial rates but not on final surface shape

Reference	Furnace, commodity	Methodology	Conclusions
Iida *et al.* (2008)	Blast furnace, iron	- Pressure balance model developed with the fluid path including a packed coke particle layer and the taphole, estimating transient drain rates - Model estimated changes in coke particle diameter and void fraction, specifying slag FeO and metal carbon contents - Taphole enlargement rate specified as model input - Fully dispersed flow assumed with perfectly mixed slag and metal – average values of density and viscosity of slag and iron used the pressure drop equation - Mixed slag and iron drain rates and tapping times estimated - Coke filter length tuned for model to match plant data	- Larger initial taphole – shorter tap times - Tap time decreases with slag FeO content due to higher coke consumption rates and increased coke permeability - Tap time increases with metal carbon content due to lower coke consumption rates and lower coke permeability - Tap times are not significantly influenced by hearth temperature. Higher hearth temperatures are associated with the disappearance of the low permeability zone and a deeper metal bath, causing longer metal travelling times to the taphole and higher degrees of metal carbon saturation
Leu (2010)	Blast furnace, iron	- 3D CFD model developed of blast furnace tapping with gas, slag, and metal included as fluids - Model validated with a physical model (pressurized water tank) - Drag force between fluids included in model, as well as buoyancy in the volume of fluid (VOF) model	- Model estimates slag delay during tapping with gas blowing out of the taphole when the slag-metal interface is above the taphole level
Kadkhodabeigi *et al.* (2010)	SAF, silicon and ferrosilicon	- 3D CFD model developed of a SAF producing silicon and ferrosilicon - Model considers zones in the furnace and relevant permeability of porous material through which fluid is tapped - Effect of metal height and crater pressure around electrodes on the tapping rate was investigated - Model estimations compared with actual plant data	- Crater pressure causes high initial tapping rates, and also a faster decrease in the rate until gas blows out of the taphole, leading to less being tapped in total - The total weight tapped and the rate increase with initial metal height, but this has a less significant effect than crater pressure - Decreased bed permeability causes a decrease in tapping flow rate and an increase in tap time, and tapped metal yield decreases

17

Reference	Furnace, commodity	Methodology	Conclusions
Shao (2013)	Blast furnace, iron	- Deadman state and liquid levels were estimated with a model based on a force balance in hearth bottom, and also considering liquid in- and outflow rates, hearth geometry, and deadman porosity - An integrated CFD model was developed to estimate hearth iron flow and erosion due to shear stresses by considering high and low flow regimes with a modified turbulence model - An improved drainage model was developed considering the effect of taphole length and diameter on tapping rates - A two-fluid flow model was developed to estimate the flow pattern in the taphole with separated flow, coupled to a simple deadman pressure loss expression to study the taphole flow evolution and liquid levels during tapping - The two-fluid model was combined with the VOF method representing interfacial forces at the liquids interface, and extended to the hearth region and applied for the slag-iron and oil-water systems	- Relatively small regions exist with fully-developed turbulent flow near the taphole and in the coke-free zones, implying that the standard turbulence method does not properly describe hearth flow - The results from the improved drainage model correlated well with actual plant data in terms of the slag delays observed, and can be used to estimate deadman porosity - The VOF CFD model estimated mostly separated taphole flow for the cases of similar slag and iron tap rates - The integrated two-fluid model with fully stratified flow assumed estimated the evolution of liquid outflow rates and levels during tapping, which was shown to significantly affect hearth performance in terms of tapping rates and interface angle near the taphole

18

2.3 Slag physicochemical property modelling

Physicochemical properties of slags in the fully or partially liquid states are of interest here (viscosity, thermal conductivity, density, and heat capacity). These properties are dependent on the slag structure, which is determined by its chemical composition and temperature (Slag Atlas 1995). Modelling these properties requires an understanding of the structures of slags and their influence on the properties that form the basis of the modelling.

Slags and glasses are polymer rings or chains of SiO_4^{4-} tetrahedra, each consisting of four O^{2-} anions connected to a Si^{4+} cation arranged in a three-dimensional tetrahedral array (Figure 4). The O^{2-} anions shared between the SiO_4^{4-} tetrahedra are named "bridging oxygens", and cause the formation of silicate polymer chains or rings. Cations (e.g. Na^+, Ca^{2+}, Mg^{2+}, and Fe^{2+}) break up these silicate chains and decrease the degree of polymerisation, with the oxygen anions at the end of the chains (as O^-) named non-bridging oxygens (NBO), or O^{2-} when not connected to a Si ion and then named "free oxygens" (Figure 5) (Slag Atlas 1995). The bond-breaking cations of interest in this study originate from the basic oxides CaO, MgO, and MnO.
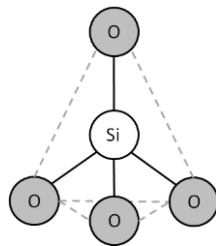
Figure 4 A single SiO_4^{4-} tetrahedron unit showing a Si^{4+} cation surrounded by four O^{2-} anions in a three-dimensional tetrahedral arrangement (Slag Atlas 1995).
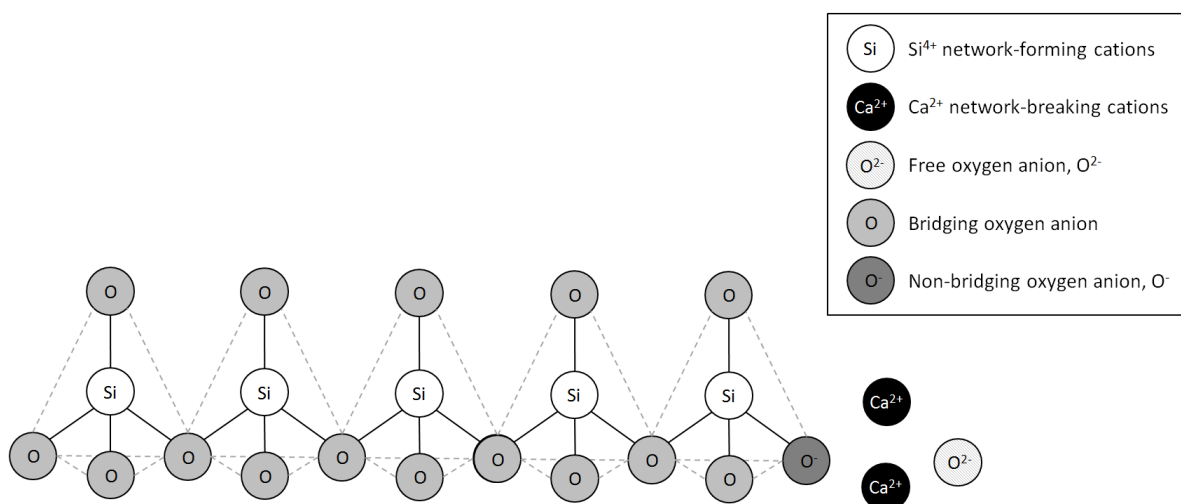
Figure 5 A single slag polymer chain composed of SiO_4^{4-} tetrahedra, showing the bridging and non-bridging O^{2-} anions linked to Si^{4+} cations formed by network-breaking cations (Ca^{2+} illustrated) (Slag Atlas 1995).

19

In FeMn and SiMn smelting the slag physicochemical properties differ, depending on the varying amounts of SiO$_2$ in relation to the basic oxides and the resulting slag structure. As an example, slag viscosity increases with the degree of polymerisation, with longer chains restricting the flow of one layer over another (Mills *et al.* 2011). Slags from FeMn and SiMn smelting differ largely in their SiO$_2$ content (Table 3, Table 4), with slags from SiMn smelting having higher SiO$_2$ contents that are thermodynamically required to produce SiMn alloy to the required specifications. The SiMn slags therefore have higher viscosities compared to those in HCFeMn production at similar temperatures. These higher slag viscosities might be largely compensated for by the higher temperature of silicomanganese production, effectively lowering the viscosity to a level where the slag has desirable flow characteristics.

Physicochemical properties are often modelled as a function of the basicity to consider the effect of polymerisation, with these parameters as derived from chemical composition included in the models. The numerical ratio of non-bridging oxygen to tetragonal-bonded oxygen (NBO/TBO) may be estimated from the molar fractions of the chemical slag constituents (Mills *et al.* 2011).

The fraction of non-bridging oxygen (NBO) is calculated:

$$NBO = 2 \left[X_{CaO} + X_{MgO} + X_{MnO} - 2X_{Al2O3} \right] \qquad [11]$$

The fraction of tetragonal-bonded oxygen (TBO) is calculated:

$$TBO = X_{SiO2} + 2X_{Al2O3} \qquad [12]$$

The degree of polymerisation (Q) is calculated:

$$Q = 4 - NBO/TBO \qquad [13]$$

The modelling of each of the relevant slag physicochemical properties is discussed in the following sections. These include a definition of each property, experimental measurement techniques, and models published in the literature that may be used to model these properties as functions of temperature and chemical composition.

2.3.1 Viscosity

Fluid viscosity is the convective term constant of the momentum conservation equation, and in general is indicative of a fluid's resistance to flow or the ease with which slag of a certain composition flows at a specific temperature. In the smelting process, this is relevant in specific areas such as flow through a taphole, slag and metal separation, and smelting reaction kinetics.

20

Single-phase (fully liquid) metallurgical slags behave as Newtonian fluids (Kondratiev *et al.* 2002) with linear relationships between flow viscous stresses and local strain rates, and viscosity (the proportionality constant) being independent of the strain rate. Therefore slag viscosity (and flow behaviour) is related only to composition and temperature, irrespective of the forces acting on the slag. The viscosity, shear stress, and strain rate relationship is:

$$\tau = \mu \frac{du}{dx} \qquad\qquad [14]$$

in which τ is the shear stress, μ the fluid dynamic viscosity, and $\frac{du}{dx}$ the velocity gradient perpendicular to the shear direction (or the strain rate) (Versteeg and Malalasekera 2007).

Operating temperatures are, however, typically between the solidus and liquidus temperatures of the slags, which then contain some precipitated solids that affect viscosity. These multiphase slags reportedly behave as Newtonian fluids at solids up to 40% by volume (Kondratiev *et al.* 2002).

Experimental measurement:

Viscosities of slags can be measured experimentally, with variable degrees of accuracy influenced by instrumental, material, and hydrodynamic factors (Seetharaman *et al.* 2004). Typical experimental errors are large and can be around 25% (Mills and Keene 1987).

Experimental methods include (Aune *et al.* 2002, Mills and Keene 1987):

- *Oscillating methods:* Some object (cylinder, plate, or the crucible) is oscillated within the fluid. Viscosity is derived from the fluid density, period of oscillation, fluid dampening decrement, and radius and thickness of the cylinder.
- *Falling-body method:* Viscosity is derived from the time it takes a bob (typically a sphere) to fall or be dragged through a fluid. This method is popular for measuring Newtonian viscosities, but is regarded as inaccurate when measuring very low viscosities (Aune *et al.* 2002).
- *Rotating method:* Shear flow is induced through motion of boundary surfaces, mostly by rotating coaxial cylinders, cone and plates, or parallel disks. In rotating cylinder viscometers a bob is rotated within a crucible at a constant speed and the viscosity derived from the torque generated by the rotational speed (torsional resistance), height and diameter of the spindle, and diameter of the crucible.
- *Capillary method:* Viscosity is derived from the time required for a fluid to flow through a capillary tube, the constant pressure gradient between ends of the capillary, the capillary radius and length, and the fluid density. The materials used in this type of equipment typically allow for measurements up to 1200°C.

21

Viscosity modelling:

Slag viscosities are normally modelled with consideration of viscosity being largely dependent on the slag structure. Higher degrees of polymerisation cause increased viscosities, due to the increased resistance of longer chains of SiO_4^{4-} tetrahedral structural units moving over each other. The addition of basic components (CaO, MgO, and MnO) breaks up silicate chains and lowers the viscosity, increasing the ease with which slag flows.

Measured viscosities are related to temperature and chemical composition by different modelling techniques. Viscosity-temperature dependence is normally modelled by either the Arrhenius or the Weymann equations (Equations [15] and [16] respectively) (Mills *et al.* 2011):

$$\mu = 0.1\, A_A \exp(E_A/R\,T) \qquad\qquad [15]$$

$$\mu = 0.1\, A_w T \exp(E_w/R\,T) \qquad\qquad [16]$$

where μ is the estimated viscosity (Pa.s), A a pre-exponential constant (P.K^{-1}), E the activation energy (J.mol^{-1}), T the absolute temperature (K), and R the ideal gas constant (8.314 J.mol^{-1}.K^{-1}). The pre-exponential factors and activation energies are related to chemical component amounts in the available models through different types of empirical relationships.

These models mostly assume the slag to be fully liquid, but below the liquidus temperature precipitated solids that are suspended in the slag affect the viscosity to yield an observed (effective) viscosity. Slag at temperatures below its liquidus with between 10 to 40% solids by volume may still be considered a Newtonian fluid (Kondratiev *et al.* 2002). The liquid viscosity (μ_{liq}) may then be estimated and modified with an estimated amount of solids, using a relationship such as the Roscoe equation (Roscoe 1952) to estimate the effective viscosity, μ_{eff}:

$$\mu_{eff} = \mu_{liq}(1 - 1.35\,\emptyset)^{-2.5} \qquad\qquad [17]$$

where $\emptyset$ is the volume fraction of solids, which can be estimated through the Gibbs free energy minimization technique using thermodynamic software such as FactSage (Bale *et al.* 2009).

The following is a summarized review of viscosity models applicable to the manganese-bearing slag system. Models are discussed in more detail elsewhere, and include discussion on models for other slag systems (Seetharaman *et al.* 2004):

- *Urbain (Slag Atlas 1995, Mills et al. 2011):* Model developed for various slag systems, in which viscosity is related to temperature with the Weymann viscosity-temperature relationship, Equation [16]. The pre-exponential constant and activation energy are correlated to the sum of

22

mole fractions of slag constituents grouped into glass formers (SiO_2), modifiers (CaO, MgO, MnO), and amphoterics (Al_2O_3), where the contribution of some other species might be weighted.

- *Riboud (Slag Atlas 1995):* Model developed for mould fluxes, and extended to other types of slags. Similarly to the Urbain formalism, it is based on the Weymann viscosity-temperature relationship (Equation [16]). The pre-exponential constant and activation energy are also correlated to the mole fractions of constituents grouped into five categories, three of which apply to the constituents relevant to this study (i.e. SiO_2, CaO with MgO, and MnO, and Al_2O_3).

- *Iida (Mills et al. 2011):* Model developed for mould fluxes using a quasi-chemical modelling approach. Viscosity is correlated to a basicity index (ratio of acid to basic oxides) accounting for structure, and the changing basicity of amphoteric oxides (Al_2O_3) with temperature. The Arrhenius temperature relationship is used (Equation [15]).

- *Tang and Tangstad (2007):* Model developed with the focus on the MnO-SiO_2-Al_2O_3-CaO-MgO-FeO slag system, through extrapolation from binary systems and the temperature dependence based on the Eyring formalism. Viscosity is related to composition through binary activation energies.

- *FactSage (Decterov et al. 2009):* Viscosities of liquid slags and glasses are modelled and validated against data for multicomponent systems. The "Modified Quasichemical Model" is used with data from the thermodynamic databases to provide quantified estimations of the slag structure.

2.3.2 Thermal conductivity

Thermal conductivity is a property describing a material's ability to conduct heat, and is used with a temperature differential and length to calculate the rate of heat conduction. This property of metallurgical slags is important, especially when considering that the flow of energy affects the temperature, phase composition, and therefore other physicochemical properties. For example, in the taphole area during tapping the thermal conductivity would affect the temperature gradient throughout the tapstream, and also the amount of precipitated solids and viscosity, thus influencing the fluid flow behaviour and in turn the heat flow.

In specific process areas the amount of material solidified would be directly related to the thermal conductivity of the solidified material. This is relevant when operating furnaces with the freeze-lining concept, which are constructed with conductive refractories to promote the formation of a protective layer of solidified slag due to initial higher heat flow rates (Steenkamp *et al.* 2011).

Similar to viscosity, slag thermal conductivity is structurally dependent, increasing with SiO_2 content. This is reported to be due to the high thermal conductivity of covalently-bonded Si^{4+} and Al^{3+} ions, with thermal conductivity subsequently lowered by the network-breaking basic oxides (Mills et al. 2011). This can be further explained by considering that heat transfer involves the movement of phonons (or lattice vibrations), which is easier along the polymer chain than between the ends of different chains (Mills et al. 2011). Thermal conductivity of metallurgical slags is therefore a function of the chemical and phase composition, as well as temperature.

Figure 6 illustrates the expected trends in thermal conductivity, with an increase up to temperatures of around 700 to 1000 K (typically the glass transition temperature), followed by a sharp decrease up to the liquidus temperature, and then a slight decrease once the temperature is in the fully liquid region (Hayashi et al. 2001). The positive correlation between slag thermal conductivity and temperature is said to be due to the increase in collision frequency and the decrease in the phonon mean free path (Aune et al. 2002), but with the packing density and changes in the silicate network having greater effects.
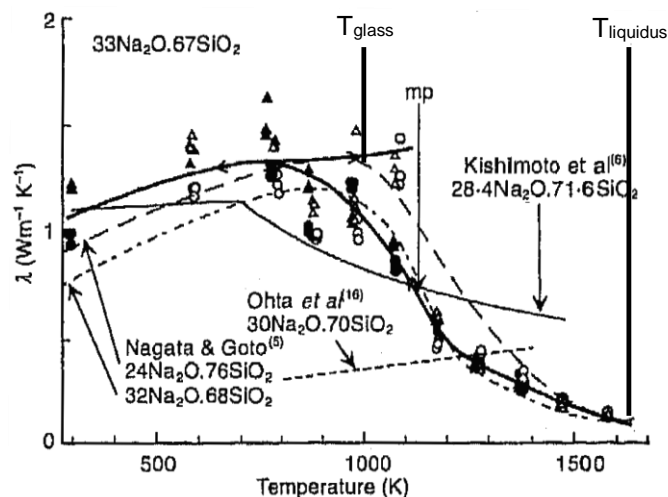
Figure 6 Thermal conductivity as a function of temperature for the Na_2O-SiO_2 system (Hayashi et al. 2001).

Experimental measurement:

Thermal conductivities of slags can be experimentally determined through a number of techniques, which mostly measure the heat flux, deriving thermal conductivity from the relationship:

$$q = -\frac{k_{eff}.\Delta T}{L}$$

[18]

with q being the measured heat flux (in $W.m^{-2}$), ΔT the temperature difference (in °C or K), L the distance over which the temperature difference is measured (in m), and k_{eff} the effective (or observed) thermal conductivity (in $W.m^{-1}.K^{-1}$) (Slag Atlas 1995).

24

When evaluating and modelling experimentally determined thermal conductivities, it is important to consider the experimental technique used and the fact that the effective thermal conductivity is made up of phonon conductivity (or conduction) and other heat transfer mechanisms, e.g. radiation and convection (Eriksson *et al.* 2003). Typical challenges are the prevention of convective heat transfer with liquids, and estimation of radiative heat transfer when performing these experimental techniques. The latter is more challenging in glassy and liquid slags which scatter less radiation than crystalline slags (Mills *et al.* 2011).

Typical experimental methods include the following steady-state and transient methods:

- *Laser-flash method (transient):* A thin sample is placed between two platinum discs, inserted into an even temperature zone, and heated until thermal equilibrium is obtained. The top surface is exposed to a short pulse of laser energy while the temperature of the lower disc is continuously measured by infrared detector (Eriksson *et al.* 2003). The thermal conductivity is calculated from the observed temperature change over time (Mills *et al.* 2011).

- *Hot-wire method (transient):* A sample is heated by passing an electrical current through a thin metal wire, while the sample temperature is continuously monitored through its temperature-resistance relationship. Thermal conductivity is derived from the temperature-time relationship during the period of linear increase. The influence of convection is visible in the deviation from the linear temperature-time relationship only at higher temperatures, and is not considered in this method (Eriksson *et al.* 2003).

- *Linear/radial heat flow method (steady state):* A sample is placed around an electrical heat source within an insulated apparatus and heated. The thermal conductivity is derived from the temperature profile (Slag Atlas 1995).

- *Phase-shift methods (non-steady state):* In the radial wave method, the outer wall of a crucible is subjected to temperature variation, measured by thermocouples on the wall. A thermocouple along the central axis of the crucible monitors the change in temperature at the centre of the crucible, which is then used to derive thermal diffusivity. In the modulated beam technique, a laser beam is used to produce a periodic temperature variation at a constant frequency on the front face of a disk. The phase shift in the temperature variation between the front face and that measured at the back face is used to derive thermal diffusivity (Glaser *et al.* 2013).

Thermal conductivity modelling:

Thermal conductivity of slags is related to their chemical composition and temperature, with distinctively different behaviour and models dependent on whether the slag is glassy (and amorphous), or crystalline, or in the liquid phase (Mills *et al.* 2011). In the liquid state, thermal conductivity increases with SiO_2 content, and is directly correlated with the degree of polymerisation (Q) or inversely correlated

25

with the ratio of non-bridging oxygen to tetragonal-bonded oxygen (NBO/TBO). The models reported by Mills *et al.* (2011) are summarised here.

Thermal conductivities of the solidified slag are estimated at 298 K and at the glass transition temperature with the following equations, assuming a linear dependence between these temperatures:

$$k_{298K} = -0.424 + 0.00002\, e^{Q/0.299} \qquad [19]$$

$$k_{Tg} = -0.435 + 0.00005\, e^{Q/0.332} \qquad [20]$$

where Q is the degree of polymerisation, and k the estimated thermal conductivity (W.m⁻¹.K⁻¹) at either 298 K (k_{298K}) or at the glass transition temperature (k_{Tg}).

For liquid slags a model has been derived by correlating measured thermal conductivities with modelled viscosities using the model of Riboud (Mills *et al.* 2011):

$$\ln(k_{Tm}) = -2.178 + 0.282\, ln(\mu_R) \qquad [21]$$

where μ_R is the viscosity estimated with the model by Riboud (poise), and k_{Tm} the thermal conductivity of the slag from the melting temperature (W.m⁻¹.K⁻¹). A linear dependence is also assumed between the thermal conductivity at the glass transition temperature (Equation [20]) and the thermal conductivity calculated at the melting temperature (Equation [21]).

2.3.3 Density

Material mass density refers simply to the mass of material per unit volume. In flow modelling, the conservation equations are expressed in and solved for volume units, while the quantities and other properties are typically mass- (or molar-) based, requiring the conversion of density to a volume basis. Density specifically features in the heat transfer equation with mass-specific heat capacity in both transient and convective terms. It is also present in several terms of the mass transport equation. Density differences between slag and metal are also an important operational parameter, influencing separation between slag and metal (Zhang and Chou 2010) in the smelting processes of interest here.

Density can be expressed as specific gravity (SG), being the ratio of density to that of water at 1 atmosphere and 4°C. When evaluating and modelling the density of slags, molar volumes (V_m, m³.kmol⁻¹) of the constituents are considered, being the molar mass (MM, kg.kmol⁻¹) divided by the density (ρ, kg.m⁻³):

$$V_m = \frac{MM}{\rho} \qquad [22]$$

Similar to the properties discussed earlier, the density of slags is dictated mostly by the fraction of SiO_2 relative to other oxides, and the resulting structure and arrangement of silicate chains (Slag Atlas 1995). Partial molar volumes of the slag constituents are therefore not constant with varying compositions.

Density is generally expected to decrease with increasing temperature, since the relative affinities become weaker as the types and sizes of ions and the activation energies change with temperature (Zhang and Chou 2010). Density is related to temperature simply through the volumetric thermal expansion coefficient, α, as the derivative of density with regard to temperature:

$$\alpha = \left(\frac{1}{V}\right)\left(\frac{\partial V}{\partial T}\right)_p \hspace{2cm} [23]$$

For the different slag constituents, it has been reported that the thermal expansion coefficient increases with optical basicity, making slags with high basicities (lower degrees of polymerisation) more sensitive to temperature (Zhang and Chou 2010). Low-basicity constituents (e.g. SiO_2) are expected to be tightly bonded with low thermal expansion, and thermal expansion increases with cation size (Mills *et al.* 2011).

Experimental measurement:

Typical slag density measuring methods include the following (Slag Atlas 1995):

- *Pycnometry*: The mass of material in a vessel with known volume is weighed.
- *Buoyancy method (Archimedes principle)*: In the direct method density is derived from the change in mass of an inert bob (with known volume) immersed into the melt. In the indirect method the density of the melt is derived from the change in mass of a closed crucible containing the melt which is immersed into a buoyant liquid.
- *Dilatometer*: A sample with known mass is placed in a known volume of gas at known pressure, which is then pressurised. The density is derived from the initial and new volumes and pressures.
- *Manometer*: Density is derived from the relative difference in fluid heights for the same pressure exerted on a fluid with known density and on the fluid with unknown density.
- *Droplet methods*: The density of liquid droplets can be determined by either estimating the volume from measured dimensions of a sessile droplet, or the rate at which a droplet falls through a liquid of a lower density.

- *Suspension methods*: The material tested is placed into suspension in a liquid that is non-reactive and composed of a mixture of two liquids, one denser and one less dense than the material tested. The density of this final mixture is determined using one of the above methods.

Density modelling:

Density is typically estimated through summation of partial molar volumes:

$$V = X_1\bar{V}_1 + X_2\bar{V}_2 + X_3\bar{V}_3 + \cdots \qquad [24]$$

where V is the total molar volume (m^3.kmol^{-1}), X_i the mole fraction of component i, and $\bar{V}_i$ the partial molar volume of component i (in m^3.kmol^{-1}). The values (or equations) of the molar volumes of slag constituents at specific temperatures can be found in the literature, together with constant thermal expansion coefficients (Slag Atlas 1995). The temperature relationship of density has also been expressed as the Arrhenius equation (Zhang and Chou 2010), which relates the activation energy to the constituent concentrations.

For modelling solid slag densities, the documented molar volumes for crystalline slag constituents at 25°C are listed in Table 7. The basic oxides have lower molar volumes compared to SiO_2 and Al_2O_3, and therefore higher densities.

The reported average volumetric thermal expansion coefficient of 9 x 10^{-6} K^{-1} is used to calculate density up to the glass transition temperature (Mills *et al.* 2011):

$$\rho = \rho_{298K}/(1 + 9 \times 10^{-6}\, \Delta T)^3 \qquad [25]$$

where ρ is the density at the required temperature (kg.m^{-3}), ρ_{298K} is the crystalline density at 25°C (kg.m^{-3}), and ΔT is the difference between the temperature (K) at which density is calculated and 298 K.

Table 7 Partial molar volumes of crystalline slag solid constituents at 25°C (Mills *et al.* 2011).

Constituent	Molar volume ($\bar{V}_i$, m^3.kmol^{-1})
SiO_2	23.76 + 3.5 X_{SiO2}
Al_2O_3	40.4
CaO	14.4
MgO	12.5
MnO	17

A simple model from Mills and Keene (1987) was published for estimating the density of liquid slags. This is provided as Equation [26], for which a constant thermal expansion coefficient of 1 x 10^{-4} K^{-1} is prescribed (Mills and Keene 1987).

$$\rho_{1673K} = 2490 + 12\,(w_{FeO} + w_{MnO}) \qquad [26]$$

28

where ρ_{1673K} is the liquid slag density at 1673 K, and w_{FeO} and w_{MnO} are the mass fractions of FeO and MnO respectively in the slag.

The average density of a solid-liquid mixture between the solidus and liquidus temperatures can be calculated as follows:

$$\rho = (1 - \emptyset)\, \rho_{solid} + \emptyset\, \rho_{liquid} \qquad [27]$$

where ρ is solid-liquid mixture density (kg.m^{-3}), ρ_{solid} and ρ_{liquid} are the solid and liquid densities respectively (kg.m^{-3}), and $\emptyset$ is the volume fraction solids.

2.3.4 Heat capacity and enthalpy

Heat capacity is the relation between a change in a material's temperature and the energy required to bring about the temperature change. In the mass and energy flow applications of interest, heat capacity features in the transient and convective terms of the heat transfer equation. Over time, the fluid temperature response is dependent on the mass of material and heat transferred in a time step and the heat capacity of the material. Other temperature dependent properties (e.g. viscosity, thermal conductivity, density) are therefore indirectly related to heat capacity.

Heat capacity is by definition the derivative of enthalpy with regard to temperature (at constant pressure), with units per mass or molar amount (J.kg^{-1}.K^{-1} or J.mol^{-1}K^{-1}):

$$C_p = \frac{dH}{dT} \qquad [28]$$

where C_p is heat capacity at constant pressure (J.kg^{-1}.K^{-1}), H is specific enthalpy (J.kg^{-1}), and T is temperature (K).

The heat capacity of metallurgical slags is reported to depend mostly on temperature, and to a lesser degree on structure (Mills *et al.* 2011). Heat capacity is therefore modelled as a partial molar property combining the values for each of the individual constituents at certain temperatures. Energy is required for phase (or structural) changes over the temperature range (e.g. from crystalline solid to liquid slag), and enthalpy is therefore not a continuous function of temperature. Step changes in enthalpy at specific temperatures have to be considered when using heat capacities.

It is reported that the heat capacity of glassy slags is approximately 200 J.kg^{-1}.K^{-1} higher than that of crystalline slags and, unlike crystalline slags, the enthalpy does not undergo a step change at the melting temperature (Mills *et al.* 2011). The heat capacity of glassy slags increases with temperature from the glass transition temperature up to the melting temperature, with no enthalpy difference between the solid and liquid at the melting temperature.

29

Experimental measurement:

Heat capacities of slags are typically measured using commercially available differential scanning calorimeters, or drop calorimeters (Mills *et al.* 2011). A differential scanning calorimeter normally contains two crucibles, one containing the slag sample and the other some reference sample. Both crucibles are heated at a constant rate by conduction, with the temperatures monitored with thermocouples. Heat capacity is derived from the measured temperature difference and known heat capacity of the reference material.

In a drop calorimeter the sample is heated in an upper insulated part to a specific temperature and dropped into a lower part consisting of an insulated metal block (high thermal conductivity). The temperature of the lower part is monitored while it is allowed to reach thermal equilibrium. As with the differential scanning calorimeter, the sample heat capacity is derived from the change in temperature and the known thermal properties of the lower metal block.

Heat capacity and enthalpy modelling:

Enthalpies (and heat capacities) of slags are functions of their chemical composition, temperature, and to some extent structure. With temperature changes, step changes in enthalpy are expected, associated with phase (and structure) transitions. Heat capacities and enthalpies can be estimated with models available in the literature, or with commercially available software.

Some of the models and software considered for estimating heat capacity (or enthalpy) include:

- *Enthalpy model* (Björkvall *et al.* 2001): A thermodynamic model developed for multicomponent slags by combining experimental data for binary sub-systems. The model estimates the enthalpy of multicomponent liquid slags by extrapolating for temperature from the enthalpies of the pure species at 1600°C and using the heat capacity around that temperature (also for the pure species). Heat of mixing for the liquid phase is added, calculated from binary cation interactions.

- *FactSage* (Bale *et al.* 2009): Commercially available computational thermochemistry software, used to estimate phase composition through chemical equilibrium, and the enthalpy and heat capacity of a mixture at any temperature. Model parameters are stored in a database as temperature-dependent heat capacity equation coefficients and interaction parameters. Enthalpy results therefore reflect heats of fusion and mixing, and other phase transformations.

- *Heat capacity models* (Mills *et al.* 2011): The models estimate heat capacity of crystalline, glassy, and liquid slags by considering heat capacity as a partial molar property. For each type of slag, depending on its temperature, the temperature-dependent heat capacities of each constituent are combined to obtain the total heat capacity:

30

$$C_p = \sum X_i C_{pi} \qquad \qquad [29]$$

where X_i is the mole fraction of constituent *i* and C_{pi} is the heat capacity of constituent *i* (J.kg^{-1}.K^{-1}). For crystalline slag the heat capacity of each component is calculated as follows:

$$C_{pi} = a_i + b_i T - c_i/T^2 \qquad \qquad [30]$$

where T is temperature (K), and a_i, b_i and c_i are coefficients for each slag constituent.

For liquid slags a constant heat capacity is assumed for each constituent and the heat capacities are combined using the molar fractions of the constituents (Equation [29]).

3   Slag physicochemical property model formulation

In this work, physicochemical properties of interest for slags in the CaO-MnO-SiO$_2$-Al$_2$O$_3$-MgO system have been modelled by applying the models selected from literature. This section contains the formulation of the models specifically applied to calculate the properties: solidus and liquidus temperatures, viscosity, thermal conductivity, density, and heat capacity. FactSage is used as the starting point to determine the phase composition at different temperatures, for use as input to other models.

3.1   Metallurgical system

The slag system is defined to enable modelling of slag physicochemical properties using computational thermochemistry methods. The system of interest is mostly defined in terms of the temperature and compositional ranges. Chemical constituents are considered when present in major amounts, or when having significant influence on some property even if present in small amounts. This defines the solid and liquid metallurgical phases possibly present in the system at different operating conditions, and is used to configure computational thermochemistry software for the calculation of physicochemical properties.

For the production of SiMn or HCFeMn the important physicochemical properties are evaluated for the CaO-MnO-SiO$_2$-Al$_2$O$_3$-MgO slag system only, ignoring all minor components (P, S, K$_2$O, Na$_2$O, TiO$_2$, etc.). Typical slag chemical compositions (Table 8) are used as the basis for the calculation. These compositions vary between processes producing the same alloy due to different operating practices.

Process temperatures in SiMn production range from 1600 to 1650°C, with the slag leaving the furnace between 1550 and 1650°C, while process temperatures in HCFeMn production range between 1400 and 1500°C (Olsen *et al.* 2007). An ambient temperature of 25°C is used, considering that slag could possibly cool down to this temperature in a modelled domain.

The components specified for the metallurgical system were CaO, MnO, MgO, and 3(SiO$_2$).Al$_2$O$_3$. The latter virtual species is defined to simulate a typical Al$_2$O$_3$/SiO$_2$ weight ratio of 0.57, eliminating the need to specify Al$_2$O$_3$ as a fixed percentage in the evaluation of ternary diagrams.

This metallurgical system was configured with solution phases and pure solid phases within FactSage 6.2 (Bale *et al.* 2009) with selections from the FToxid database. The phases were selected with prior knowledge of the solid and liquid phases expected for this type of metallurgical system, derived from published phase diagrams (Figure 7). The most important selected phases, with their FactSage FToxid database names, include the following (Bale *et al.* 2009):

- *ASlag-liq*: Liquid slag solution phase of CaO, MgO, MnO, Al$_2$O$_3$, and SiO$_2$.
- *AMonoxide:* Solid solution phase of CaO, MgO, MnO, and Al$_2$O$_3$.

- *Melilite*: Solid solution of $Ca_2MgSi_2O_7$ and $Ca_2Al_2SiO_7$.

- *Mullite*: Solid solution phase of Al_2AlO_5 and Al_2SiO_5.

- *AOlivine:* Solid solution phase of Mg_2SiO_4 (forsterite), Ca_2SiO_4 (larnite), $CaMgSiO_4$ (monticellite), Mn_2SiO_4 (tephroite), $MnCaSiO_4$, $CaMnSiO_4$, $MgMnSiO_4$, and $MnMgSiO_4$.

- *ASpinel*: AB_2O_4-type cubic spinel solution containing Al, Mg, and O (oxidation states 2^+ and 3^+ only) (e.g. spinel: $MgAl_2O_4$ and pleonaste: $MgAl_2O_4$).

- *SiO_2(s6)*: Pure solid SiO_2, cristobalite h.

- *aCa_2SiO_4*: Solid solution phase of mostly of Ca_2SiO_4, and possibly of Mg_2SiO_4 and Mn_2SiO_4.

Using the metallurgical system definition, ternary phase diagrams were configured and generated in FactSage 6.2 (Bale *et al.* 2009). The diagrams were configured with $3(SiO_2).Al_2O_3$, CaO and MnO at the A, B, and C corners of the pseudo-ternary diagrams respectively, with a fixed percentage of 6% MgO. Diagrams were calculated at 1400, 1500, and 1600°C to cover the typical operating temperatures of both HCFeMn and SiMn processes.
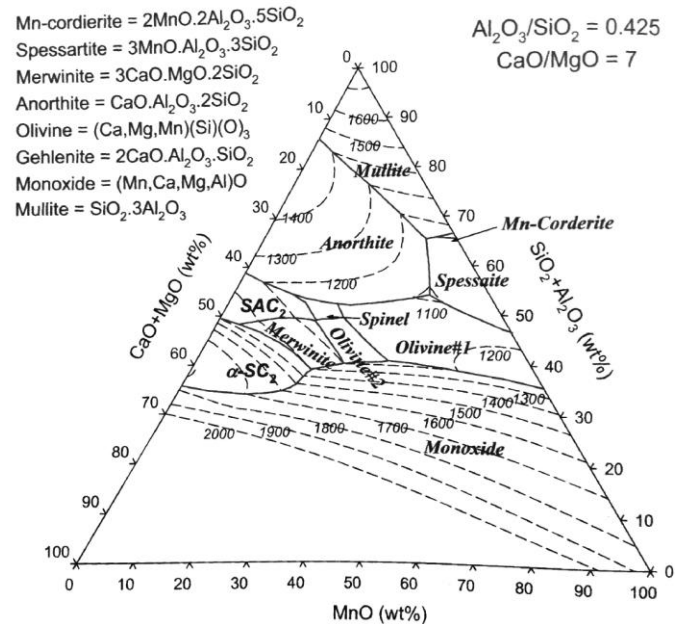
Figure 7 Calculated phase and liquidus relations for the MnO-SiO_2-CaO-Al_2O_3-MgO system (Olsen *et al.* 2007).

3.2 Solidus and liquidus temperatures

Slag solidus and liquidus temperatures were also calculated. These are important parameters to consider when modelling physical properties, since they indicate the transition from solid to liquid, and in most cases a significant change in behaviour with regard to temperature and composition. A glass transition temperature of 700°C was constantly applied for all the compositions considered, derived as a typical value from the data in Mills *et al.* (2011). To determine the liquidus temperature, FactSage 6.2 (Bale *et al.* 2009) was configured to find the temperature at which the first solid would start to

33

precipitate from the liquid slag phase. The same configuration was also used to determine the solidus temperature, determined as the temperature at which the first liquid slag forms upon heating.

3.3   Viscosity

To model slag liquid viscosity, the models from the literature were applied as functions of chemical composition and temperature. The models applied were those of Mills *et al.* (2011), Riboud (Slag Atlas 1995), Iida (Mills *et al.* 2011), and Tang and Tangstad (2007). The viscosity module in FactSage 6.2 (Bale *et al.* 2009) was also used to calculate viscosity. Prior to calculation, the phase compositions were estimated with FactSage at the specified temperatures. This provided the slag liquid chemical composition used to estimate the slag liquid viscosity. The volume fractions of solids were calculated to be used with the Roscoe equation (Equation [17]) (Roscoe 1952) to adjust the liquid viscosity and yield the effective viscosity.

3.4   Thermal conductivity

The thermal conductivity models by Mills *et al.* (2011) were applied to model slag thermal conductivity as functions of slag chemical composition and temperature. The models allowed for differentiation between glassy, crystalline, or fully liquid slag, depending on temperature. The thermal conductivity model of Riboud (Mills *et al.* 2011) reported earlier was considered, but this system yielded results significantly different from those typically expected for slag.

3.5   Density

The density models of Mills *et al.* (2011) and Mills and Keene (1987) were applied to model slag density as functions of slag chemical composition and temperature. The models allowed for differentiation between solid and liquid slag.

3.6   Heat capacity

The heat capacities of solids and liquids were derived from the enthalpies calculated with FactSage 6.2 (Bale *et al.* 2009). Calculated enthalpies were found to be almost linearly related to temperature, and heat capacities were subsequently determined by fitting a straight line through enthalpies calculated between two temperatures. The solids heat capacities were derived between 298 K and the solidus temperature, and the liquid heat capacity between the liquidus temperature and 2100 K (arbitrarily chosen high value). The liquid slag heat capacity model by Björkvall *et al.* (2001) was also applied. Enthalpy of melting was derived as the difference between the enthalpy calculated at the liquidus temperature with FactSage and the solid enthalpy estimated at this liquidus temperature by extrapolating the FactSage estimated enthalpy at 298 K and the derived solid heat capacity.

To compare different enthalpy and heat capacity models, enthalpies at temperatures relative to a reference (298 K) have been derived. Enthalpy difference ($H_T - H_{298K}$, in J.kg^{-1}) was calculated as the integral of heat capacity (C_p, in J.kg^{-1}.K^{-1}) between the reference state of 298 K and the temperature of interest (T, in K):

$$(H_T - H_{298K}) = \int_{298K}^{T} C_p dT \qquad [31]$$

Because heat capacity, C_p, is quoted mostly as functions of temperature or constant values, the above enthalpy difference could be determined simply through analytical integration of the temperature-dependent equation. In the case of the results calculated using FactSage, the chemical equilibrium and enthalpy of the resulting mixture were calculated at the temperature of interest as well as at 298 K.

4   Slag physicochemical property model – results and discussion

The results presented here were obtained by applying the slag property models described in the previous sections. For the purpose of evaluating the properties of relevant slags in the $CaO-MnO-SiO_2-Al_2O_3-MgO$ system, typical HCFeMn and SiMn slags were identified and used in the application of the models. The slag compositions (Table 8) were selected to cover a wide operating range of slag compositions from the most common practices. These include the compositions from the literature shown in Table 3 and Table 4 (Olsen *et al.* 2007), as well as values inferred from working experience.

The following data is presented for each of the slag properties considered (where applicable):

- Pseudo-ternary phase diagrams, calculated for the $CaO-MnO-SiO_2-Al_2O_3-MgO$ system.
- Pseudo-ternary diagrams were calculated for each of the slag properties, showing estimated property values as contours together with the placement of the typical slag compositions considered (Table 8).
- Slag viscosity measurements reported in the literature were used to validate the models, comparing the reported measurements to the modelled values estimated for the reported chemical compositions and temperatures. Reliable measurements for the other properties for the slag system considered could not be obtained from the literature, and estimated property values were related to values for other systems merely in terms of order of magnitude.
- Slag properties were calculated and analysed as functions of temperature and basicity for each of the typical slag compositions considered (Table 8). The B5 basicity, calculated as $(CaO+MgO+MnO)/(SiO_2+Al_2O_3)$, was varied by adjusting the species percentages in such a way that the ratios of species in the numerator and denominator remained constant relative to each other. The baseline temperature of 1400°C was used for the HCFeMn slags, and 1600°C for the SiMn slags.
- Physicochemical properties are summarised as values estimated for each of the typical slag compositions (Table 8) at 1400°C for the HCFeMn slags, and 1600°C for the SiMn slags. These values are used later in the tapping flow modelling.

Table 8 Typical HCFeMn and SiMn slag compositions used for modelling physicochemical properties.

	Slag compositions (wt.%)						
	HCFeMn Slag A	HCFeMn Slag B	HCFeMn Slag C	HCFeMn Slag D	SiMn Slag A	SiMn Slag B	SiMn Slag C
MnO	40.9	15.1	29.8	36.0	8.5	7.7	3.1
SiO_2	23.1	24.0	30.0	24.0	45.2	42.1	41.8
Al_2O_3	12.7	20.7	4.3	16.0	15.8	20.9	20.0
CaO	16.9	34.4	29.3	20.0	21.0	22.4	29.0
MgO	6.4	5.7	6.6	4.0	9.5	6.9	6.2
Basicity*	1.79	1.23	1.91	1.5	0.64	0.59	0.62

* Basicity = $(CaO+MgO+MnO)/(Al_2O_3+SiO_2)$

36

4.1 Pseudo-ternary phase diagrams

The pseudo-ternary phase diagrams for the slag system are illustrated in Figure 8–10, which show the phase regions expected for the slag system with 6% MgO and Al_2O_3/SiO_2 ratio of 0.57 (according to the stoichiometric species $3(SiO_2).Al_2O_3$), calculated at 1400, 1500, and 1600°C. The monoxide and di-calcium silicate solid solution phase boundary lines indicate the liquidus points for typical HCFeMn and SiMn slag compositions (Table 8). In these diagrams, the percentage of CaO plus 6% MgO is plotted on the B-corner axis, and therefore only compositions with CaO + MgO greater than 6% are valid.

In HCFeMn production the slags are operated close to or below their liquidus temperatures, with the first phase to precipitate being the monoxide phase. This is evident in Figure 8, generated for 1400°C, which is closest to the typical HCFeMn operating temperature. An apparent outlier is HCFeMn slag B from the discard slag practice, having a very low MnO content and higher (less diluted) $SiO_2 + Al_2O_3$ contents. For this slag the liquidus temperature is around 1400°C, but the first phase to precipitate will be di-calcium silicate. Physicochemical properties influenced by the presence of solids might therefore be sensitive to variations in temperature and chemical composition in the case of HCFeMn slags.

SiMn slags are all shown to be operated above their liquidus temperature, with compositions within the liquid-only phase region on the diagram generated for 1600°C (Figure 10). The diagram generated for 1400°C (Figure 8), however, suggests that at this temperature the SiMn slags will still be fully liquid, but the first solid phase to precipitate might be melilite.
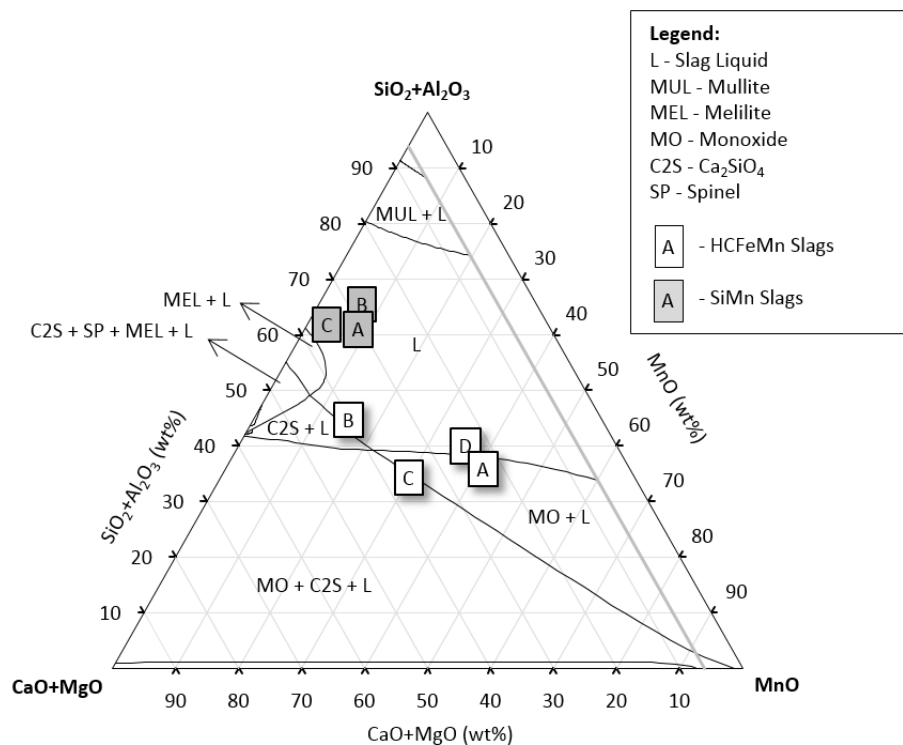
Figure 8 Pseudo-ternary phase diagram of the CaO-MnO-SiO₂-Al₂O₃-MgO slag system with 6% MgO and Al₂O₃/SiO₂ = 0.57 at 1400°C, generated with FactSage 6.2 (Bale *et al.* 2009), showing typical SiMn and HCFeMn slag compositions (Table 8).
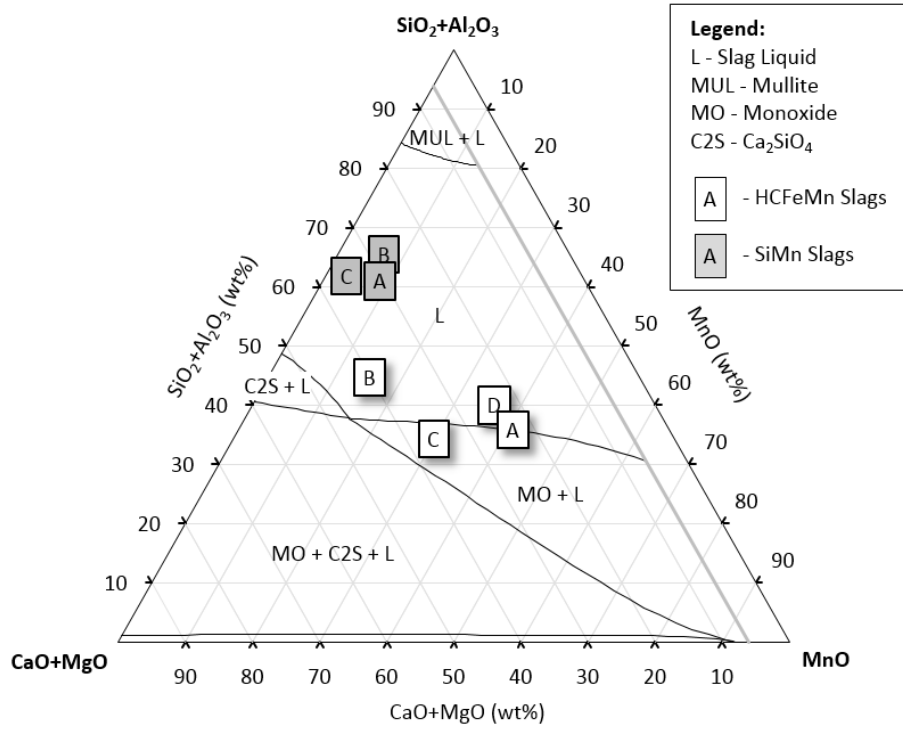
Figure 9 Pseudo-ternary phase diagram of the CaO-MnO-SiO₂-Al₂O₃-MgO slag system with 6% MgO and Al₂O₃/SiO₂ = 0.57 at 1500°C, generated with FactSage 6.2 (Bale *et al.* 2009), showing typical SiMn and HCFeMn slag compositions (Table 8).
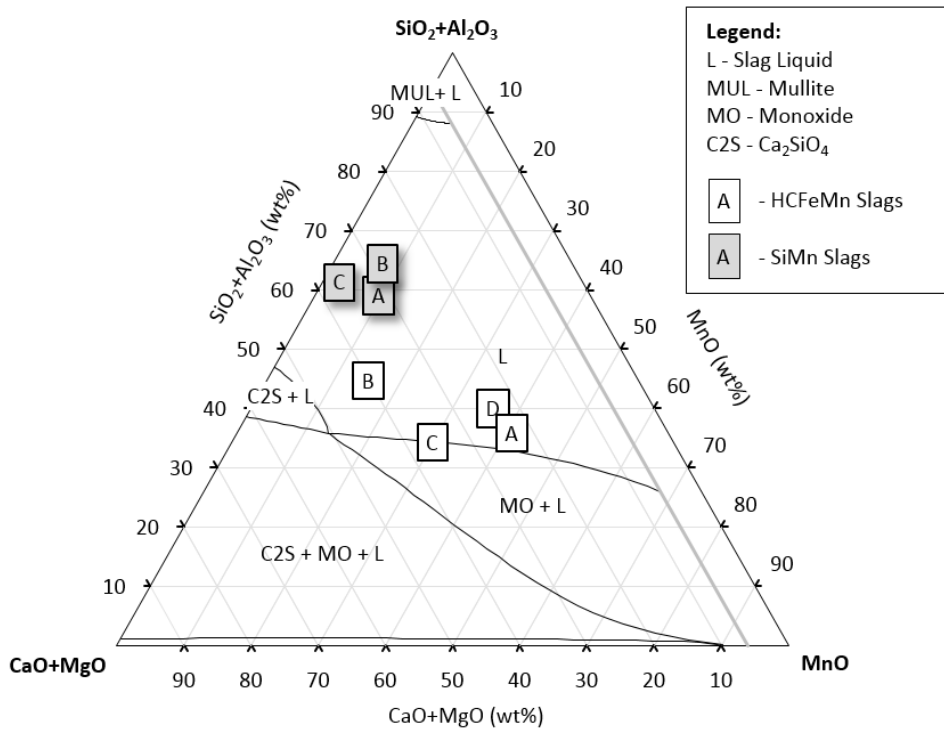
Figure 10 Pseudo-ternary phase diagram of the CaO-MnO-SiO₂-Al₂O₃-MgO slag system with 6% MgO and Al₂O₃/SiO₂ = 0.57 at 1600°C, generated with FactSage 6.2 (Bale *et al.* 2009), showing typical SiMn and HCFeMn slag compositions (Table 8).

4.2 Solidus and liquidus temperatures

The liquid slag phase boundary lines on the pseudo-ternary phase diagrams (Figure 8–10) indicate the liquidus points at the specific temperature (1400, 1500, or 1600°C) for fixed MgO contents and Al_2O_3/SiO_2 ratios. These fixed values vary between the slag compositions considered, having an effect on the solidus and liquidus temperatures. The more precise solidus and liquidus temperatures calculated specifically for the typical SiMn and HCFeMn slag compositions (Table 8) are compared in Figure 11.

Estimated solidus temperatures are somewhat higher and vary over a wider range for the HCFeMn slags, ranging between 1106 and 1167°C compared to 1071 and 1075°C for the SiMn slags. Liquidus temperatures of the HCFeMn slags are also mostly higher than those of the SiMn slags due to the higher monoxide contents of the HCFeMn slags. The liquidus temperatures of the HCFeMn slags vary between 1323 and 1501°C, around the typical operating temperature of approximately 1400°C. For SiMn slags, liquidus temperatures vary between 1233 and 1296°C, which is lower than those of HCFeMn slags, but also significantly lower than the typical SiMn operating temperature of around 1600°C. SiMn processes are therefore operated at temperatures much higher than the slag liquidus temperatures, to promote the extent and rate of the reduction reactions. HCFeMn processes are operated with slags closer to their liquidus temperatures, and the precipitation of solids can be expected to have a significant influence on some of the slag physicochemical properties, especially viscosity. In the case of SiMn slags, despite being operated above the liquidus temperatures, physicochemical properties (especially viscosity) could also be negatively influenced by the higher SiO_2 contents and longer polymer chains.

	HCFeMn A	HCFeMn B	HCFeMn C	HCFeMn D	SiMn A	SiMn B	SiMn C
Solidus	1121.7	1166.9	1128.7	1106.2	1071.6	1074.7	1072.4
Liquidus	1501.2	1418.5	1443.7	1323.4	1232.9	1310.3	1295.7
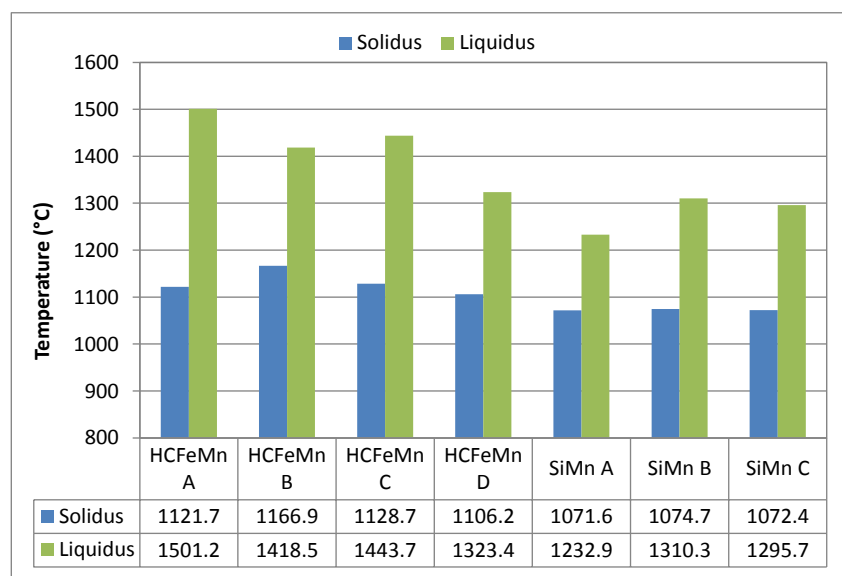
Figure 11 Solidus and liquidus temperatures of typical SiMn and HCFeMn slag compositions (Table 8) calculated with FactSage 6.2 (Bale *et al.* 2009).

The pseudo-ternary liquidus temperature diagram generated with FactSage 6.2 for the same slag system, with 6% MgO and Al_2O_3/SiO_2 ratio of 0.57, is shown in Figure 12. This diagram shows the liquidus temperature lines from 1200 to 2000°C in steps of 100°C. The diagram indicates that the lowest liquidus temperature of the typical slag compositions is approximately 1275°C. It again illustrates that SiMn slags have lower liquidus temperatures than typical HCFeMn slags, with SiMn slags containing lower amounts of the high-melting monoxide solid solution phase. SiMn slags are located in a region of the pseudo-ternary liquidus diagram where variations in chemical composition have little effect on the liquidus temperature unlike HCFeMn slags, where small differences in especially SiO_2 and Al_2O_3 have a significant effect on liquidus temperature.
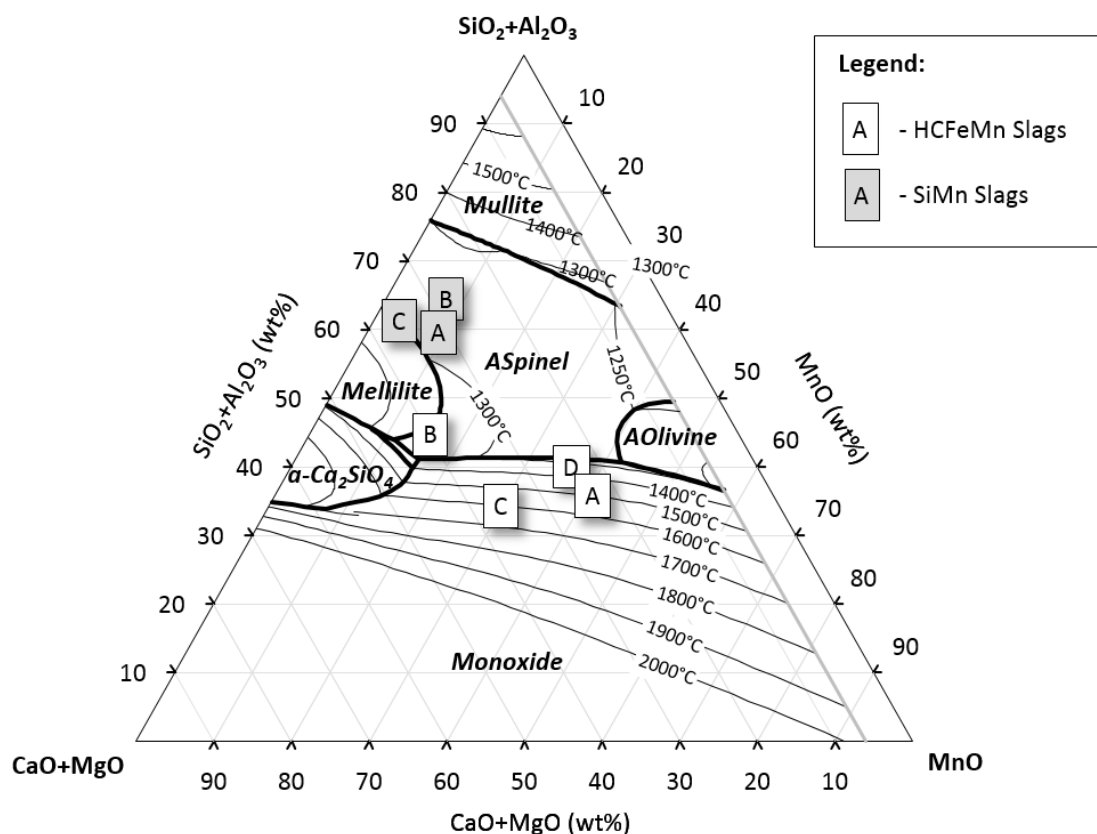
Figure 12 Liquidus temperature pseudo-ternary diagram of the CaO-MnO-SiO_2-Al_2O_3-MgO slag system with 6% MgO and Al_2O_3/SiO_2= 0.57, showing typical SiMn and HCFeMn slag compositions (Table 8), calculated with FactSage 6.2 (Bale *et al.* 2009).

4.3 Viscosity

Model validation:

The selected viscosity models applied were validated against measured viscosity data for a similar slag system. Limited measured viscosity data is available in the open literature for slags with similar amounts of all five components defining this slag system. The same viscosity data referenced by other authors (Tang and Tangstad 2007) was used, and is summarised in Table 9.

Table 9 Summary of measured slag viscosities referenced by other authors (Tang and Tangstad 2007).

Original reference		SiO$_2$ (wt. %)	Al$_2$O$_3$ (wt. %)	CaO (wt. %)	MnO (wt. %)	MgO (wt. %)	Temperature (°C)	Measured viscosity (P)
Benesch *et al.* (1984) (21 data points)	Min.	32.1	6	31.2	5	4.8	1400	3.7
	Max.	41.8	7	40.9	25.3	6	1500	5.9
	Avg.	37.2	6.4	35.3	15.3	5.1	1450	4.3
Kozakevitch (1949) (6 data points)	Min.	31.2	10.1	44.7	0.94	2	1400	3
	Max.	38.3	19	48.4	1.17	4	1500	6.6
	Avg.	34.8	14.6	46.6	1.1	3.0	1450	5.0
Chubinidze (1974) (12 data points)	Min.	20	10	30	10	5	1500	1.4
	Max.	45	35	30	10	5	1600	2.8
	Avg.	32.5	22.5	30.0	10.0	5.0	1550	2.0
Engh (1975) (647 data points)	Min.	35.6	14	16.81	7.29	3.05	1431	6.4
	Max.	49.7	30	26.25	10.59	7.9	1816	372.3
	Avg.	42.1	21.5	21.7	9.0	5.7	1651	77.9
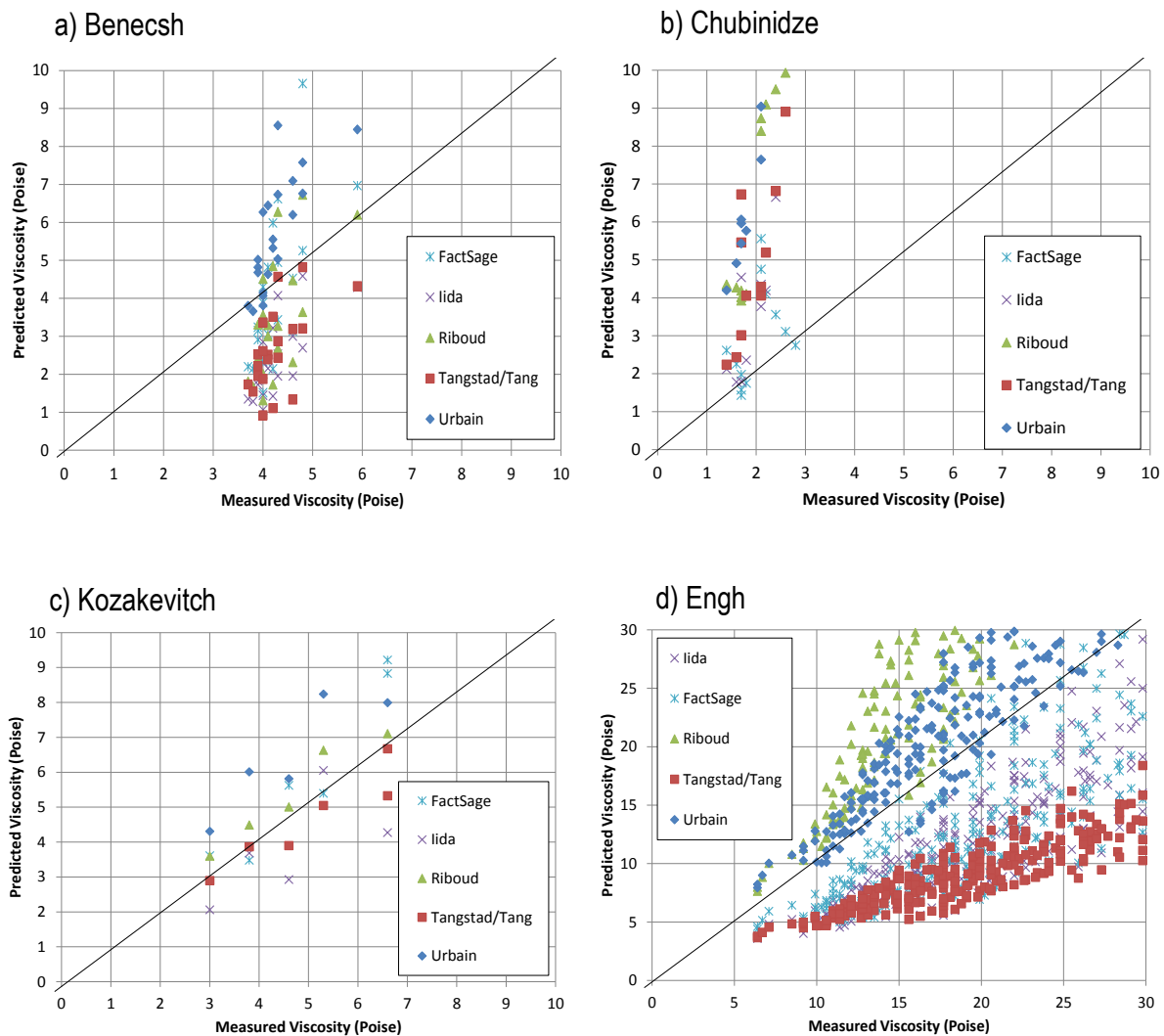
Figure 13 Viscosities estimated with different models correlated to measurements by (a) Benesch *et al.* (1984), (b) Chubinidze (1974), (c) Kozakevitch (1949), and (d) Engh (1975).

Figure 13 compares estimated viscosities using the different models, and the reported measured values (summarised in Table 9). Large variations in the data values, and in some cases the limited number of data points, made it difficult to quantify the differences between the calculated and measured viscosities, where normally a correlation coefficient could be calculated. In general, it should also be

41

considered that the experimental measurement of viscosity is difficult and the results may contain errors. The following conclusions can be drawn from these graphs:

- For the data by Benesch *et al.* (1984) and Chubinidze (1974), significantly large differences were obtained between measured values (Figure 13a and b) and the results from the independently developed models believed to be consistent and structurally correct.

- In the relatively small data-set by Kozakevitch (1949), estimated viscosities are closer to the measured values when compared to the other viscosity data-sets (Figure 13c). The model by Tang and Tangstad (2007) offers the best overall correlation (Figure 13).

- The large data-set by Engh (1975) displays mostly either positive or negative deviations from the measured values (Figure 13d). Significant negative deviations are obtained with the model by Tang and Tangstad (2007), with models by Urbain (Mills *et al.* 2011) and FactSage 6.2 (Bale *et al.* 2009) providing results closest to measured values in the range below 30 P. Consistently lower viscosities are estimated at higher measured viscosities.

- The newer version of the Urbain model (Mills *et al.* 2011) will be used in further evaluation of this slag system, since it is well known and easily applicable, offering acceptable correlations in the above evaluations (Figure 13c and d).

Sensitivity analysis:

Estimated volume fractions of solids at equilibrium and the effective viscosities calculated are illustrated as functions of basicity (Figure 14) and temperature (Figure 15). Both indicate distinct differences for the baseline compositions, due to the significant differences in basicity (Figure 14) and operating temperatures (Figure 15) of the SiMn and HCFeMn slags. Figure 16a and b compare the values of the volume fraction solids and effective viscosities for the baseline HCFeMn and SiMn slag compositions at the baseline operating temperatures.

Figure 14a illustrates that no suspended solids are estimated for the SiMn slags, but in some cases solids are estimated to be present for the HCFeMn slags having higher basicities and lower operating temperatures (as expected from the calculated liquidus temperatures). HCFeMn slag A stands out (high-MnO slag practice) with the most solids being estimated under normal operating conditions. The behaviour of HCFeMn slag C is also of interest, with significantly lower amounts of Al_2O_3 and highest basicity, with solids precipitation starting at higher basicities and close to the operating point.

42

a) Volume fraction solids
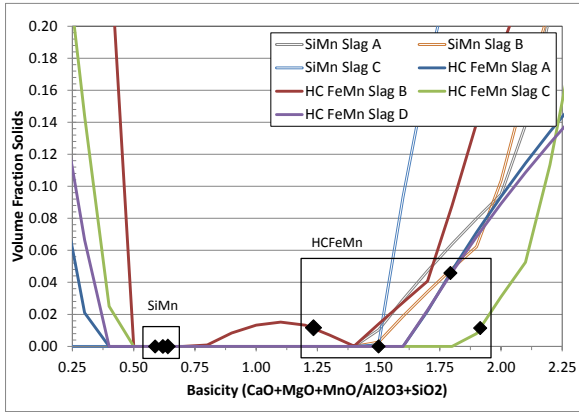
b) Effective viscosity
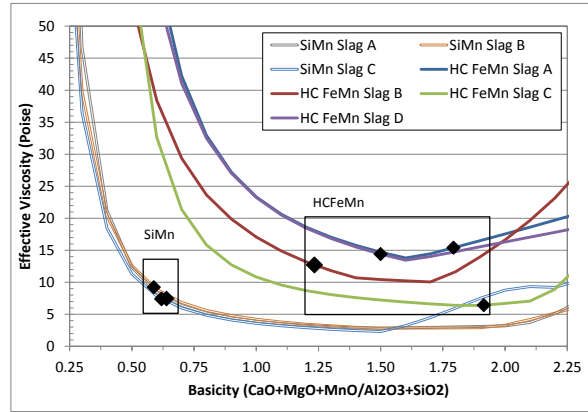
Figure 14 (a) Volume fraction solids and (b) effective viscosity (poise) as functions of basicity (CaO+MgO+MnO/SiO$_2$+Al$_2$O$_3$), calculated using FactSage 6.2 (Bale *et al.* 2009), Urbain model (Mills *et al.* 2011), and the Roscoe equation (Roscoe 1952) with the baseline compositions for HCFeMn slags at 1400°C and SiMn slags at 1600°C shown as points on each series (Table 8).

Estimated effective viscosities, illustrated in Figure 14b, decrease with basicity due to the effect of the bond-breaking monoxides, but increase at higher basicities due to precipitating solids. Viscosities for SiMn and HCFeMn slags are estimated to be in the same order of magnitude at normal conditions, but SiMn slags are estimated to be more sensitive to changing basicity than HCFeMn slags. Less variation is also estimated between the different SiMn slags, due to less variation in the baseline compositions (Figure 14b). The effective viscositiy of HCFeMn slag C is the lowest, due to its high basicity but without significant solids forming at normal operating conditions.

a) Volume fraction solids
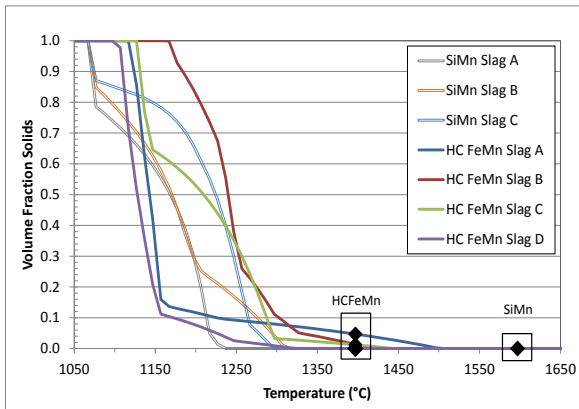
b) Effective viscosity
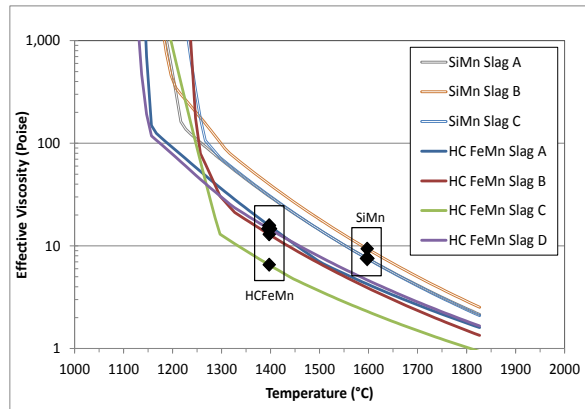
Figure 15 (a) Volume fraction solids and (b) effective viscosity (poise) as functions of temperature, calculated using FactSage 6.2 (Bale *et al.* 2009), Urbain model (Mills *et al.* 2011), and the Roscoe equation (Roscoe 1952) with the baseline compositions for HCFeMn slags at 1400°C and SiMn slags at 1600°C shown as points on each series (Table 8).

Figure 15a also confirms that SiMn slags are further above their liquidus temperatures as compared to HCFeMn slags, for which some precipitated solids are estimated in most cases. In any case, the amounts of precipitated solids are estimated to increase sharply with cooling below the liquidus temperature. The effect of precipitation is seen in Figure 15b, where the effective viscosity increases with cooling from higher temperatures, with an abrupt increase from the liquidus temperature as solids

43

start to precipitate. Noteworthy on Figure 15b is the upward shift of the viscosity curves for typical SiMn slags due to the longer polymer chains resulting from increased SiO_2 content. The viscosity for HCFeMn slag C is again significantly lower due to it having the highest basicity, with the same viscosities as in other practices estimated at around 100 to 150°C lower than the other typical HCFeMn slags.

a) Volume fraction solids

b) Effective viscosity

	HCFeMn A	HCFeMn B	HCFeMn C	HCFeMn D	SiMn A	SiMn B	SiMn C
Vol. Frac. Sol.	4.58%	1.16%	1.15%	0.00%	0.00%	0.00%	0.00%

	HCFeMn A	HCFeMn B	HCFeMn C	HCFeMn D	SiMn A	SiMn B	SiMn C
Viscosity	15.39	12.69	6.42	14.40	7.44	9.21	7.40
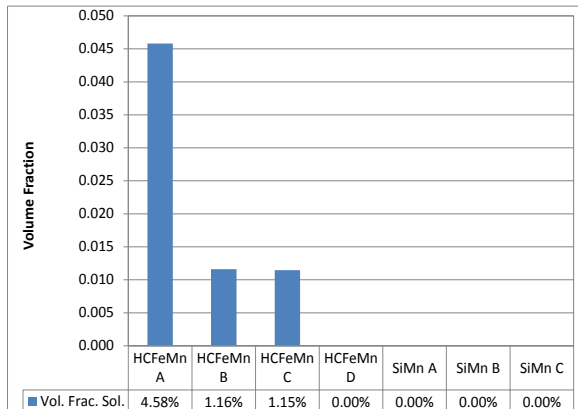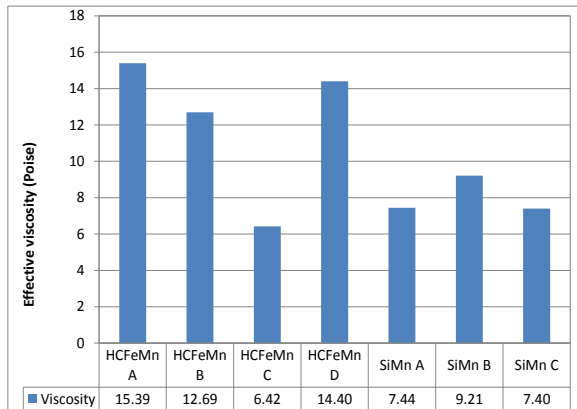
Figure 16 (a) Volume fraction solids and (b) effective viscosities (poise) of typical HCFeMn and SiMn slag compositions (Table 8) estimated using FactSage 6.2 (Bale *et al.* 2009), Urbain model (Mills *et al.* 2011), and the Roscoe equation (Roscoe 1952) at the typical operating temperatures of 1400°C for HCFeMn slags and 1600°C for SiMn slags.

Pseudo-ternary diagrams:

Effective viscosities calculated for the SiO_2-CaO-MnO-Al_2O_3-MgO system with 6% MgO and Al_2O_3/SiO_2 = 0.57 are illustrated on the pseudo-ternary diagrams in Figure 17, Figure 18, and Figure 19 as iso-effective viscosity lines at each temperature (1400, 1500, and 1600°C). Effective viscosities were calculated using FactSage 6.2 (Bale *et al.* 2009), the Urbain model (Mills *et al.* 2011), and the Roscoe equation (Roscoe 1952).

Characteristic on these diagrams is the decrease in viscosity with increasing SiO_2 content, due to less solids being present as fully liquid compositions are approached (at which the lowest viscosities are observed). In the fully liquid slag region the opposite is observed, where viscosities increase due to longer polymer chains forming.

Iso-viscosity lines are located (almost in parallel) around the liquidus compositions. Iso-viscosity lines are spaced more widely in the upper fully liquid slag region, compared to the lower multi-phase region. This indicates that slag viscosity is more sensitive to variations in SiO_2 content when operating below the liquidus temperature, where precipitated solids affect viscosity, as compared to operating above the liquidus temperature where the elongation of polymer chains affects viscosity. The typical SiMn slags are positioned in the single-phase regions where the viscosity is less sensitive to variations in SiO_2, compared to the HCFeMn slags in the multi-phase regions with high sensitivity to variations in SiO_2.

44
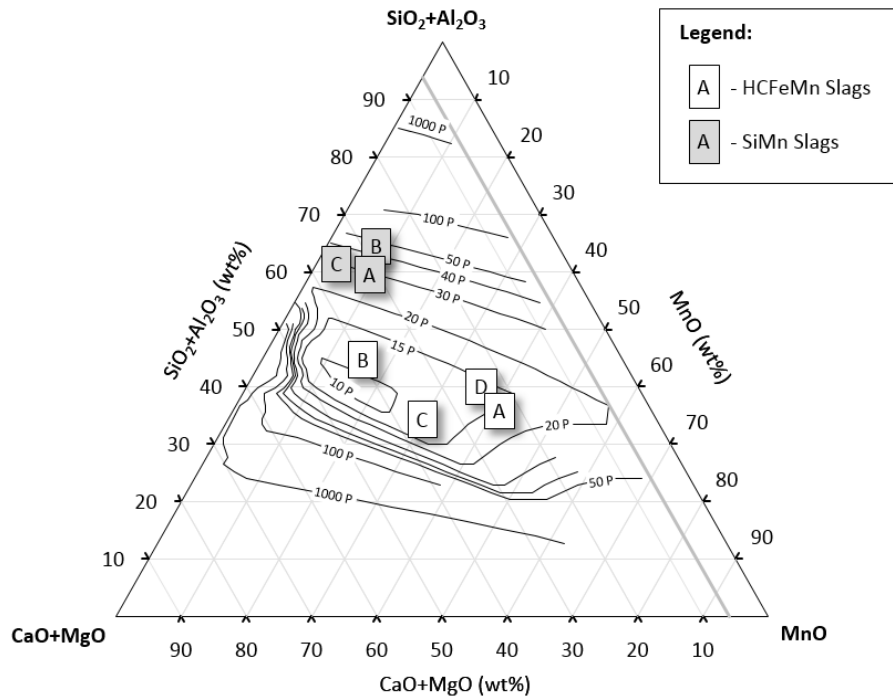
Figure 17 Iso-effective viscosity pseudo-ternary diagram (poise) of the CaO-MnO-SiO₂-Al₂O₃-MgO slag system with 6% MgO and Al₂O₃/SiO₂= 0.57 at 1400°C, showing typical SiMn and HCFeMn slag compositions (Table 8). Calculated using the Urbain model (Mills *et al.* 2011), FactSage 6.2 (Bale *et al.* 2009), and the Roscoe equation (Roscoe 1952).
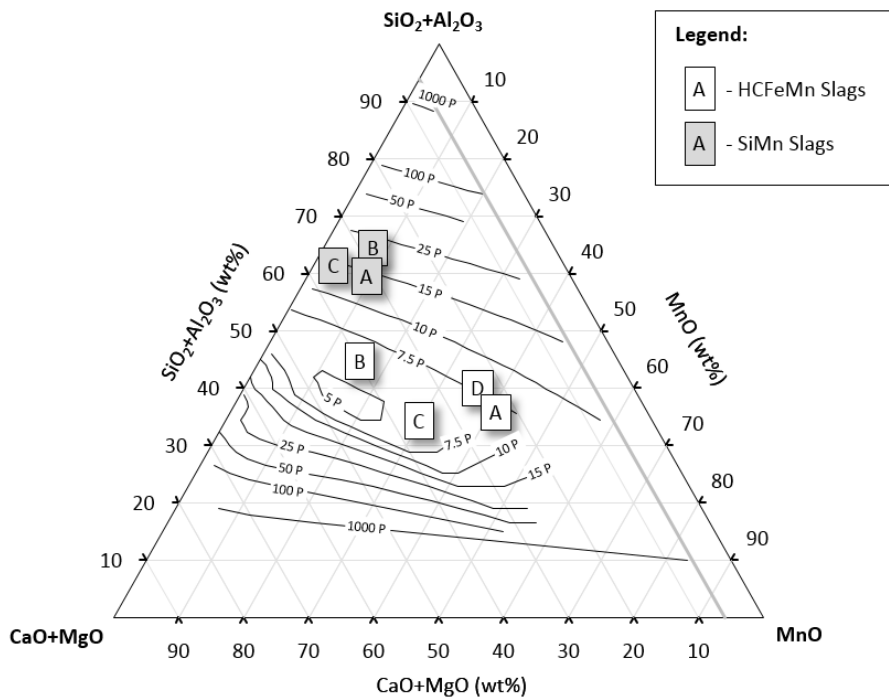
Figure 18 Iso-effective viscosity pseudo-ternary diagram (poise) of the CaO-MnO-SiO₂-Al₂O₃-MgO slag system with 6% MgO and Al₂O₃/SiO₂= 0.57 at 1500°C, showing typical SiMn and HCFeMn slag compositions (Table 8). Calculated using the Urbain model (Mills *et al.* 2011), FactSage 6.2 (Bale *et al.* 2009), and the Roscoe equation (Roscoe 1952).
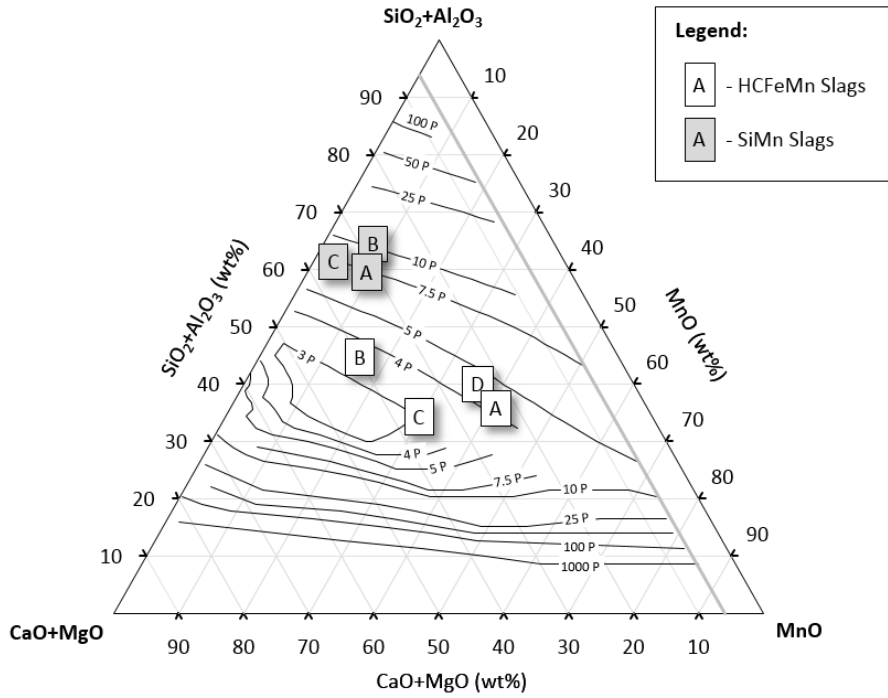
Figure 19 Iso-effective viscosity pseudo-ternary diagram (poise) of the CaO-MnO-SiO$_2$-Al$_2$O$_3$-MgO slag system with 6% MgO and Al$_2$O$_3$/SiO$_2$= 0.57 at 1600°C, showing typical SiMn and HCFeMn slag compositions (Table 8). Calculated using the Urbain model (Mills *et al.* 2011), FactSage 6.2 (Bale *et al.* 2009), and the Roscoe equation (Roscoe 1952).

It is noteworthy that viscosities of typical SiMn slags do not appear to be very sensitive to variations in MnO content (as reduction progresses), compared to most of the HCFeMn slag compositions, where the viscosity is likely to decrease with increasing degree of reduction due to fewer MnO-based precipitated solids being present. SiMn slags with fixed CaO+MgO/SiO$_2$+Al$_2$O$_3$ ratios should display very consistent viscosity behaviour, being not as sensitive to the degree of reduction as might be the case with HCFeMn slags.

4.4   Thermal conductivity

Sensitivity analysis:

Thermal conductivities have been estimated, using the applied models, as functions of basicity (Figure 20a) and temperature (Figure 20b) from the baseline compositions (Table 8). Figure 21 compares the thermal conductivities for the baseline HCFeMn and SiMn slag compositions at the baseline operating temperatures.

For SiMn and HCFeMn slags, thermal conductivities are estimated to decrease with increasing basicity up to basicities of approximately 1.5 (Figure 20a), and then increase again for higher basicities. At lower basicities and at the process temperature a slag would be above its liquidus temperature and therefore fully liquid. Thermal conductivity of liquid slag is then proportional to liquid viscosity, which also decreases with increased basicity (due to the increase in network-breaking basic oxides).

The thermal conductivity of slag below the liquidus temperature is simply obtained from interpolation between the value estimated for solids at the glass transition temperature (assumed 700°C here) and

46

the value estimated for fully liquid slag at the liquidus temperature of the slag. In general, the thermal conductivities of solid slags are higher than that of fully liquid slag, which explains why the value is estimated to increase with basicity at higher basicities where the baseline temperature is below the estimated liquidus temperature.

Considering now the differences in thermal conductivities estimated for typical HCFeMn and SiMn slags over the basicity range (Figure 20a), the baseline points are located at two distinct basicity locations, but have values of the same order of magnitude (0.15 to 0.27 $W.m^{-1}.K^{-1}$). The curves differ in that the thermal conductivities for SiMn slags are lower than for HCFeMn slags with the same basicities (0.25 to 1.4). This is a result of the higher baseline temperature used for SiMn slags (1600°C compared with 1400°C used for HCFeMn slags), since thermal conductivity decreases with temperature for fully liquid slags (Figure 20b).

Also notably different in the higher basicity region (above 1.5) are the curves for HCFeMn slags with low MnO (HCFeMn B) and low Al_2O_3 (HCFeMn C). This is due to the thermal conductivity being interpolated between the liquid values at liquidus temperature and the solid values at the glass transition temperature, both of which are strong functions of chemical composition.

In general, thermal conductivities are estimated to decrease with increasing temperature (Figure 20b). Above the liquidus temperature, the thermal conductivity of liquid slag is proportional to viscosity, which also decreases with temperature. Thermal conductivities of SiMn slags are estimated to be significantly higher than those of HCFeMn slags over the entire temperature range. This is due to SiMn slags having higher SiO_2 contents (higher degrees of polymerisation, longer conductive chains).

a) Function of basicity
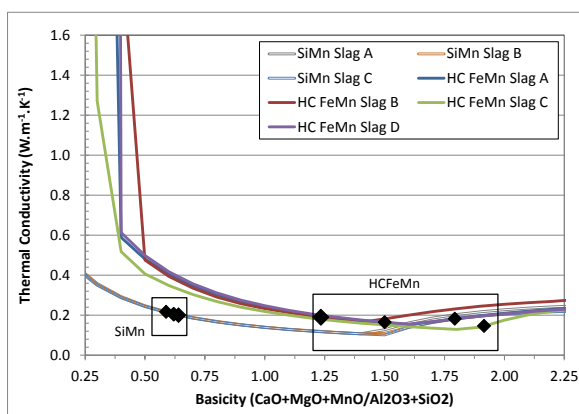
b) Function of temperature
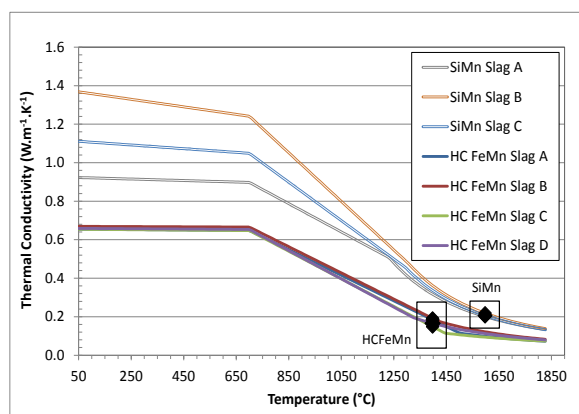
Figure 20 Thermal conductivity as a function of (a) basicity ($CaO+MgO+MnO/SiO_2+Al_2O_3$) at the typical operating temperatures of 1400°C for HCFeMn slags and 1600°C for SiMn slags, and (b) temperature (°C), calculated using reported models (Mills *et al.* 2011) and FactSage 6.2 (Bale *et al.* 2009), showing values for baseline compositions as points (Table 8).
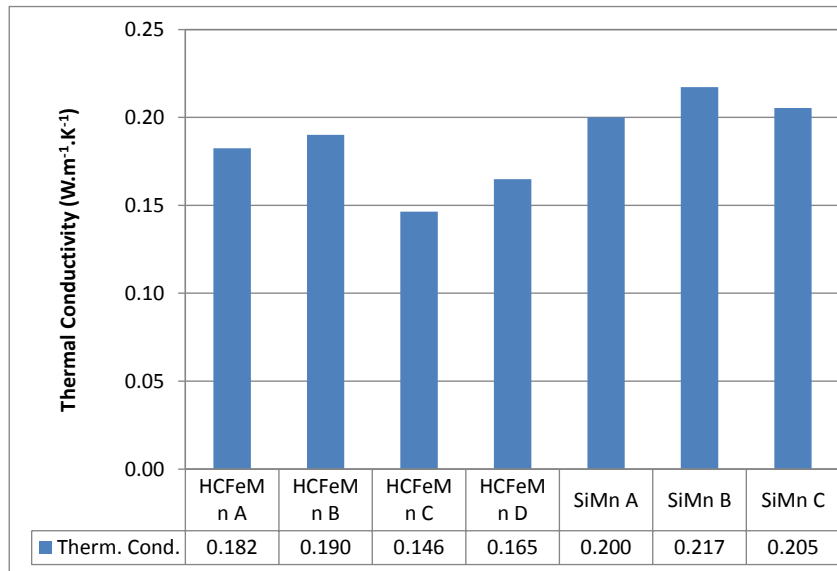
Figure 21 Estimated thermal conductivities of typical HCFeMn and SiMn slag compositions (Table 8) using the models by Mills *et al.* (2011) at the typical operating temperatures of 1400°C for HCFeMn slags and 1600°C for SiMn slags.

Pseudo-ternary diagrams:

Thermal conductivities calculated for the SiO_2-CaO-MnO-Al_2O_3-MgO system with 6% MgO and Al_2O_3/SiO_2 = 0.57 are illustrated on the pseudo-ternary diagrams in Figure 22, Figure 23, and Figure 24 as iso-thermal conductivity lines at each temperature (1400, 1500, and 1600°C). These were calculated using the thermal conductivity models by Mills *et al.* (2011), and phase fractions estimated with FactSage 6.2 (Bale *et al.* 2009) to estimate liquidus temperatures.

Similarities are observed between these and the viscosity pseudo-ternary diagrams (Figure 17 to Figure 19), with thermal conductivities being the lowest around the liquidus composition and increasing towards both high and low SiO_2 contents. A cross-section of these plots around MnO contents between 20 to 40% would have a shape similar to Figure 20a. As in Figure 20b, lower thermal conductivities are estimated at the higher temperatures, and minimum values are estimated around the liquidus compositions.

Thermal conductivities of both typical SiMn and HCFeMn slags do not appear to be very sensitive to varying degrees of MnO reduction.

48
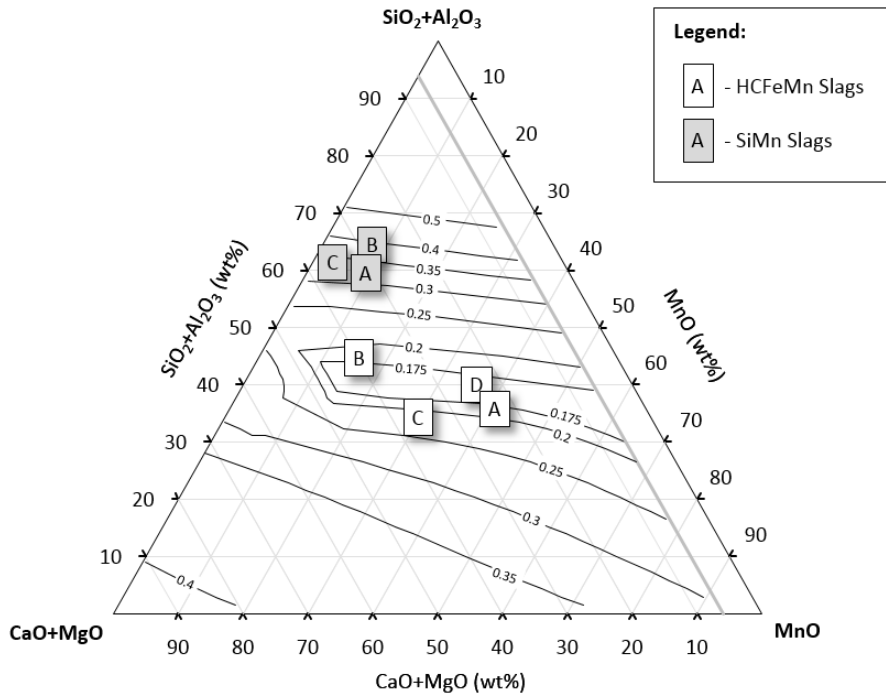
Figure 22 Iso-thermal conductivity pseudo-ternary diagram ($W.m^{-1}.K^{-1}$) of the $CaO-MnO-SiO_2-Al_2O_3-MgO$ slag system with 6% MgO and $Al_2O_3/SiO_2= 0.57$ at 1400°C, showing typical SiMn and HCFeMn slag compositions (Table 8). Calculated using the models by Mills *et al.* (2011).
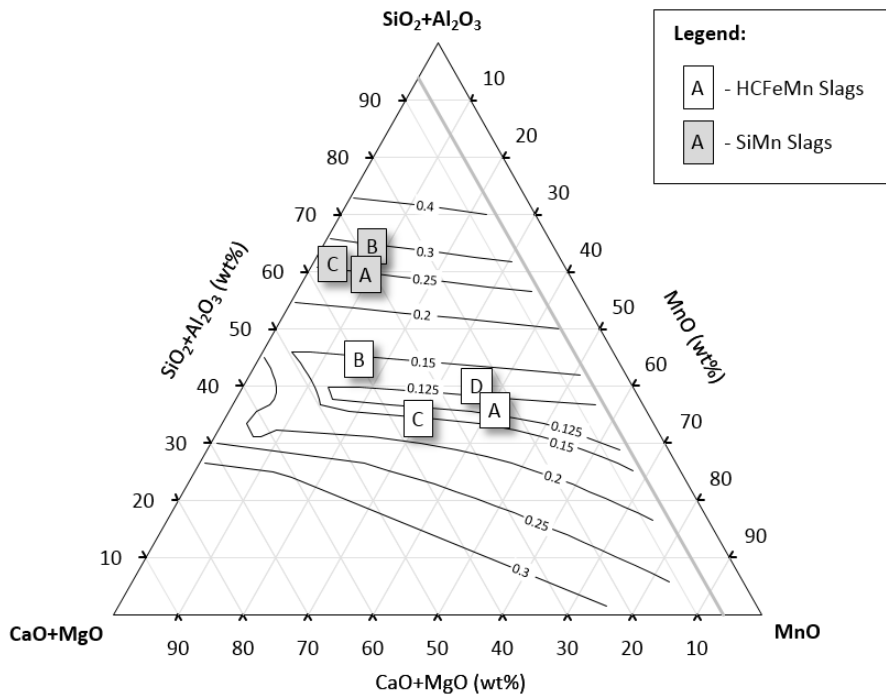
Figure 23 Iso-thermal conductivity pseudo-ternary diagram ($W.m^{-1}.K^{-1}$) of the $CaO-MnO-SiO_2-Al_2O_3-MgO$ slag system with 6% MgO and $Al_2O_3/SiO_2= 0.57$ at 1500°C, showing typical SiMn and HCFeMn slag compositions (Table 8). Calculated using the models by Mills *et al.* (2011).

49
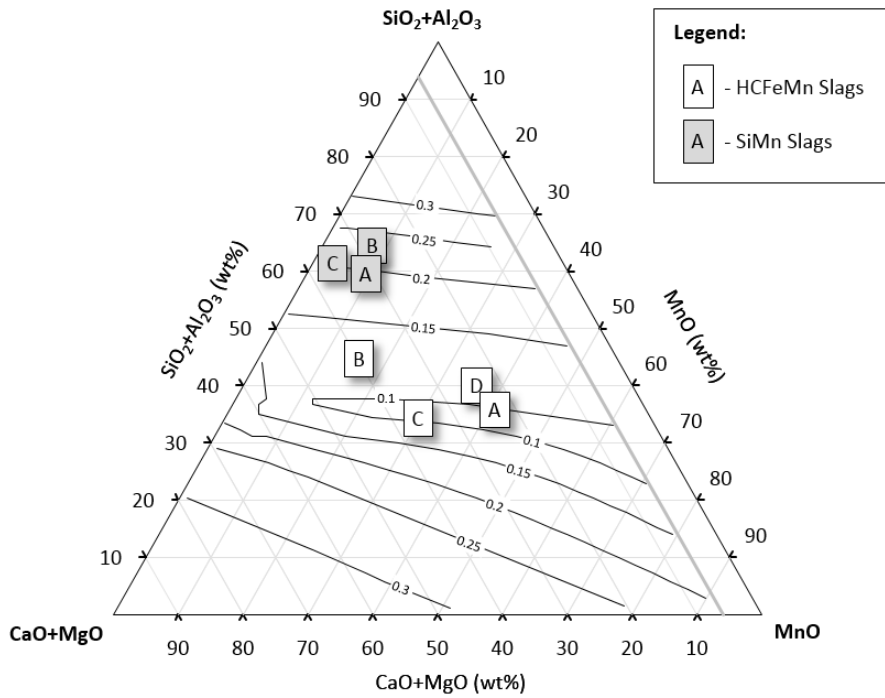
Figure 24 Iso-thermal conductivity pseudo-ternary diagram (W.m^{-1}.K^{-1}) of the CaO-MnO-SiO$_2$-Al$_2$O$_3$-MgO slag system with 6% MgO and Al$_2$O$_3$/SiO$_2$= 0.57 at 1600°C, showing typical SiMn and HCFeMn slag compositions (Table 8). Calculated using the models by Mills *et al.* (2011).

4.5 Density

Sensitivity analysis:

Densities of slags have been estimated as functions of basicity (Figure 25a) and temperature (Figure 25b), using the applied models. On Figure 26 the densities are compared for the baseline HCFeMn and SiMn slag compositions at the baseline operating temperatures.

Densities are estimated to increase slightly with basicity (Figure 25a) as a result of the lower molar volumes and higher densities of constituents with higher basicities (basic oxides) (Table 7). Over the basicity range (Figure 25a), densities of typical SiMn slags are estimated to be significantly lower than typical HCFeMn slags, due largely to the difference in baseline temperatures for which the results were calculated (1400°C for HCFeMn slags and 1600°C for SiMn slags), as well as the higher SiO$_2$ contents with high molar volumes and lower MnO contents for SiMn slags (Table 7).

The slags HCFeMn A and HCFeMn D have higher estimated densities at 1400°C compared to HCFeMn B and HCFeMn C, probably because HCFeMn B has a high Al$_2$O$_3$ content and HCFeMn C a fairly low MnO content.

Density in general is estimated to decrease with temperature (Figure 25b) due to thermal expansion, and due to the liquids having lower densities than solids. Above the liquidus temperature, density would decrease more rapidly, since liquid slag has a larger thermal expansion coefficient. Densities of the typical HCFeMn slags are estimated to be higher due to the lower SiO$_2$ contents and higher MnO contents compared to SiMn slags.

50

At typical process temperatures the estimated densities of the HCFeMn slags vary over a wider range (2700 to 3000 kg.m^{-3}) than those of SiMn slags (2500 kg.m^{-3}). Considering the changes with temperature (related to thermal expansion coefficient), it can be concluded from Figure 25a that these density differences of typical slags from HCFeMn and SiMn operations are due mostly to differences in chemical composition, rather than operating temperature.
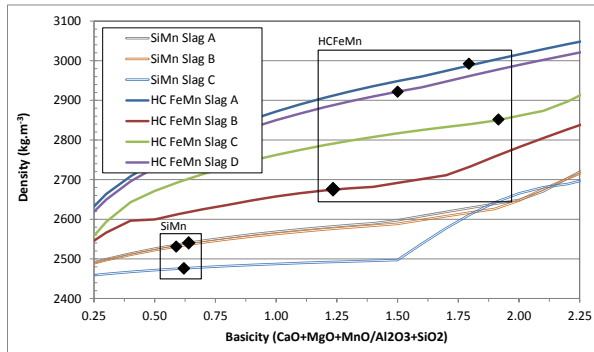
a) Function of basicity   b) Function of temperature
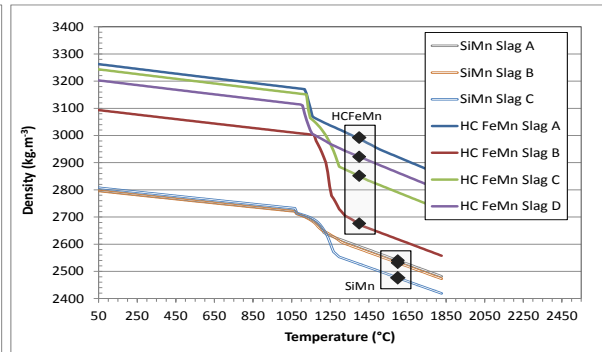
Figure 25 Density as a function of (a) basicity (CaO+MgO+MnO/SiO$_2$+Al$_2$O$_3$) at the typical operating temperatures of 1400°C for HCFeMn slags and 1600°C for SiMn slags, and (b) temperature (°C), calculated using reported models (Mills *et al.* 2011) and FactSage 6.2 (Bale *et al.* 2009), showing values for baseline compositions as points (Table 8).
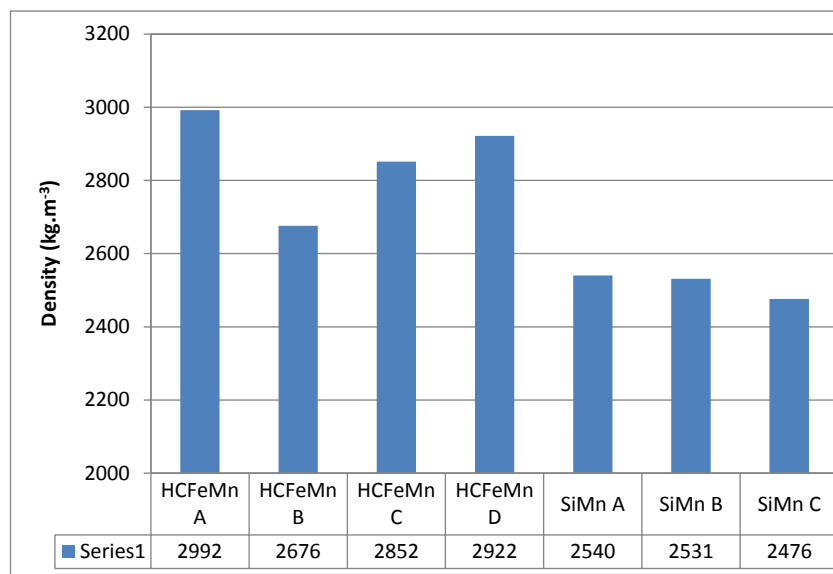
Figure 26 Densities estimated for typical HCFeMn and SiMn slag compositions (Table 8) using the models by Mills *et al.* (2011) at the typical operating temperatures of 1400°C for HCFeMn slags and 1600°C for SiMn slags.

Pseudo-ternary diagrams:

Densities calculated for the SiO$_2$-CaO-MnO-Al$_2$O$_3$-MgO system with 6% MgO and Al$_2$O$_3$/SiO$_2$ = 0.57 are illustrated on the pseudo-ternary diagrams in Figure 27, Figure 28, and Figure 29 as iso-density lines at each temperature (1400, 1500, and 1600°C). These were calculated with the density models at the different temperatures as functions of chemical composition (Mills *et al.* 2011), and using FactSage 6.2 (Bale *et al.* 2009) to estimate the liquidus temperatures.

51

The orientations of the curves on these diagrams are distinctively different from those for viscosity and thermal conductivity. At higher $Al_2O_3+SiO_2/MgO+CaO$, ratios, density is fairly insensitive to this ratio, but varies mostly with MnO content. This is due to MnO having the lowest molar volume and largest molar mass (i.e. highest density) in the density model used. Should a section of constant MnO be constructed through one of these diagrams, a curve similar to Figure 25a would be obtained, where density increases slightly with basicity.

At lower $Al_2O_3+SiO_2$ contents (essentially below the liquidus temperature) densities are higher due to the higher densities of the precipitated solids, and are shown to be sensitive mostly to the amounts of $Al_2O_3+SiO_2$.

Only small differences are estimated between the plots for different temperatures, due to the very small thermal expansion coefficients. This again shows that density differences between the HCFeMn and SiMn slags are due more to chemical composition than to temperature.
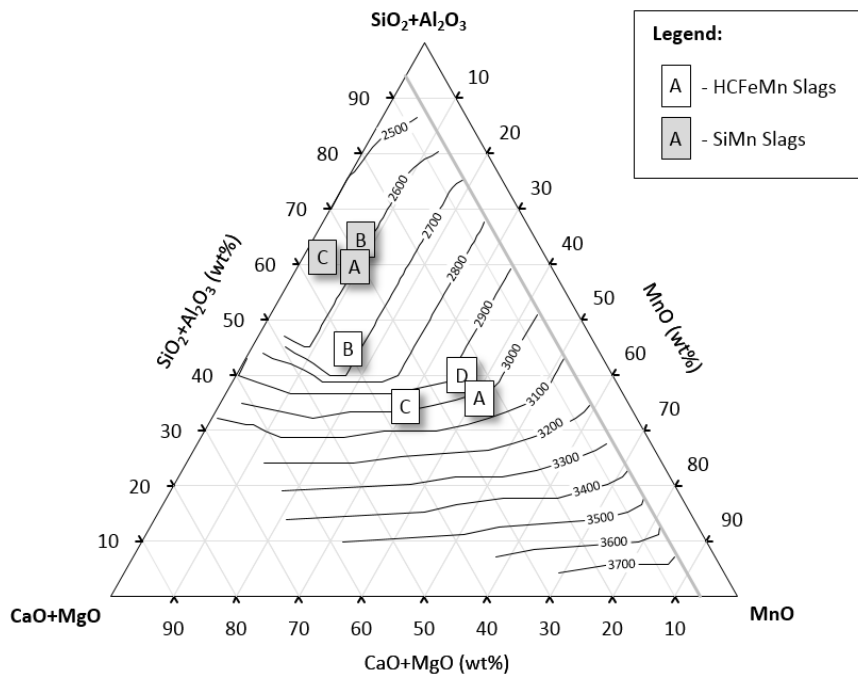
Figure 27 Iso-density pseudo-ternary diagram (kg.m^{-3}) of the CaO-MnO-SiO$_2$-Al$_2$O$_3$-MgO slag system with 6% MgO and Al$_2$O$_3$/SiO$_2$= 0.57 at 1400°C, showing typical SiMn and HCFeMn slag compositions (Table 8). Calculated using the models by Mills *et al.* (2011).
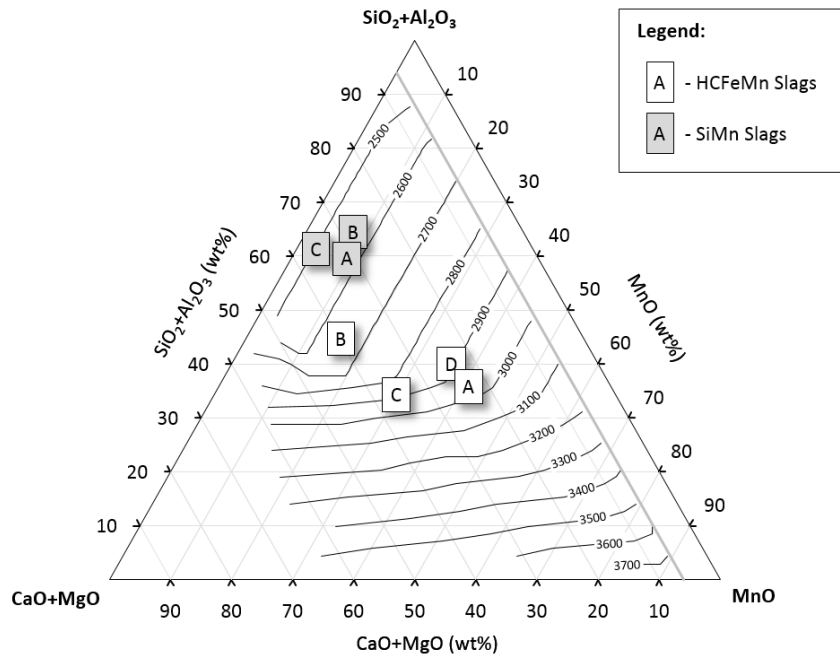
Figure 28 Iso-density pseudo-ternary diagram (kg.m^{-3}) of the CaO-MnO-SiO$_2$-Al$_2$O$_3$-MgO slag system with 6% MgO and Al$_2$O$_3$/SiO$_2$= 0.57 at 1500°C, showing typical SiMn and HCFeMn slag compositions (Table 8). Calculated using the models by Mills *et al.* (2011).
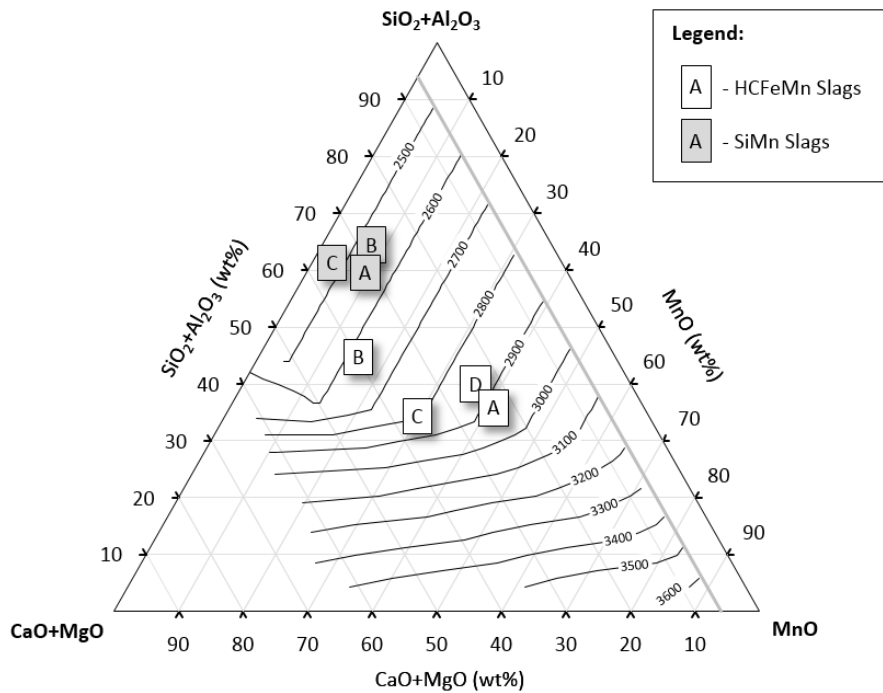
Figure 29 Iso-density pseudo-ternary diagram (kg.m^{-3}) of the CaO-MnO-SiO$_2$-Al$_2$O$_3$-MgO slag system with 6% MgO and Al$_2$O$_3$/SiO$_2$= 0.57 at 1600°C, showing typical SiMn and HCFeMn slag compositions (Table 8). Calculated using the models by Mills *et al.* (2011).

4.6   Heat capacity and enthalpy

Model evaluation:

Solid and liquid heat capacities estimated for typical HCFeMn and SiMn slags (Table 8) are compared in Figure 30 for the different models used. Heat capacities of solid slags are estimated to be

53

approximately 12% higher for typical SiMn slags than for HCFeMn slags (Figure 30a), due to the relatively high partial heat capacity of SiO_2 and its higher content in typical SiMn slags. On average, the heat capacities derived from the FactSage 6.2 (Bale *et al.* 2009) results are 8% higher than those estimated with the models by Mills (Mills *et al.* 2011) (Figure 30a).

Heat capacities of liquid slags are estimated to be on average 7% higher for typical SiMn slags compared to HCFeMn slags (Figure 30b). Heat capacities estimated with the models by Mills (Mills *et al.* 2011) are significantly higher (approximately 21%) than those with the models by by Björkvall (Björkvall *et al.* 2001) and FactSage 6.2 (Bale *et al.* 2009).

The higher heat capacities of typical solid and liquid SiMn slags imply that in heat and mass flow applications, smaller temperature responses would be observed for specific amounts of heat transferred in comparison with HCFeMn slags. Other temperature-dependent properties would then be affected, and in turn the flow of heat and mass. SiMn slags are therefore expected to be less sensitive to heating and cooling than HCFeMn slags.

a) Solid heat capacity

b) Liquid heat capacity

	HCFeMn A	HCFeMn B	HCFeMn C	HCFeMn D	SiMn A	SiMn B	SiMn C
Mills	928.8	996.2	942.1	938.6	1033.3	1034.5	1037.8
FactSage	962.8	1082.5	974.9	969.6	1110.1	1140.9	1196.6

	HCFeMn A	HCFeMn B	HCFeMn C	HCFeMn D	SiMn A	SiMn B	SiMn C
Mills	1364.5	1439.5	1401.8	1360.5	1492.1	1473.3	1482.7
Björkvall	1085.1	1148.2	1082.4	1094.4	1208.6	1210.2	1207.7
FactSage	1179.8	1214.6	1172.7	1168.4	1260.2	1254.2	1241.3
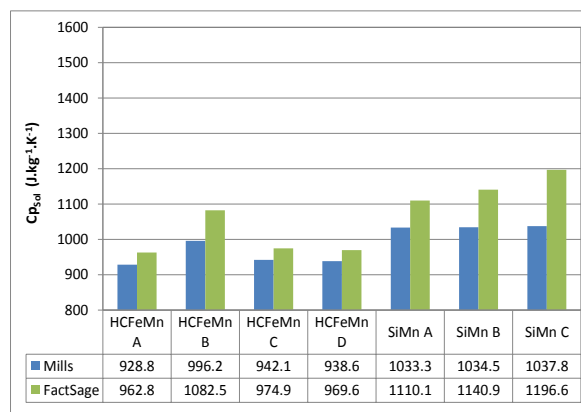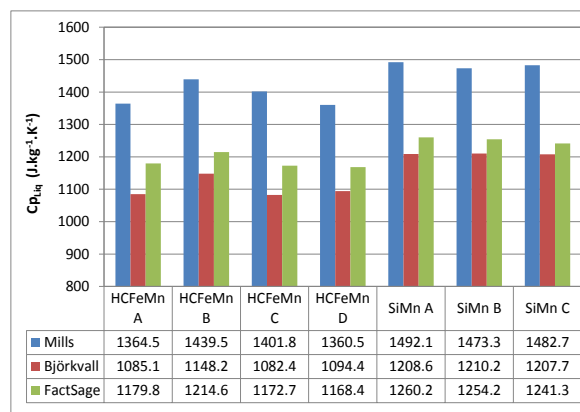
Figure 30 Heat capacities ($J.kg^{-1}.K^{-1}$) estimated for (a) solid and (b) liquid slags of typical HCFeMn and SiMn slag compositions (Table 8) using models by Mills *et al.* (2011), Björkvall *et al.* (2001*)*, and FactSage 6.2 (Bale *et al.* 2009).

Enthalpies estimated at 298 K with FactSage, and the heats of melting at the estimated liquidus temperatures for typical slag compositions (Table 8) are illustrated in Figure 31. Enthalpies at 298 K of typical SiMn slags were estimated to be lower than for typical HCFeMn slags (Figure 31a). For the HCFeMn slags, the heats of melting estimated with the models by Mills (Mills *et al.* 2011) differed inconsistently from those derived from the FactSage 6.2 results (Bale *et al.* 2009), whereas for the SiMn slags the FactSage-derived values were significantly higher.

a) Enthalpy at 298K

	HCFeMn A	HCFeMn B	HCFeMn C	HCFeMn D	SiMn A	SiMn B	SiMn C
FactSage	-1.10E+07	-1.31E+07	-1.17E+07	-1.15E+07	-1.42E+07	-1.43E+07	-1.46E+07

b) Heat of melting

	HCFeMn A	HCFeMn B	HCFeMn C	HCFeMn D	SiMn A	SiMn B	SiMn C
Mills	5.36E+05	5.87E+05	5.03E+05	4.87E+05	4.30E+05	4.69E+05	4.77E+05
FactSage	6.09E+05	5.29E+05	4.96E+05	5.67E+05	6.38E+05	6.07E+05	5.54E+05
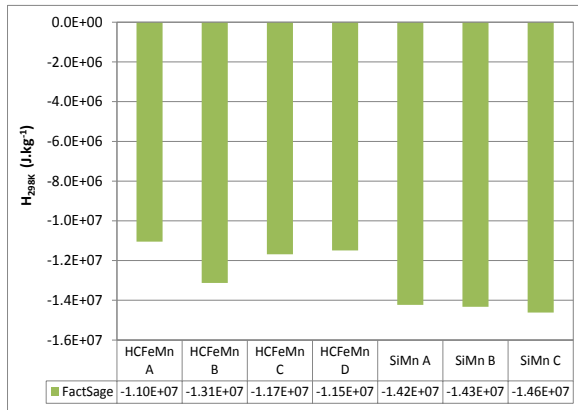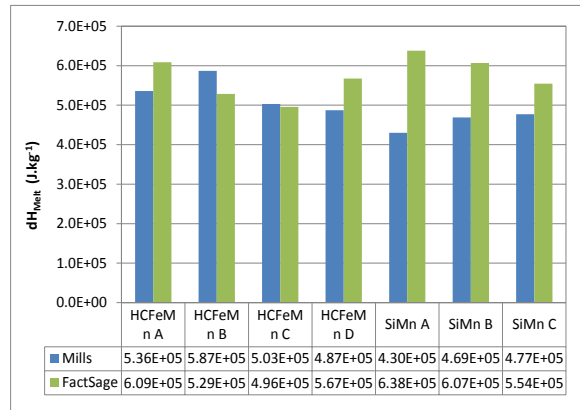
Figure 31 (a) Enthalpies at 298K (J.kg^{-1}), and (b) heat of melting (J.kg^{-1}) of typical HCFeMn and SiMn slag compositions (Table 8) estimated using models by Mills *et al.* (2011), and FactSage 6.2 (Bale *et al.* 2009) (where applicable).

<u>Sensitivity analysis:</u>

To further compare the models by Mills and FactSage and the behaviour for varying temperature and basicity, $H_T - H_{298K}$ values were derived using both these models over the temperature and basicity range using the typical SiMn and HCFeMn compositions as a baseline (Table 8). The $(H_T - H_{298K})$ values estimated using the models by Mills are illustrated in Figure 32, and those calculated with FactSage in Figure 33. In Figure 32a, distinctive step changes are observed in the estimated values as functions of basicity. This is due to the large differences in enthalpies for solids and liquids estimated by the model of Mills (Mills *et al.* 2011). With increasing basicity the liquidus temperatures generally increase, and a step change to a lower enthalpy would indicate the basicity from which the slag is estimated to be solid at the relevant temperature. For the HCFeMn slags, the liquidus temperatures were estimated to increase at the very low basicities considered, and therefore the enthalpies are lower at these points. Generally, as functions of basicity (Figure 32a and Figure 33a) the enthalpies of SiMn slags are distinctly higher than those of HCFeMn slags, due to the higher assumed operating temperature of 1600°C, compared to 1400°C for HCFeMn slags.

Enthalpies increase with temperature as the internal energy increases (Figure 32b and Figure 33b), with the step changes in enthalpies around the liquidus temperature representing the heat required for the phase change. In the case of the FactSage results (Figure 33b) there is no sudden step change, but a gradual increase in enthalpy between the solidus and liquidus temperatures due to increasing amounts of liquid being estimated from the solidus temperature. In the solid and liquid regions of these enthalpies plotted as functions of temperature (Figure 32a and Figure 33a) the slopes remain mostly constant, indicating that the heat capacity variation with temperature is very small.

55

a) Function of basicity
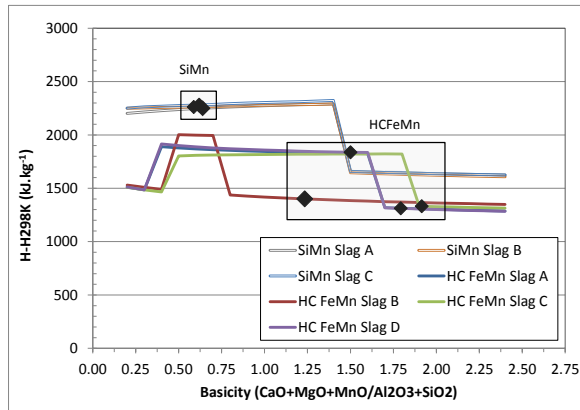
b) Function of temperature
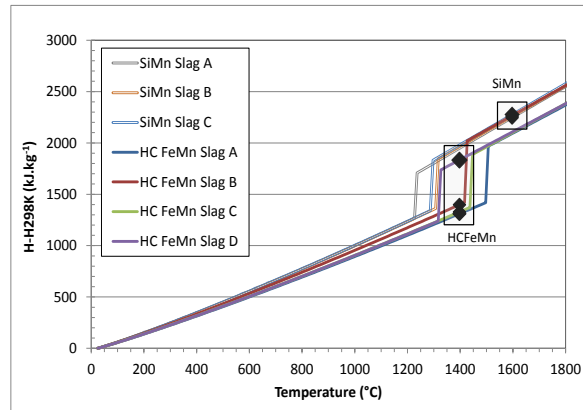
Figure 32 ($H_T - H_{298K}$) as a function of (a) basicity (CaO+MgO+MnO/SiO$_2$+Al$_2$O$_3$) at the typical operating temperatures of 1400°C for HCFeMn slags and 1600°C for SiMn slags, and (b) temperature (°C), calculated using models by Mills *et al.* (2011).

a) Function of basicity
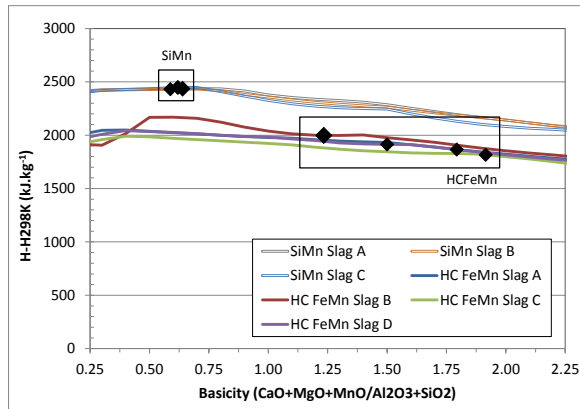
b) Function of temperature
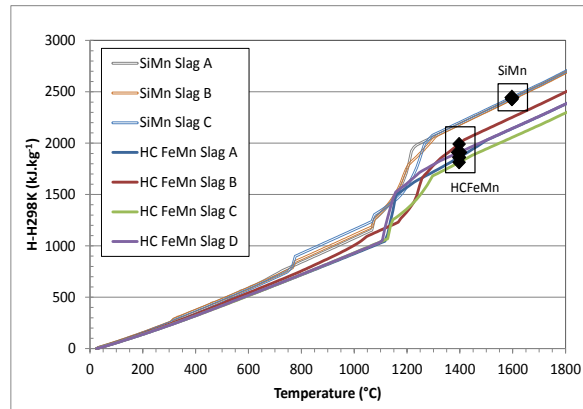
Figure 33 ($H_T - H_{298K}$) as a function of (a) basicity (CaO+MgO+MnO/SiO$_2$+Al$_2$O$_3$) at the typical operating temperatures of 1400°C for HCFeMn slags and 1600°C for SiMn slags, and (b) temperature (°C), calculated using FactSage 6.2 (Bale *et al.* 2009).

Pseudo-ternary diagrams:

Heat capacities calculated for the SiO$_2$-CaO-MnO-Al$_2$O$_3$-MgO system with 6% MgO and Al$_2$O$_3$/SiO$_2$ = 0.57 are illustrated on the pseudo-ternary diagrams in Figure 34, Figure 35, and Figure 36 as iso-heat capacity lines at each temperature (1400, 1500, and 1600°C). These were calculated with the heat capacity models at the different temperatures as functions of chemical composition (Mills *et al.* 2011), and using FactSage 6.2 (Bale *et al.* 2009) to estimate the liquidus temperatures.

The transition from solid to liquid with increasing amounts of SiO$_2$ and Al$_2$O$_3$ can be clearly observed between 30 to 50% SiO$_2$+Al$_2$O$_3$. Across this liquid transformation line the increase in heat capacity is estimated to be approximately 200 to 300 J.kg^{-1}.K^{-1}. Below the liquidus compositions (lower amounts of SiO$_2$+Al$_2$O$_3$), heat capacities are estimated to increase mostly with increasing amounts of SiO$_2$+Al$_2$O$_3$ and with decreasing amounts of MnO, having a range of approximately 200 J.kg^{-1}.K^{-1}. In the liquid

56

region (above liquidus compositions) heat capacity is estimated to vary with MnO content, and is also higher for lower MnO contents with a range of only approximately 100 J.kg^{-1}.K^{-1}.
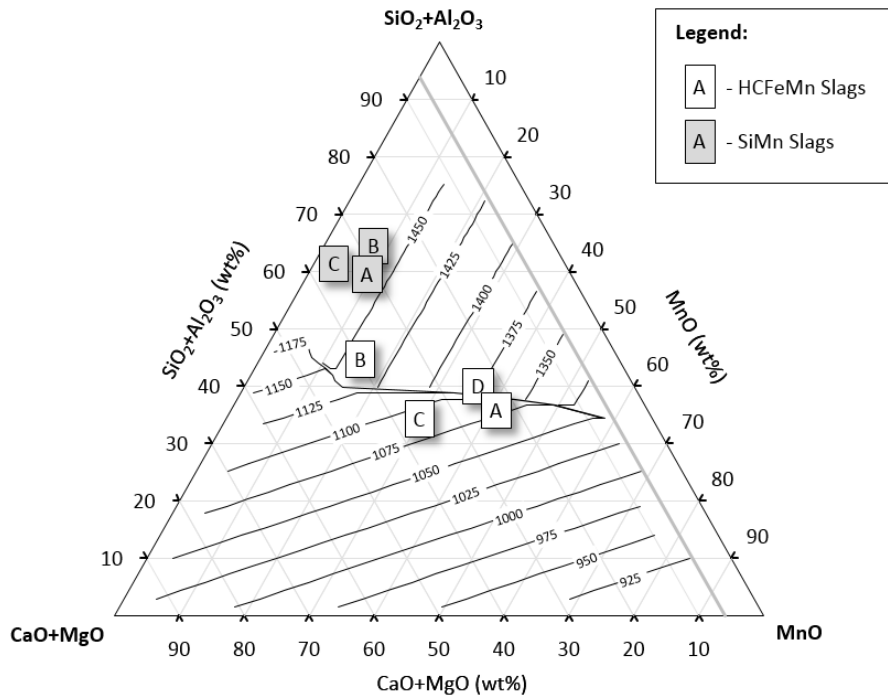
Figure 34 Iso-heat capacity pseudo-ternary diagram (J.kg^{-1}.K^{-1}) of the CaO-MnO-SiO$_2$-Al$_2$O$_3$-MgO slag system with 6% MgO and Al$_2$O$_3$/SiO$_2$= 0.57 at 1400°C, showing typical SiMn and HCFeMn slag compositions (Table 8). Calculated using the models by Mills *et al.* (2011).
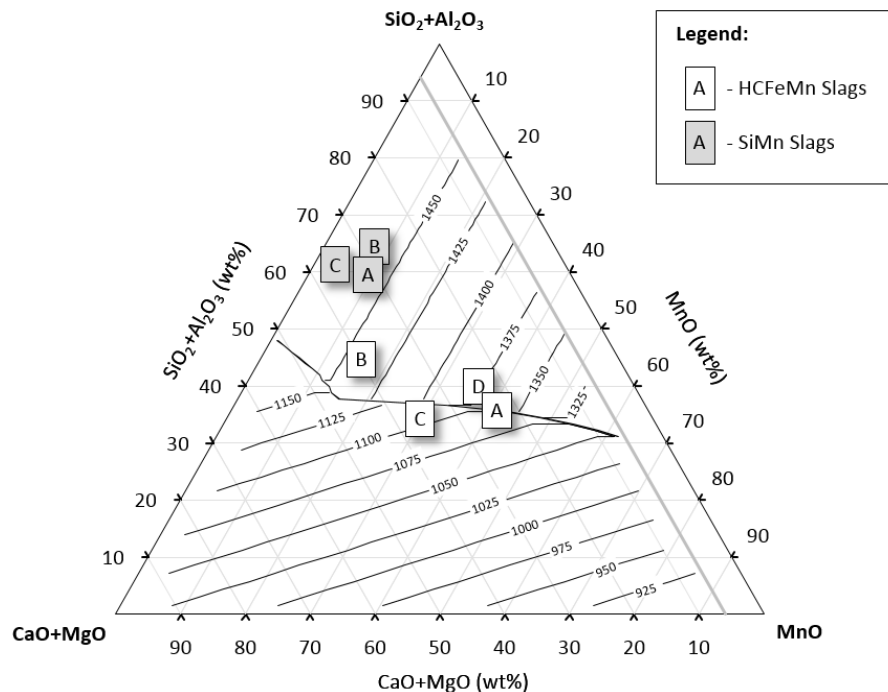
Figure 35 Iso-heat capacity pseudo-ternary diagram (J.kg^{-1}.K^{-1}) of the CaO-MnO-SiO$_2$-Al$_2$O$_3$-MgO slag system with 6% MgO and Al$_2$O$_3$/SiO$_2$= 0.57 at 1500°C, showing typical SiMn and HCFeMn slag compositions (Table 8). Calculated using the models by Mills *et al.* (2011).

57
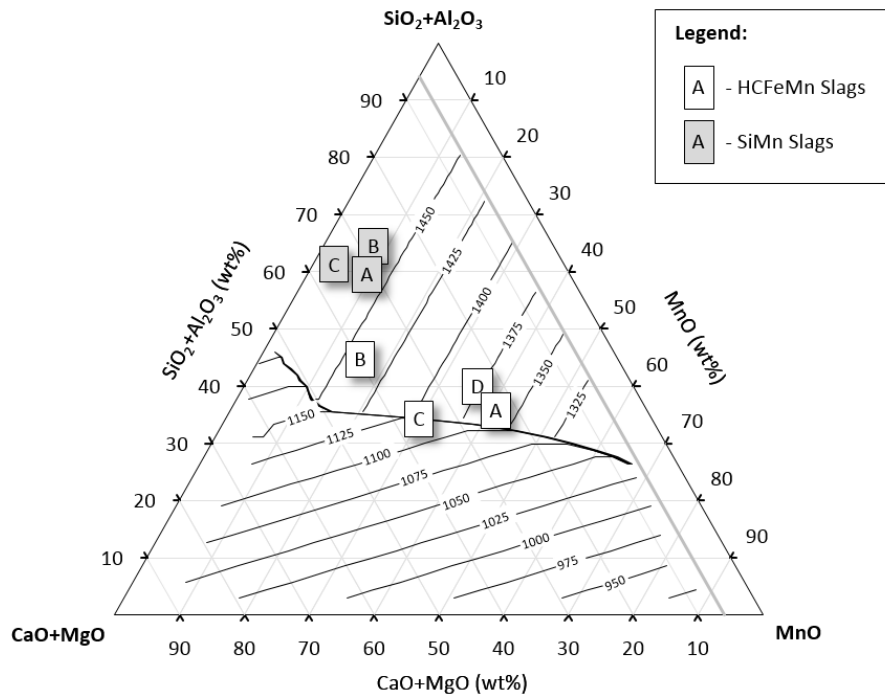
Figure 36 Iso-heat capacity pseudo-ternary diagram $(J.kg^{-1}.K^{-1})$ of the $CaO-MnO-SiO_2-Al_2O_3-MgO$ slag system with 6% MgO and Al_2O_3/SiO_2= 0.57 at 1600°C, showing typical SiMn and HCFeMn slag compositions (Table 8). Calculated using the models by Mills *et al.* (2011).

4.7   Summary

The values of the slag properties at the standard operating temperatures of 1400°C for HCFeMn slags and 1600°C for SiMn slags are summarised in Table 10. These property values were used in further tap flow modelling in which the typical slags with the compositions as in Table 8 were evaluated.

Table 10 Summary of slag physicochemical properties calculated for the typical slag compositions (Table 8) – HCFeMn slags at 1400°C and SiMn slags at 1600°C.

|	Solidus temperature (°C)	Liquidus temperature (°C)	Density (kg.m⁻³)	Effective viscosity (P)	Thermal conductivity (W.m⁻¹.K⁻¹)	Heat capacity solid (J.kg⁻¹.K⁻¹)	Heat capacity liquid (J.kg⁻¹.K⁻¹)
HCFeMn Slag A	1122	1501	2992	15.4	0.182	963	1180
HCFeMn Slag B	1167	1419	2676	12.7	0.190	1083	1215
HCFeMn Slag C	1129	1444	2852	6.4	0.146	975	1173
HCFeMn Slag D	1106	1323	2922	14.4	0.165	970	1168
SiMn Slag A	1072	1233	2540	7.4	0.200	1110	1260
SiMn Slag B	1075	1310	2531	9.2	0.217	1141	1254
SiMn Slag C	1072	1296	2476	7.4	0.205	1197	1241

Viscosity:

- The latest Urbain formalism model (Mills *et al.* 2011) produced acceptable results and is used in subsequent evaluations, together with estimations of amounts of precipitated solids (using FactSage 6.2) at 1600°C for SiMn slags and 1400°C for HCFeMn slags.

- At operating temperatures of 1600°C, typical SiMn slags have no precipitated solids and slightly lower viscosities, compared to typical HCFeMn slags at 1400°C which have small amounts of solids and slightly higher viscosities.

58

- An increase in basicity would cause decreasing viscosities of typical SiMn slags due to network-breaking monoxides, while viscosity tends to increase with increased basicity for HCFeMn slags as monoxide phase solids precipitate.

- Above the liquidus temperature, viscosity increases with increased SiO_2 content as the longer polymer chains cause resistance to flow, while below the liquidus temperature higher SiO_2 contents lead to fewer flow-hindering precipitated solids.

- Typical SiMn slags appear to be fairly insensitive to MnO content, while the viscosity of HCFeMn slags could decrease with increased MnO reduction, as less MnO-containing solids would precipitate at higher degrees of reduction.

Thermal conductivity:

- Thermal conductivity models reported by Mills *et al.* (2011) have been used, and the liquidus temperature was estimated with FactSage 6.2.

- At operating temperatures of 1600°C, typical SiMn slags have slightly higher thermal conductivities compared to typical HCFeMn slags at 1400°C.

- At lower basicities, thermal conductivity decreases with increasing basicity as increasing concentrations of monoxides break up the conductive silicate chains. This also causes the viscosity to decrease. At higher basicities the thermal conductivity increases due the precipitation of conductive solids.

- Thermal conductivity decreases slightly with increasing temperature from ambient up to the liquidus temperature, beyond which it decreases sharply due to the formation of the less conductive liquid phase.

- Over the temperature range studied, the thermal conductivity of SiMn slags is significantly higher than that of HCFeMn slags, as the higher SiO_2 content in the SiMn slags lead to higher degrees of polymerisation and longer and more conductive chains.

- Thermal conductivities of both typical SiMn and HCFeMn slags do not appear to be very sensitive to differences in the degree of MnO reduction.

Density:

- Density models reported by Mills (Mills *et al.* 2011, Slag Atlas 1995) have been used, and volume fractions of solids were estimated with FactSage 6.2. Models are based on partial molar volumes at 25°C and 1500°C, and constant thermal expansion coefficients up to the glass transition temperature and above the melting temperature.

- In the model, MnO and other basic oxides have lower partial molar volumes compared with SiO_2 and Al_2O_3. The result is that density increases with basicity, and typical SiMn slags have significantly lower densities than typical HCFeMn slags.

- Density is also estimated to be fairly insensitive to basicity ($SiO_2+Al_2O_3/MgO+CaO$), and more sensitive to MnO content (with smaller partial molar volume). Density therefore decreases significantly as MnO reduction occurs.

Heat capacity, enthalpy:

- Heat capacity models by Mills *et al.* (2011) have been used, with temperature-dependent heat capacities of the solid constituents and constant values for the liquid phase. FactSage 6.2 (Bale *et al.* 2009) has been used to estimate the liquidus temperatures and enthalpies of the resulting mixtures at different temperatures.

- For comparative purposes ($H_T - H_{298K}$) was derived, but heat capacities, enthalpies at 298 K, and heats of melting were all calculated as would be required in heat and fluid flow modelling.

- Consistently higher heat capacities were estimated for liquid slags, compared to solid slags. For SiMn slags, slightly higher heat capacities were estimated (especially for solids) than for HCFeMn slags.

- Enthalpies at 298 K of typical SiMn were estimated to be slightly lower than those of HCFeMn slags, although no firm conclusions could be drawn about the heats of melting estimated for each.

- Pseudo-ternary diagrams indicated that heat capacities increase mostly as MnO reduction progresses. Below liquidus temperatures, heat capacity is also somewhat dependent on the SiO_2 and Al_2O_3 content of the slag.

5 Tapping flow model formulation

5.1 Blast furnace fluid flow model

Tapping from a furnace can be modelled in detail using CFD, estimating and investigating specific aspects of fluid flow and heat transfer. A simpler analytical modelling approach is considered here, which was reported by Iida *et al.* (2008) who modelled the draining of molten iron and slag through a blast furnace taphole. The formulation of this model is discussed here as it was applied, and later used as the basis for the development of an improved model.

The domain of the model is illustrated in Figure 37, showing the simplified taphole region of a blast furnace consisting of a cylinder that represents the taphole together with a layer of porous media representing the coke particles ("coke filter") on the hot-face side of the taphole. The pressure drop is calculated for the slag and metal flowing through these two regions during tapping.
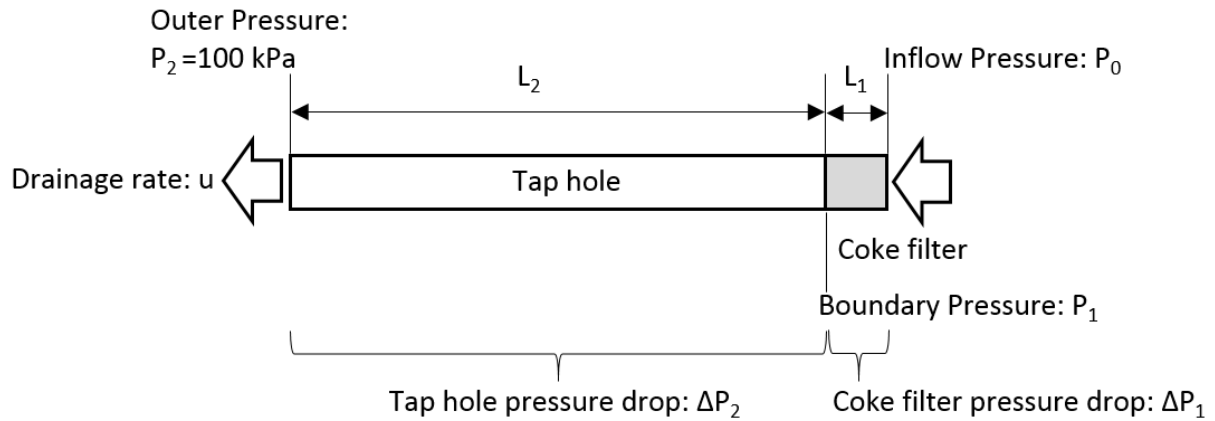
Figure 37 The iron blast furnace tapping flow model domain by Iida *et al.* (2008).

The pressure decreases from P_0 at the inlet to the coke filter, by ΔP_1 to P_1 at the interface between the coke filter and the taphole. The pressure further decreases from P_1 by the pressure drop across the taphole, ΔP_2, to the taphole outlet pressure, P_2. The pressure drops over the two regions are given by:

$$\Delta P_1 = P_0 - P_1 \qquad\qquad [32]$$

$$\Delta P_2 = P_1 - P_2 \qquad\qquad [33]$$

The flow rate through the taphole is obtained by separately solving the equations that describe the pressure drops across the coke filter and taphole. The pressure drop across the coke filter, ΔP_1, is modelled with the Kozeny-Carman equation (Equation [34]) as a function of the fluid flow rate and coke properties, while the pressure drop over the taphole, ΔP_2, is modelled with the Darcy Weisbach equation (Equation [35]) (Iida *et al.* 2008):

$$\Delta P_1 = \frac{180u \cdot \mu \cdot L_1}{D^2} \cdot \frac{(1 - \varepsilon)^2}{\varepsilon^3} \qquad\qquad [34]$$

61

$$\Delta P_2 = f \, \frac{L_2}{d} \cdot \frac{\rho \cdot u^2}{2} \qquad\qquad\qquad [35]$$

where

ΔP_1 : coke filter pressure drop (Pa),

u : fluid flow rate (m.s^{-1}),

μ : fluid viscosity (Pa.s),

L_1 : coke filter thickness (m),

D : coke particle diameter (m),

ε : coke filter void fraction,

ΔP_2 : taphole pressure drop (Pa),

f : taphole tube friction factor,

L_2 : taphole length (m),

d : taphole diameter (m), and

ρ : fluid density (kg.m^{-3}).

The taphole friction factor, f, is estimated by the Nikuradse equation (Iida *et al.* 2008), which contains the Reynolds number, Re, and is calculated as follows:

$$f = 0.0032 + \frac{0.221}{Re^{0.237}} \qquad\qquad\qquad [36]$$

$$Re = \frac{\rho u L_2}{\mu} \qquad\qquad\qquad [37]$$

where

Re : Reynolds number,

f : taphole tube friction factor,

L_2 : taphole length (m),

μ : fluid viscosity (Pa.s), and

ρ : fluid density (kg.m^{-3}).

The model by Iida *et al.* (2008) also includes the effect of coke consumption to form a low-permeability zone, as well as taphole enlargement rate to estimate transient flow behaviour. These effects are operation-specific for iron production in a blast furnace, and were therefore deemed not relevant for the purpose of this study on HCFeMn and SiMn production in SAFs.

5.2   Improved model

The blast furnace tapping flow modelling work reported by Iida *et al.* (2008) has been critically evaluated in this work, and certain errors were identified and improvements made to the model. The changes, which are discussed in more detail below, pertain essentially to the following:

- Slag and metal fluid properties, and that of the mixture.
- The path of fluid flow through the coke bed.
- The calculation of the Reynolds number and friction factor for fluid flow through the taphole.

5.2.1   Slag-metal mixture properties

The mixed fluid density and viscosity are in most cases estimated simply as the mean of the values for slag and metal respectively (Iida *et al.* 2008), despite the fact that the relative amounts of these fluids vary during tapping and that their properties can also differ significantly. In some CFD studies the two fluids are considered to be immiscible, and the fluid properties are specified individually; fluid flow of the mixture is then solved by the volume of fluid (VOF) method (Kadkhodabeigi *et al.* 2010, Leu 2010, Nishioka *et al.* 2005, Shao 2013).

Here, an attempt was made to estimate both the viscosity and density of the slag-metal mixed fluid more accurately, considering the volume fraction of each.

Mixed fluid viscosity:

As an improvement to calculating the mean, and to take into account the varying volume fractions of slag and metal in the mixed fluid being tapped, the viscosity may also be calculated as a weighted average according to the rule of mixtures:

$$\mu_{mixture} = (1 - \varphi)\mu_{slag} + \varphi\,\mu_{metal} \qquad\qquad [38]$$

where

$\mu_{mixture}$: viscosity of mixture (slag, metal) (Pa.s),

μ_{slag} : viscosity of slag (Pa.s),

μ_{metal} : viscosity of metal (Pa.s), and

φ : volume fraction metal.

In addition, the effective viscosity of the slag-metal mixture with varying volume fractions was modelled based on work by Pal (2001). This model was derived by correlating the viscosity of a concentrated emulsion with the viscosities of the continuous and dispersed phases and the volume fraction of the dispersed phase. This relationship estimates that viscosity will increase with the volume fraction of the dispersed phase. The model is based upon the assumption that the two fluids would be sufficiently

63

finely dispersed in one another. However, this is difficult to verify for the slag-metal system to which this model is applied.

This effective viscosity is modelled with the following equations (Pal 2001):

$$\mu_r \left[\frac{2\mu_r + 5K}{2 + 5K}\right]^{3/2} = \left(1 - \frac{\varphi}{\varphi_m}\right)^{-2.5\varphi_m} \tag{39}$$

$$\mu_{mixture} = \mu_r \times \mu_{continuous} \tag{40}$$

where

K : viscosity of the dispersed phase divided by the viscosity of the continuous phase ($\mu_{dispersed}/\mu_{continuous}$),

μ_r : relative viscosity (Pa.s),

$\mu_{mixture}$: viscosity of mixture (slag-metal) (Pa.s),

$\mu_{continuous}$: viscosity of continuous phase (Pa.s),

φ : volume fraction of the dispersed phase,

φ_m : model fitting parameter with a value of 0.637 used, and

$\mu_{dispersed}$: viscosity of dispersed phase (Pa.s).

The influence of the selection of dispersed and continuous phases is illustrated in Figure 38, calculated using a slag viscosity of 0.435 Pa.s and a metal viscosity of 0.006 Pa.s (Iida *et al.* 2008). The diagram shows the estimated mixed fluid viscosity as a function of the volume fraction of slag, selecting either slag (curve 1) or metal (curve 2) as the dispersed phase. In either case the volume fraction of the dispersed phase, φ, is constrained to 0.637 (the value of the model fitting parameter, φ_m,) due to the formulation of Equation [39]. Therefore for slag fractions between 0.363 and 0.637 it is possible to select either slag or metal as the dispersed phase. It cannot, however, be concluded from this work which fluid should be selected as the dispersed phase, but merely that the mixed fluid viscosity is estimated to be between the dashed lines in Figure 38. Below slag fractions of around 0.5 the estimated viscosities increase significantly. This is considered not to be realistic – for example, a mixture with 40% metal is not realistically expected to have a viscosity so high that almost no flow would occur.

Considering the viscosity ratios of the emulsion systems used by Pal (2001), the derived model would in most cases also be expected to be valid only up to dispersed phase fractions, φ, of around 0.5. At this point a large discontinuity exists in the estimated viscosities, as can be seen from the difference between the curves at a slag fraction of 0.5 (Figure 38). For the purpose of this study, only slag

fractions above 0.5 are considered, with the slag as the continuous phase containing dispersed metal at fractions up to 0.5.
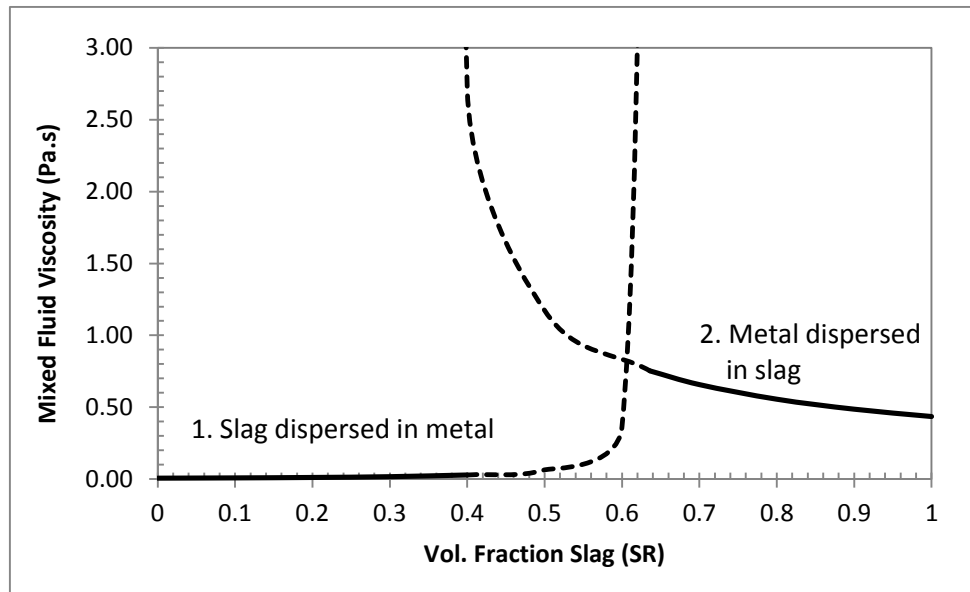
Figure 38 Estimated mixed fluid viscosity as a function of the volumetric slag fraction, alternating selected dispersed and continuous phases.

Mixed fluid density:

The average density of the slag-metal mixture is calculated by Equation [41], using the density and the volume fraction of each individual fluid. This would yield the same result as the mean density when the volume fractions of slag and metal are both 0.5:

$$\rho_{mixture} = (1 - \varphi)\rho_{slag} + \varphi\rho_{metal} \qquad [41]$$

where

$\rho_{mixture}$: density of mixture (slag, metal) (kg.m^{-3}),

ρ_{slag} : density of slag (kg.m^{-3}),

ρ_{metal} : density of metal (kg.m^{-3}), and

φ : volume fraction metal.

5.2.2 Spherical-radial fluid flow through a coke bed

The model domain is illustrated in Figure 39, showing the adapted configuration for flow through the coke bed as compared to that used by Iida *et al.* (2008) in Figure 37. Here the coke bed is considered to be a spherical volume around the taphole entry region where fluid flows from all directions into the taphole along the radius of the sphere. The derivation of the model based on this configuration is discussed below, and it is shown that the resulting pressure drop equation becomes independent of the distance that the fluid travels through the coke bed, eliminating the need to estimate this unknown parameter.

65
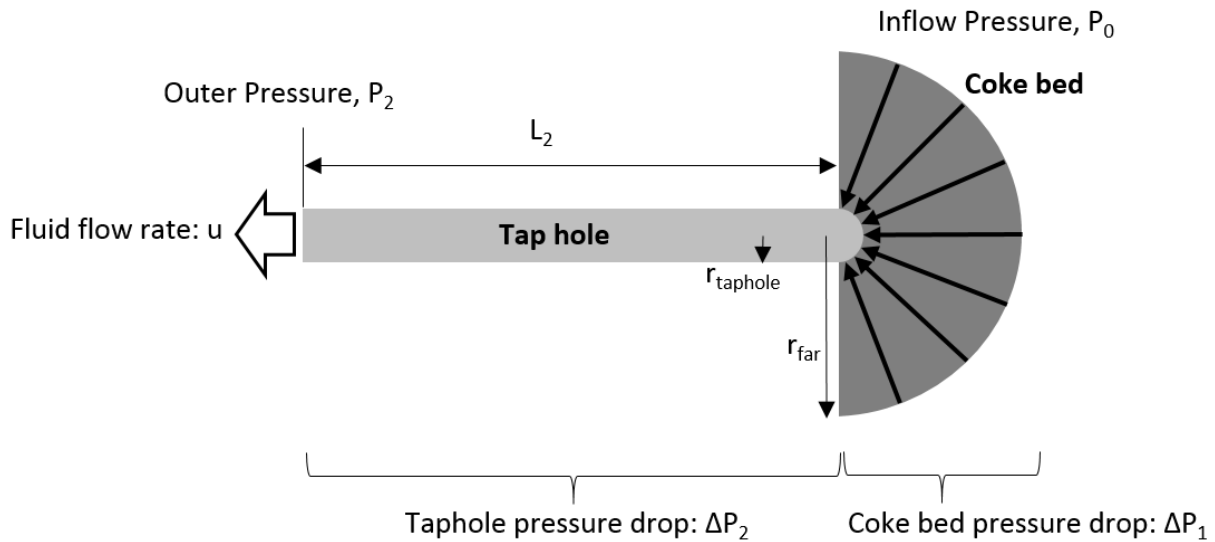
Figure 39 The improved model domain, with fluid flow through the taphole and spherical-radial flow through the coke bed.

To model the pressure drop across the coke bed, flow is assumed to be symmetrical around the entrance into the taphole. The Kozeny-Carman equation (as used by Iida *et al.* (2008) to model the pressure drop through the coke bed) is adapted so that the distance is the spherical radius (Figure 39). The pressure drop across the coke bed, ΔP_1, is then found by integrating this adapted pressure drop equation from the taphole radius to some point remote from the taphole:

$$\Delta P_1 = \int_{r_{taphole}}^{r_{far}} \frac{180u\mu}{D^2} \cdot \frac{(1-\varepsilon)^2}{\varepsilon^3} \cdot dr \qquad [42]$$

where

ΔP_1: coke bed pressure drop (Pa),

u : fluid flow rate (m.s^{-1}),

μ : fluid viscosity (Pa.s),

D : coke particle diameter (m),

ε : coke bed void fraction,

r : spherical radius, distance from taphole entrance (m),

$r_{taphole}$: taphole radius (m), and

r_{far} : far radius of sphere (m).

In the above equation the fluid flow velocity, u, is equal to the total fluid volumetric flow rate, V, divided by half the area of a sphere:

$$u = \frac{V}{2\pi r^2} \qquad [43]$$

66

where

u: fluid flow rate (m.s^{-1}),

V: fluid flow volumetric rate (m^3.s^{-1}), and

r : spherical radius, distance from taphole entrance (m).

The pressure drop across the coke bed (Equation [42]) then becomes the following if u is replaced with Equation [43]:

$$\Delta P_1 = \int_{r_{taphole}}^{r_{far}} \frac{90\,V\,\mu}{\pi\,r^2\,D^2} \cdot \frac{(1-\varepsilon)^2}{\varepsilon^3} \cdot dr \qquad [44]$$

The pressure drop across the coke bed is then given by the following relationship, obtained by integrating the modified Kozeny-Carman equation from $r_{taphole}$ to r_{far}:

$$\Delta P_1 = \frac{90V\mu}{\pi\,D^2} \cdot \frac{(1-\varepsilon)^2}{\varepsilon^3} \cdot \left(\frac{1}{r_{taphole}} - \frac{1}{r_{far}} \right) \qquad [45]$$

The length of coke bed through which fluid flows is expected to be significantly larger than the radius of the taphole, i.e. $r_{far} \gg r_{taphole}$. Figure 40 illustrates this effect, whereby the term $\left(\frac{1}{r_{taphole}} - \frac{1}{r_{far}} \right)$ quickly increases towards the value of only $\frac{1}{r_{taphole}}$ when the ratio of $r_{far}/r_{taphole}$ increases.

Equation [45] can then be reduced to Equation [46], in which the pressure drop is independent of the distance the fluid travels through the coke bed:

$$\Delta P_1 = \frac{90V\mu}{\pi\,D^2} \cdot \frac{(1-\varepsilon)^2}{\varepsilon^3} \cdot \frac{1}{r_{taphole}} \qquad [46]$$

67
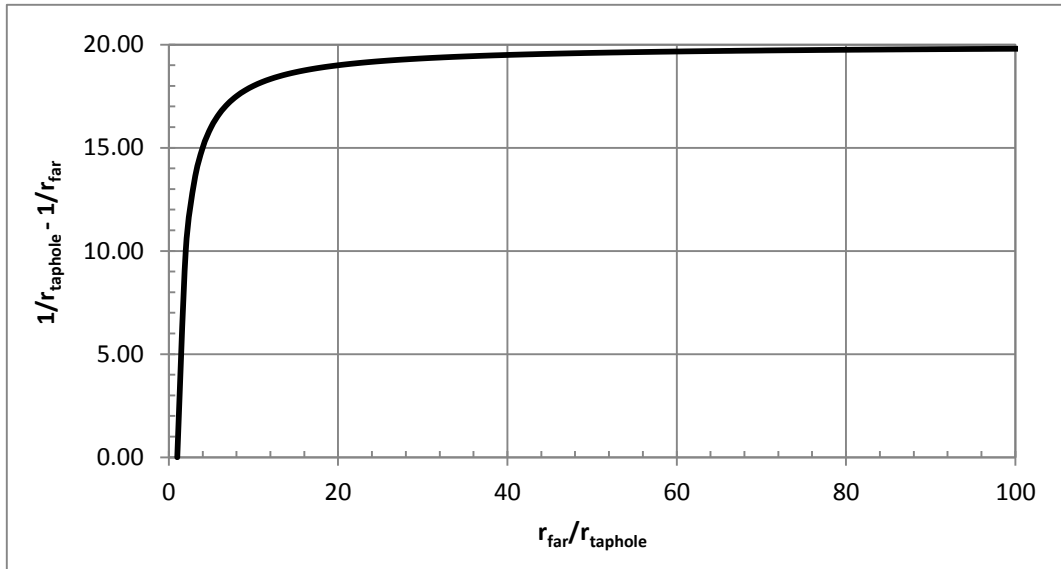
Figure 40 Illustration of the term (1/$r_{taphole}$ – 1/r_{far}) as a function of the ratio of r_{far}/$r_{taphole}$ (Equation [45]).

5.2.3 Taphole fluid flow

Starting with the taphole pressure drop model used by Iida *et al.* (2008) as a basis, some aspects are corrected and improved on.

Flow regime:

The flow profile is related to the fluid properties and the average velocity by calculating the Reynolds number, given by the Equation [47], considering the taphole to be a circular duct (Lienhard and Lienhard 2006):

$$Re_D = \frac{\rho D u_{avg}}{\mu} \qquad [47]$$

where ρ is the fluid density (kg.m^{-3}), D is the pipe diameter (m), u_{avg} the average fluid velocity (m.s^{-1}), and μ the fluid dynamic viscosity (kg.m^{-1}.s^{-1}).

Equation [47] for the Reynolds number is similar to that used by Iida *et al.* (2008), but is corrected here to use the taphole diameter, D, instead of the taphole length incorrectly used by Iida *et al.* (2008).

This Reynolds number can be used to estimate the velocity at which transition from laminar to turbulent flow would occur, considering that developed laminar flow is certain up to a Reynolds number of around 2100, but could extend to 10 000 if care is taken with the flow configuration (Lienhard and Lienhard 2006).

68

Fully developed laminar flow entry length:

Flow develops towards fully developed laminar flow along the length of the pipe. From the point at which laminar flow is fully developed, the velocity vectors would not change with respect to the length of the pipe, and the flow stream lines would be parallel.

The distance from the entry to the pipe up to where laminar flow is fully developed is termed the entry length, and can be estimated as a function of the Reynolds number and the pipe diameter (Lienhard and Lienhard 2006):

$$\frac{x_e}{D} = 0.03 Re_D \qquad\qquad [48]$$

where x_e is the length required for laminar flow to fully develop (m), D the pipe diameter (m), and Re_D the Reynolds number for flow through a pipe (Equation [47]).

Darcy-Weisbach tubular flow pressure drop equation:

The Darcy-Weisbach equation (Lienhard and Lienhard 2006) is used to model flow through a cylindrical tube, which is similar to the model by Iida *et al.* (2008) (Equation [35]). The fluid flowing through the coke bed enters the taphole at the one end and exits at the other end, with the pressure drop, ΔP_2, estimated as:

$$\Delta P_2 = f\,\frac{L_2}{d} \cdot \frac{\rho \cdot u^2}{2} \qquad\qquad [49]$$

where

ΔP_2: taphole pressure drop (Pa),

u : fluid flow rate (m.s^{-1}),

f : taphole tube friction factor,

L_2 : taphole length (m),

d : taphole diameter (m), and

ρ : fluid density (kg.m^{-3}).

Darcy-Weisbach friction factor:

The friction factor in Equation [49] can be calculated specifically for either fully developed laminar flow or for turbulent flow by using experimentally determined correlations. For the taphole considered with a low length-to-diameter ratio, flow is expected not to develop into fully laminar flow. In such a case,

69

where flow is in the transitional entry region of a tube, the Darcy-Weisbach friction factor can be up to four times larger than that of fully developed laminar flow (Ghajar and Madon 1992).

The apparent friction factor for developing laminar flow (Re < 2100), f_{app}, is calculated using the correlation by Ghajar and Madon (1992):

$$f_{app} = \frac{1}{Re}\left(\frac{3.44}{\zeta^{1/2}} + \frac{0.31/\zeta + 16 - 3.44/\zeta^{1/2}}{1 + 0.00021/\zeta^2}\right) \qquad [50]$$

$$\zeta = \frac{L_2}{d\,Re} \qquad [51]$$

where

$\quad f_{app}$: apparent Darcy-Weisbach friction factor for developing laminar flow,

$\quad Re$: Reynolds number,

$\quad L_2$: taphole length (m), and

$\quad d$: taphole diameter (m).

The apparent friction factor for turbulent flow (Re > 2100), $f_{turbulent}$, is calculated using the empirical Haaland equation (Bird *et al.* 2007):

$$f_{turbulent} = \frac{4}{\left(3.6\log\left(\frac{Re}{6.9}\right)\right)^2} \qquad [52]$$

70

6 Tapping flow model results and discussion

The tapping flow models formulated in the previous sections have been applied in order to analyse the flow of slag and metal mixtures through a taphole. The following outlines the model applications:

1. The blast furnace tapping flow model by Iida *et al.* (2008) was applied, as described in Section 5.1, in order to validate the application methodology. The length of the coke bed flow path was varied to produce results comparable with those presented by Iida *et al.* (2008). The relevant model input parameter values were then applied in the improved tapping flow model, as described in Section 5.2, in order to establish the differences in results due to the model modifications. Here the effect of varying slag-metal ratio was evaluated.

2. The improved tapping flow model was applied, using as model parameters the physicochemical properties of typical SiMn and HCFeMn slags and alloys and other model parameter values representative of a typical SAF producing these alloys. A baseline scenario was established, and flow then evaluated at various slag-metal ratios, taphole lengths and diameters, and coke bed particle void fractions and diameters. For comparison, viscosity is estimated using the rule of mixtures approach (Equation [38]) and the model by Pal (2001) (Equations [39] and [40]).

6.1 Iron blast furnace tapping flow

6.1.1 Model by Iida *et al.* (2008)

The blast furnace tapping flow model by Iida *et al.* (2008) has been applied as was described in Section 5.1 in order to validate the model implementation. This application also allowed for the estimation of other result parameters not reported by Iida *et al.* (2008), e.g. coke bed and taphole pressure drops, Reynolds number, friction factor, etc. Table 11 summarises the value of each model parameter used in this application, including material properties, boundary conditions, and dimensional parameters. The slag-metal mixed fluid density and viscosity were calculated as the means of the values for the individual fluids, in this case yielding the same values as calculating volume-weighted averages would, since the slag ratio, SR, was 0.5.

Table 11 Blast furnace tapping flow model parameter values as per Iida *et al.* (2008).

Category	Parameter	Symbol	Units	Value
Material property	Coke particle diameter	D	m	0.04
Material property	Coke filter void fraction	ε		0.32
Material property	Slag density	ρ_{slag}	kg.m^{-3}	2800
Material property	Metal density	ρ_{metal}	kg.m^{-3}	6700
Material property	Slag viscosity	μ_{slag}	Pa.s	0.435
Material property	Metal viscosity	μ_{metal}	Pa.s	0.006
Material property	Slag ratio (vol. fraction slag)	SR	Vol. fraction	0.5
Boundary condition	Inlet pressure	P_0	kPa	400
Boundary condition	Outlet pressure	P_2	kPa	100

Category	Parameter	Symbol	Units	Value
Dimension	Coke filter thickness	L_1	m	0.08 (0.01-0.15)
Dimension	Taphole length	L_2	m	3.5
Dimension	Taphole diameter	d	m	0.06

The estimated results from varying the coke filter length parameter, L_1, between 0.01 and 0.15 m are summarised in Table 12, with the baseline value of 0.08 m. The estimated volumetric flow rates as a function of coke filter length (illustrated in Figure 41) match the initial drainage rates reported by Iida *et al.* (2008). Since similar model input parameter values are used here, it is concluded that the model has been correctly applied.

The results in Table 12 illustrate the sensitivity of the estimated flow rate to the coke filter length. Since it is not possible to measure the coke filter length accurately, a value for use in the model can be determined as the value for which the estimated flow rate agrees with an actual measurement. Iida *et al.* (2008) estimated a coke filter length of 0.08 m using this approach; hence this was selected as the baseline value. For coke filter lengths of around 0.08 m, the model results indicate the pressure drop through the coke filter to be dominant.

The Reynolds number has been incorrectly calculated in the model by Iida *et al.* (2008), using the taphole length rather than the diameter. Table 12 lists both the incorrect Reynolds numbers, Re, and the corrected Reynolds numbers, Re_{corr}, estimated for these scenarios. Considering only the corrected values, Re_{corr}, and assuming all other relationships in the model to be valid, the fluid flow can be classified as turbulent (Re >2100).

Table 12 Blast furnace tapping flow modelling results using the model and parameter values as per Iida *et al.* (2008), varying coke filter length.

Parameter	Symbol	Units	Coke filter length, L_1 (m):				
			0.01	0.05	0.08 (baseline)	0.1	0.15
Mixed fluid density	ρ_{avg}	kg.m-3	4750	4750	4750	4750	4750
Mixed fluid viscosity	μ_{avg}	Pa.s	0.2205	0.2205	0.2205	0.2205	0.2205
Reynolds nr.	Re		948 712	684 635	551 581	484 419	366 019
Friction factor	f		0.012	0.012	0.013	0.013	0.014
Coke bed pressure drop	ΔP_1	Pa	44 046	158 930	204 869	224 904	254 900
Taphole pressure drop	ΔP_2	Pa	255 954	141 070	95 131	75 096	45 100
Total pressure drop	ΔP_{tot}	Pa	300 000	300 000	300 000	300 000	300 000
Fluid flow velocity	u	m.s-1	12.583	9.080	7.316	6.425	4.855
Fluid volumetric rate	V	m3.s-1	0.0356	0.0257	0.0207	0.0182	0.0137
Fluid mass rate	M	kg.s-1	169.0	122.0	98.3	86.3	65.2
Corr. Reynolds nr.	Re_{corr}		16 264	11 737	9456	8304	6275
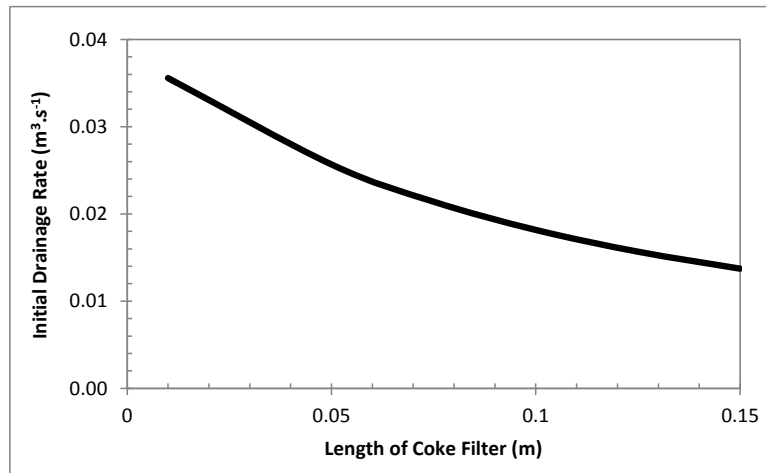
Figure 41 Initial drainage rates estimated for varying coke filter length – Iida *et al.* (2008).

6.1.2   Improved model

The blast furnace tapping flow model reported by Iida *et al.* (2008) was modified as described in Section 5.2. Some modelling errors were corrected, fluid flow models updated, and most importantly, the flow model through the coke bed was changed to be independent of the coke bed length. This section reports on the results from the application of this improved model for iron blast furnace tapping, highlighting differences from the results presented above.

Applying model parameters from Iida *et al.* (2008):

To establish the effect of the change to the model, the improved model was applied for the iron blast furnace using the same model parameter values used by Iida *et al.* (2008), summarised in Table 11. Although the density and viscosity are the same as those used previously for slag and metal respectively (Table 11), the improvements included the use of a different model to estimate the mixed fluid properties (Section 5.2.1). Also, the variation of the coke bed fluid path length is not relevant here, since the improved model is independent of this parameter (Section 5.2.2).

Table 13 Blast furnace tapping flow modelling results using the improved model with parameter values from Iida *et al.* (2008).

Parameter	Symbol	Units	Value
Mixed fluid density	ρ_{avg}	kg.m^{-3}	4750
Mixed fluid viscosity	μ_{avg}	Pa.s	1.17
Reynolds nr.	Re		1746
Friction factor	f		0.014
Coke bed pressure drop	ΔP_1	Pa	200 643
Taphole pressure drop	ΔP_2	Pa	99 357
Total pressure drop	ΔP_{tot}	Pa	300 000
Fluid flow velocity	u	m.s^{-1}	7.185
Fluid volumetric rate	V	m^3.s^{-1}	0.0203
Fluid mass rate	M	kg.s^{-1}	96.5
Laminar flow entry length	x_e	m	3.144

73

The results obtained from this improved model are presented in Table 13, and compare with results from the previous section (Table 12) as follows.

The mixed <u>fluid density</u> obtained here was unchanged at 4750 kg.m^{-3}. This was due to the slag fraction being 0.5, yielding the same result for density calculated as the mean of the two fluids (Iida *et al.* 2008) or as the volume weighted average (Equation [41]). The mixed <u>fluid viscosity</u> of 1.17 Pa.s is significantly higher than the slag-metal mean value of 0.22 Pa.s obtained by Iida *et al.* (2008). This illustrates that compared with the model from Pal (2001) (Equations [39] and [40]), the effective viscosity of the continuous phase (slag) is significantly increased by the dispersed phase (metal) in the case of emulsions.

The <u>Reynolds number</u> was found to be 1746 (reflecting the higher viscosity), which indicates laminar flow through the taphole, and is significantly different to the higher values estimated previously (Table 12), which indicated turbulent flow. The taphole length required to obtain this fully developed laminar flow (entry length) was calculated as 3.144 m, indicating the flow to be developing towards laminar flow over most of the length of the 3.5 m long taphole. The friction factor equation for developing laminar flow yields a value of 0.014, within the range of 0.012 to 0.014 obtained earlier in the model by Iida *et al.* (2008).

The mixed fluid flow <u>velocity</u> in the taphole was estimated as 7.185 m.s^{-1}, which is comparable to the value of 7.316 m.s^{-1} calculated by Iida *et al.* (2008) for the baseline coke bed fluid path length of 0.08 m. With this model the <u>pressure drop</u> through the coke bed was also found to be dominant, accounting for approximately two-thirds of the total pressure drop.

Effect of varying the slag ratio:

With more metal typically being tapped at the start of tapping, the fraction of slag is expected to increase throughout a tap. The influence of this change in slag and metal fractions on tapping rate was investigated. The results are illustrated in Figure 42, and summarised in Table 14. The improved model was again applied for the iron blast furnace by using the same model parameter values used by Iida *et al.* (2008), summarised in Table 11. The model by Pal (2001) was used to estimate the effective mixture viscosity, selecting slag as the continuous phase, containing dispersed metal with fractions up to 0.5 (slag fractions 0.5 to 1).

In general, Figure 42 illustrates that flow rates were estimated to increase with the slag fraction being tapped, as the mixed fluid viscosity was estimated to decrease with less of the dispersed phase (metal) present (Pal 2001) (illustrated in Figure 38). From a slag fraction of 0.5 up to around 0.53, the Reynolds numbers were estimated to increase up to 2100, and higher flow rates were obtained due to lower

74

laminar flow friction factors. From slag fractions of around 0.68 to 1, Reynolds numbers were estimated to be greater than 2100, lower flow rates being obtained due to higher turbulent flow friction factors.

It could be concluded from the results that at these low slag fractions, the viscosities estimated with the mixed fluid viscosity model from Pal (2001) are further removed from what is actually expected as the volume fraction of slag decreases. The model suggests the mixed fluid viscosity continues to increase and flow rate continues to decrease as the metal fraction increases, which does not correspond to observations in practice. This indicates that the assumptions associated with the application of the mixed fluid viscosity by Pal (2001) are less likely to be valid for this set of model input parameter values at lower slag fractions. The model by Pal (2001) was nonetheless also evaluated against the rule of mixtures later for HCFeMn and SiMn SAF tapping model application.

Figure 42 Total volumetric flow rates estimated with the improved model for an iron blast furnace as a function of volume fraction slag (effective viscosity with model by Pal (2001)).

For slag fractions between 0.527 and 0.683, discontinuities in the estimated flow rates resulted from the differences in the friction factors for laminar and turbulent flow. Table 15 summarises the results calculated for a slag fraction of 0.6, showing that should the lower laminar friction factor be used at a slag fraction of 0.6, a high flow rate is estimated and subsequently a Reynolds number larger than 2100 is obtained. Should the higher turbulent friction factor be used, as indicated by the Reynolds number larger than 2100, a lower flow rate is estimated and the Reynolds number is then again significantly less than 2100, suggesting that the laminar friction factor should be used. The dashed lines in Figure 42 illustrate the flow rates that would be estimated in this region should the laminar friction factor be used even though the Reynolds number is estimated at larger than 2100 (line 1), or if the turbulent friction factor is used for Reynolds numbers smaller than 2100.

At the low slag fractions with low Reynolds numbers estimated, the <u>pressure drop</u> was dominant over the coke bed, again accounting for around two-thirds of the total pressure drop. In the turbulent flow

75

region estimated for higher slag fractions, the pressure drop became dominant over the taphole, accounting for around two-thirds of the total pressure drop.

Table 14 Blast furnace tapping flow modelling results using the improved model with parameter values from Iida *et al.* (2008) - varying slag ratio (effective viscosity with model by Pal (2001)).

Parameter	Symbol	Units	Slag ratio, SR:						
			0.5	0.5263	0.683	0.7	0.8	0.9	1
Mixed fluid density	ρ_{avg}	kg.m^{-3}	4750	4647	4036	3970	3580	3190	2800
Mixed fluid viscosity	μ_{avg}	Pa.s	1.17	1.05	0.68	0.66	0.56	0.49	0.44
Reynolds nr.	Re		1746	2098	2101	2176	2552	2828	3007
Friction factor	f		0.014	0.012	0.050	0.049	0.047	0.045	0.044
Coke bed pressure drop	ΔP_1	Pa	200 643	196 619	95 352	93 885	87 264	83 098	80 650
Taphole pressure drop	ΔP_2	Pa	99 357	103 381	204 648	206 115	212 736	216 902	219 350
Total pressure drop	ΔP_{tot}	Pa	300 000	300 000	300 000	300 000	300 000	300 000	300 000
Fluid flow velocity	u	m.s^{-1}	7.185	7.882	5.894	6.001	6.598	7.180	7.786
Fluid volumetric rate	V	m^3.s^{-1}	0.020	0.022	0.017	0.017	0.019	0.020	0.022
Fluid mass rate	M	kg.s^{-1}	96.5	103.6	67.3	67.4	66.8	64.8	61.6
Laminar flow entry length	x_e	m	3.144	3.776	3.782	3.916	4.593	5.090	5.412

Table 15 Blast furnace tapping flow modelling results using the improved model with parameter values from Iida *et al.* (2008) – alternating the flow regime assumed in calculation of the friction factors (effective viscosity with model by Pal (2001)).

Parameter	Symbol	Units	Slag ratio, SR:	
			0.6	0.6
Flow regime Used for friction factor			Laminar	Turbulent
Mixed fluid density	ρ_{avg}	kg.m^{-3}	4360	4360
Mixed fluid viscosity	μ_{avg}	Pa.s	0.82	0.82
Reynolds nr.	Re		3028	1692
Friction factor	f		0.010	0.054
Coke bed pressure drop	ΔP_1	Pa	187 356	104 651
Taphole pressure drop	ΔP_2	Pa	112 644	195 349
Total pressure drop	ΔP_{tot}	Pa	300 000	300 000
Fluid flow velocity	u	m.s^{-1}	9.544	5.331
Fluid volumetric rate	V	m^3.s^{-1}	0.027	0.015
Fluid mass rate	M	kg.s^{-1}	117.6	65.7
Laminar flow entry length	x_e	m	5.451	3.045

Results were also calculated using the rule of mixtures approach to estimate the effective slag-metal viscosity. It was possible to estimate results for slag fractions from 0 to 1. The volumetric flow rates are illustrated in Figure 43 and the results summarised Table 16. Over the full range of slag fractions, turbulent flow was obtained as a result of the decreased mixture viscosity and higher flow rates for lower slag fractions, with the Reynolds number decreasing for increasing slag fractions. As with the above results, in the turbulent flow region the pressure drop was dominant over the taphole, but decreased in relation to that over the coke bed with increasing slag fractions.

A volumetric flow rate of 0.032 m^3.s^{-1} was estimated when tapping only metal (SR = 0), decreasing to 0.022 m^3.s^{-1} at a slag fraction of 0.5. At slag fractions of 0.5 to 1 the flow rate was estimated to be

76

almost constant at 0.022 m³.s⁻¹ as a result of the increasing taphole friction factor with decreasing Reynolds numbers and increasing mixture viscosities. In this range of slag fractions (SR = 0.5 to 1) the tapping rates estimated were therefore again comparable with that obtained by Iida *et al.* (2008).
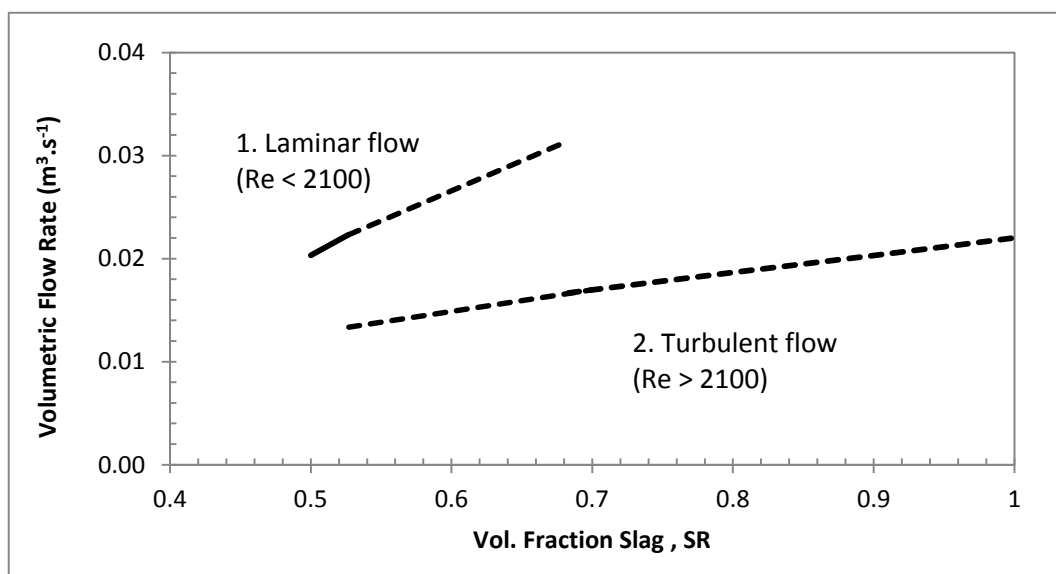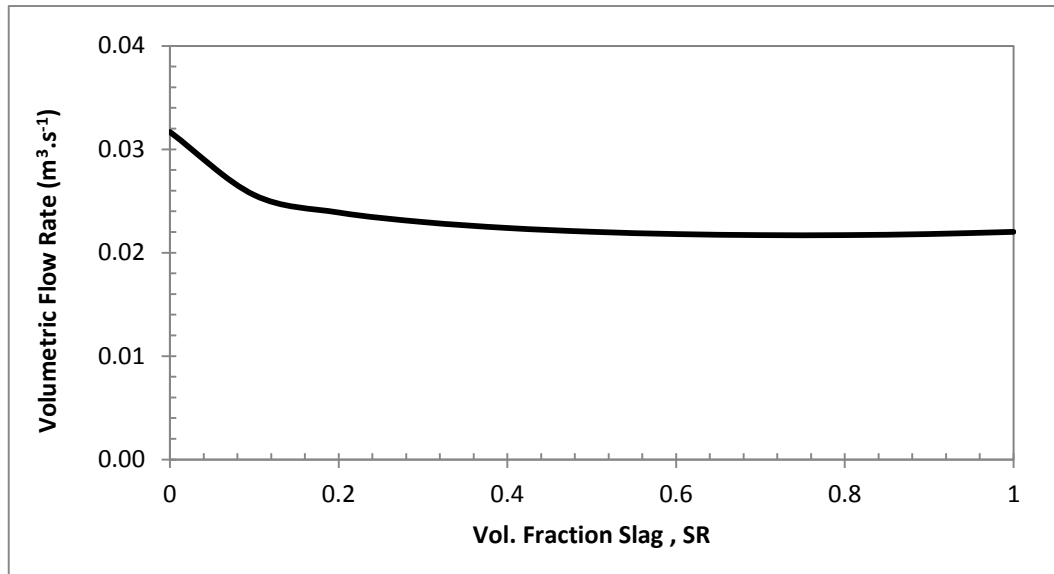

Figure 43 Total volumetric flow rates estimated with the improved model for an iron blast furnace at various volume fractions of slag (effective viscosity with rule of mixtures).

Table 16 Blast furnace tapping flow modelling results using the improved model with parameter values from Iida *et al.* (2008) - varying slag ratio (effective viscosity with rule of mixtures).

Parameter	Symbol	Units	Slag ratio, SR:						
			0	0.3	0.5	0.7	0.8	0.9	1
Mixed fluid density	ρ_{avg}	kg.m⁻³	6700	5530	4750	3970	3580	3190	2800
Mixed fluid viscosity	μ_{avg}	Pa.s	0.01	0.13	0.22	0.31	0.35	0.39	0.44
Reynolds nr.	Re		750 583	20 007	10 067	5968	4721	3764	3007
Friction factor	f		0.012	0.026	0.031	0.036	0.038	0.041	0.044
Coke bed pressure drop	ΔP_1	Pa	1601	26 052	40 896	55 977	63 823	72 004	80 650
Taphole pressure drop	ΔP_2	Pa	298 399	273 948	259 104	244 023	236 177	227 996	219 350
Total pressure drop	ΔP_{tot}	Pa	300 000	300 000	300 000	300 000	300 000	300 000	300000
Fluid flow velocity	u	m.s⁻¹	11.203	8.122	7.789	7.675	7.675	7.712	7.786
Fluid volumetric rate	V	m³.s⁻¹	0.032	0.023	0.022	0.022	0.022	0.022	0.022
Fluid mass rate	M	kg.s⁻¹	212.2	127.0	104.6	86.1	77.7	69.6	61.6
Laminar flow entry length	x_e	m	1351.049	36.012	18.121	10.743	8.498	6.776	5.412

6.2 SiMn and HCFeMn SAF tapping flow

The improved tapping flow model (Section. 5.2) was applied to evaluate tapping from SAFs producing SiMn and HCFeMn. For this exercise a different set of values were defined for the common model parameters for the taphole dimensions, slag and metal properties, coke bed properties, and boundary conditions.

Table 17 Summary of SAF tapping flow model parameter values.

Category	Parameter	Symbol	Units	Value	Notes
Material property	Coke particle diameter	D	m	0.05	Kadkhodabeigi (2011)
Material property	Coke filter void fraction	ε		0.3	Kadkhodabeigi (2011)

Category	Parameter	Symbol	Units	Value	Notes
Material property	Slag density	ρ_{slag}	kg.m^{-3}	2745 – 3327	Calculated, see Table 10
Material property	Metal density	ρ_{metal}	kg.m^{-3}	SiMn: 4449; HCFeMn: 5612	Calculated, see below
Material property	Slag viscosity	μ_{slag}	Pa.s	0.64 – 1.54	Calculated, see Table 10
Material property	Metal viscosity	μ_{metal}	Pa.s	0.005	Kadkhodabeigi (2011)
Boundary condition	Inlet pressure	P_0	Pa	115 000	Kadkhodabeigi (2011)
				127 133 – 129 663	Calculated, see Table 19
Boundary condition	Outlet pressure	P_2	Pa	100 000	As for Iida *et al.* (2008)
Geometry	Taphole length	L_2	m	0.6	Kadkhodabeigi (2011)
Geometry	Taphole diameter	d	m	0.1	Kadkhodabeigi (2011)
Geometry	Slag Height	h_{slag}	m	0.0; 0.5	Kadkhodabeigi (2011)
Geometry	Metal Height	h_{metal}	m	0.0	Kadkhodabeigi (2011)

The baseline set of model parameters values is summarised in Table 17:

1. *Coke bed particulate properties*: A coke bed particle diameter of 0.05 m and void fraction of 0.3 were used for the coarse coke bed by Kadkhodabeigi (2011) in the 2D CFD modelling of the FeMn tapping process.

2. *Slag properties*: Densities and viscosities of the three SiMn and four HCFeMn slags were used from Table 10.

3. *Metal properties*: A <u>viscosity</u> of 0.005 Pa.s was used by Kadkhodabeigi (2011) and applied here for both SiMn and HCFeMn alloys. SiMn and HCFeMn metal <u>densities</u> were calculated by combining the models of Crawley (1974), Jimbo and Cramb (1993), and Nasch and Steinemann (1995). Compositions used are summarised in Table 18, derived from the typical ranges provided by Olsen *et al.* (2007).The densities were calculated for SiMn and HCFeMn alloys as 4449 and 5612 kg.m^{-3} respectively.

Table 18 Typical compositions (wt.%) of HCFeMn and SiMn alloys derived from typical values in Olsen *et al.* (2007).

	Metal compositions (wt.%)	
Specie	HCFeMn	SiMn
Mn	78	67.5
Si	0.3	28.5
Fe	14	9
C	7.5	2.75

4. *Geometry*: A taphole length of 0.6 m and taphole diameter of 0.1 m were used. The initial slag height was set at 0.5 m, and metal height at 0 m, i.e. level with the taphole (Kadkhodabeigi 2011).

5. *Boundary conditions*: In 2D CFD modelling of the FeMn tapping process, a pressure of 15 000 Pa (gauge pressure) on top of the slag layer was specified by Kadkhodabeigi (2011) to account for the weight of the burden on the slag. The total boundary pressure used was the sum of this value, the atmospheric pressure of 100 000 Pa, and the hydrostatic pressure calculated for different slag heights (0 to 0.5 m) and density of each slag. The maximum total inlet boundary

pressures obtained for each slag composition considered at a slag height of 0.5 m above the taphole are summarised in Table 19. For the case where both the slag and metal heights were 0 m above the taphole, the boundary pressure was merely 115 000 Pa and did not vary with the slags considered.

Table 19 Slag and metal densities and total boundary pressures used in the SiMn and HCFeMn SAF tapping flow models for a slag height of 0.5 m above the taphole.

Parameter	Symbol	Units	SiMn process			HCFeMn process			
			SiMn A	SiMn B	SiMn C	HCFeMn A	HCFeMn B	HCFeMn C	HCFeMn D
Slag density	ρ_{slag}	kg.m^{-3}	2540	2531	2476	2992	2676	2852	2922
Total inlet pressure*	P_0	Pa	127448	127 403	127 133	129 663	128 111	128 973	129 318

* Calculated for a boundary pressure of 15 000 Pa (gauge pressure), atmospheric pressure of 100 000 Pa, and hydrostatic pressure for a slag height of 0.5 m slag.

6.2.1 Baseline

The improved tapping flow model was applied with the baseline model parameter values for the HCFeMn and SiMn processes summarised in Table 17, while changing the slag fraction (SR) between 0.5 and 1, and the slag height between 0 and 0.5 m. The total volumetric tap flow rates estimated are illustrated in Figure 44 and total mass rates in Figure 45, both shown as functions of viscosity for each of the typical slags considered, using the model by Pal (2001) for estimating the mixed fluid viscosity. Both these figures show typical flow rate ranges, roughly derived from data by Olsen *et al.* (2007) (Table 5). The resulting values are listed in Table 20 to Table 23 for the considered combinations of tapped slag fractions of 0.5 and 1, and the slag height at 0 and 0.5 m above the taphole.
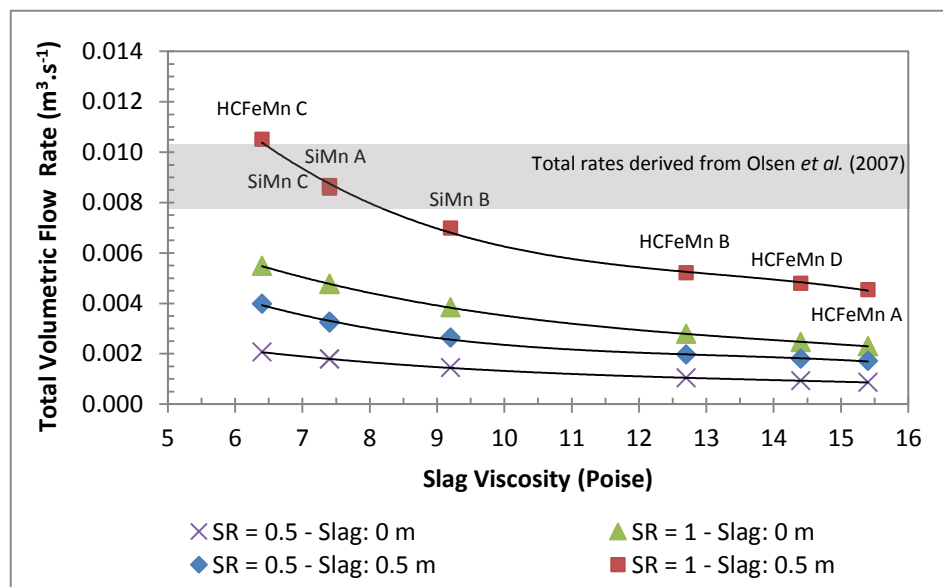
Figure 44 Total volumetric flow rate as a function of viscosity for typical SiMn and HCFeMn slags, for slag heights of 0 and 0.5 m, and slag fractions (SR) of 0.5 and 1 (effective viscosity with model by Pal (2001)).
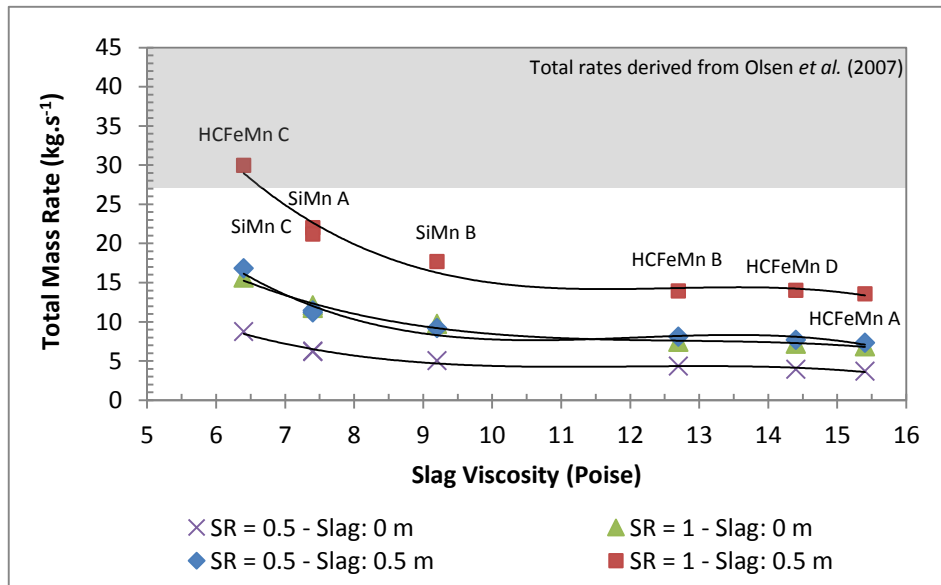
Figure 45 Total mass flow rate as a function of viscosity for typical SiMn and HCFeMn slags, for slag heights of 0 and 0.5 m, and slag fractions (SR) of 0.5 and 1 (effective viscosity with model by Pal (2001)).

The volumetric tapping rates estimated here (Figure 44) can be seen to be generally lower than those obtained earlier for the iron blast furnace (Figure 42) using the same model. As would be expected, the tapping rates also decreased with increasing slag viscosity and with decreasing slag height above the taphole (Figure 44, Figure 45).

When tapping only slag (SR = 1), mass rates were estimated between 14 and 30 kg.s^{-1} when the slag was at 0.5 m above to taphole (Table 21), and decreased significantly to between 4 and 9 kg.s^{-1} at the end of the tap when the slag was at 0 m above the taphole (Table 22). These estimated slag-only rates compare with the estimates of 13 to 18 kg.s^{-1} for typical operations provided earlier (Table 5), which were derived from data reported by Olsen *et al.* (2007), as well as with the estimated rates up to around 18 kg.s^{-1} obtained by Kadkhodabeigi (2011).

The total tapping rates of the mixed fluid tap streams with slag fractions of 0.5 were estimated to be significantly lower than the tapping rates of slag only (SR = 1), as illustrated in Figure 44 and Figure 45. The volumetric tapping rates of slag and metal were each half of these low total rates, and therefore significantly lower than the typical rates derived from Olsen *et al.* (2007) and Kadkhodabeigi (2011). Lower mixed fluid rates were estimated for these, since higher effective viscosities were estimated for the mixed fluids containing higher amounts of dispersed metal, similar to what was observed in the iron blast furnace model application. This deviation from actual results further indicates that the assumptions associated with the application of the mixed fluid viscosity by Pal (2001) are less likely to be valid for this system at lower slag fractions.

The pressure drop over the coke bed has been found to be dominant in the scenarios of varying slag fraction tapped and the slag height (shown in Table 20 to Table 23) investigated here, with the pressure

drops over the taphole being negligible. <u>Reynolds numbers</u> were estimated to be higher for the slags with lower viscosities, but remaining well below 2100, indicating laminar flow in the taphole. <u>Entry lengths</u> required for development into laminar flow were estimated to be shorter than the taphole length of 0.6 m, except for the scenarios in which the lowest mixed fluid viscosities were estimated due to a high slag fraction (SR = 1) and the high inlet pressure (slag height = 0.5 m), in which case the entry lengths ranged from 0.6 to 2 m.

Table 20 SiMn and HCFeMn SAF tapping flow model results using parameter values from Table 17, for a slag fraction (SR) of 0.5, slag height at 0.5 m above the taphole (effective viscosity with model by Pal (2001)).

Parameter	Symbol	Units	SiMn process			HCFeMn process			
			SiMn A	SiMn B	SiMn C	HCFeMn A	HCFeMn B	HCFeMn C	HCFeMn D
Slag density	ρ_{slag}	kg.m^{-3}	2540	2531	2476	2992	2676	2852	2922
Slag viscosity	μ_{slag}	Pa.s	0.74	0.92	0.74	1.54	1.27	0.64	1.44
Mixed fluid density	ρ_{avg}	kg.m^{-3}	3495	3490	3463	4302	4144	4232	4267
Mixed fluid viscosity	μ_{avg}	Pa.s	1.98	2.46	1.98	4.11	3.39	1.72	3.85
Reynolds nr.	Re		73	48	72	23	30	125	25
Friction factor	f		0.266	0.386	0.271	0.753	0.575	0.175	0.678
Coke bed pressure drop	ΔP_1	Pa	26 963	26 949	26 656	29 203	27 666	28 402	28 860
Taphole pressure drop	ΔP_2	Pa	484	454	477	460	445	571	458
Total pressure drop	ΔP_{tot}	Pa	27 448	27 403	27 133	29 663	28 111	28 973	29 318
Fluid flow velocity	u	m.s^{-1}	0.416	0.335	0.412	0.217	0.250	0.507	0.230
Fluid volumetric rate	V	m^3.s^{-1}	0.0033	0.0026	0.0032	0.0017	0.0020	0.0040	0.0018
Fluid mass rate	M	kg.s^{-1}	11.4	9.2	11.2	7.3	8.1	16.8	7.7
Laminar flow entry length	x_e	m	0.220	0.143	0.216	0.068	0.091	0.375	0.076

Table 21 SiMn and HCFeMn SAF tapping flow model results using parameter values from Table 17, for a slag fraction (SR) of 1, slag height at 0.5 m above the taphole (effective viscosity with model by Pal (2001)).

Parameter	Symbol	Units	SiMn process			HCFeMn process			
			SiMn A	SiMn B	SiMn C	HCFeMn A	HCFeMn B	HCFeMn C	HCFeMn D
Slag density	ρ_{slag}	kg.m^{-3}	2540	2531	2476	2992	2676	2852	2922
Slag viscosity	μ_{slag}	Pa.s	0.74	0.92	0.74	1.54	1.27	0.64	1.44
Mixed fluid density	ρ_{avg}	kg.m^{-3}	2540	2531	2476	2992	2676	2852	2922
Mixed fluid viscosity	μ_{avg}	Pa.s	0.74	0.92	0.74	1.54	1.27	0.64	1.44
Reynolds nr.	Re		379	245	365	112	140	596	124
Friction factor	f		0.084	0.110	0.086	0.190	0.161	0.064	0.176
Coke bed pressure drop	ΔP_1	Pa	26 668	26 741	26 374	29 093	27 541	27 987	28 741
Taphole pressure drop	ΔP_2	Pa	779	661	759	570	570	986	577
Total pressure drop	ΔP_{tot}	Pa	27 448	27 403	27 133	29 663	28 111	28 973	29 318
Fluid flow velocity	u	m.s^{-1}	1.103	0.890	1.091	0.578	0.664	1.339	0.611
Fluid volumetric rate	V	m^3.s^{-1}	0.0087	0.0070	0.0086	0.0045	0.0052	0.0105	0.0048
Fluid mass rate	M	kg.s^{-1}	22.0	17.7	21.2	13.6	14.0	30.0	14.0
Laminar flow entry length	x_e	m	1.136	0.734	1.095	0.337	0.420	1.789	0.372

Table 22 SiMn and HCFeMn SAF tapping flow model results using parameter values from Table 16, for a slag fraction (SR) of 0.5, slag height at 0 m above the taphole (effective viscosity with model by Pal (2001)).

Parameter	Symbol	Units	SiMn process			HCFeMn process			
			SiMn A	SiMn B	SiMn C	HCFeMn A	HCFeMn B	HCFeMn C	HCFeMn D
Slag density	ρ_{slag}	kg.m^{-3}	2540	2531	2476	2992	2676	2852	2922
Slag viscosity	μ_{slag}	Pa.s	0.74	0.92	0.74	1.54	1.27	0.64	1.44
Mixed fluid density	ρ_{avg}	kg.m^{-3}	3495	3490	3463	4302	4144	4232	4267
Mixed fluid viscosity	μ_{avg}	Pa.s	1.98	2.46	1.98	4.11	3.39	1.72	3.85
Reynolds nr.	Re		40	26	40	12	16	65	13
Friction factor	f		0.448	0.664	0.451	1.441	1.033	0.295	1.277
Coke bed pressure drop	ΔP_1	Pa	14 756	14 765	14 756	14 775	14 772	14 741	14 774
Taphole pressure drop	ΔP_2	Pa	244	235	244	225	228	259	226
Total pressure drop	ΔP_{tot}	Pa	15 000	15 000	15 000	15 000	15 000	15 000	15 000
Fluid flow velocity	u	m.s^{-1}	0.228	0.184	0.228	0.110	0.133	0.263	0.118
Fluid volumetric rate	V	m^3.s^{-1}	0.0018	0.0014	0.0018	0.0009	0.0010	0.0021	0.0009
Fluid mass rate	M	kg.s^{-1}	6.3	5.0	6.2	3.7	4.3	8.7	3.9
Laminar flow entry length	x_e	m	0.121	0.078	0.119	0.035	0.049	0.195	0.039

Table 23 SiMn and HCFeMn SAF tapping flow model results using parameter values from Table 17, for a slag fraction (SR) of 1, slag height at 0 m and metal at 0 m above the taphole (effective viscosity with model by Pal (2001).

Parameter	Symbol	Units	SiMn process			HCFeMn process			
			SiMn A	SiMn B	SiMn C	HCFeMn A	HCFeMn B	HCFeMn C	HCFeMn D
Slag density	ρ_{slag}	kg.m^{-3}	2540	2531	2476	2992	2676	2852	2922
Slag viscosity	μ_{slag}	Pa.s	0.74	0.92	0.74	1.54	1.27	0.64	1.44
Mixed fluid density	ρ_{avg}	kg.m^{-3}	2540	2531	2476	2992	2676	2852	2922
Mixed fluid viscosity	μ_{avg}	Pa.s	0.74	0.92	0.74	1.54	1.27	0.64	1.44
Reynolds nr.	Re		208	135	203	57	75	311	64
Friction factor	f		0.122	0.166	0.124	0.330	0.262	0.095	0.300
Coke bed pressure drop	ΔP_1	Pa	14 657	14 699	14 660	14 746	14 734	14 605	14 741
Taphole pressure drop	ΔP_2	Pa	343	301	340	254	266	395	259
Total pressure drop	ΔP_{tot}	Pa	15 000	15 000	15 000	15 000	15 000	15 000	15 000
Fluid flow velocity	u	m.s^{-1}	0.606	0.489	0.606	0.293	0.355	0.699	0.313
Fluid volumetric rate	V	m^3.s^{-1}	0.0048	0.0038	0.0048	0.0023	0.0028	0.0055	0.0025
Fluid mass rate	M	kg.s^{-1}	12.1	9.7	11.8	6.9	7.5	15.6	7.2
Laminar flow entry length	x_e	m	0.624	0.404	0.609	0.171	0.224	0.934	0.191

The above calculations were repeated using the rule of mixtures approach to estimate the mixed fluid viscosity. Results for the different slags considered are illustrated in Figure 46 and Figure 47 for a slag fraction (SR) of 0.5 and various slag heights above the taphole between 0 and 0.5 m. Results for a slag fraction (SR) of 1 are not repeated, since the fraction of metal is zero and the effective viscosity equal to that of the slag, resulting in the same flow rates as were presented in Table 21 and Table 23.

Compared to the model by Pal (2001), the rules of mixture approach resulted in lower viscosities being estimated for the mixtures with lower slag fractions. This resulted in the total rates estimated for slag fractions of 0.5 being significantly higher than those reported above. Only for some of the slags with higher viscosities at slag heights of 0 m above the taphole were the total rates estimated below the

range of typical rates derived from Olsen *et al.* (2007). Despite the higher flow rates estimated, flow was estimated to remain laminar in most cases. Turbulent flow was obtained for only slag HCFeMn C, with the lowest viscosity, at slag height of 0.5 m.
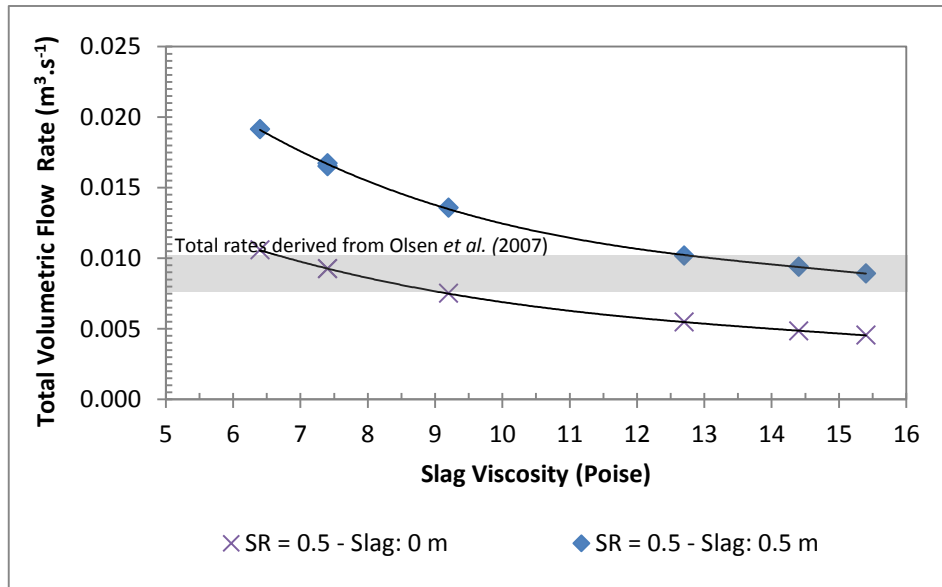
Figure 46 Total volumetric flow rate as a function of viscosity for typical SiMn and HCFeMn slags, for slag heights of 0 and 0.5 m, and slag fractions (SR) of 0.5 and 1 (effective viscosity with rule of mixtures).
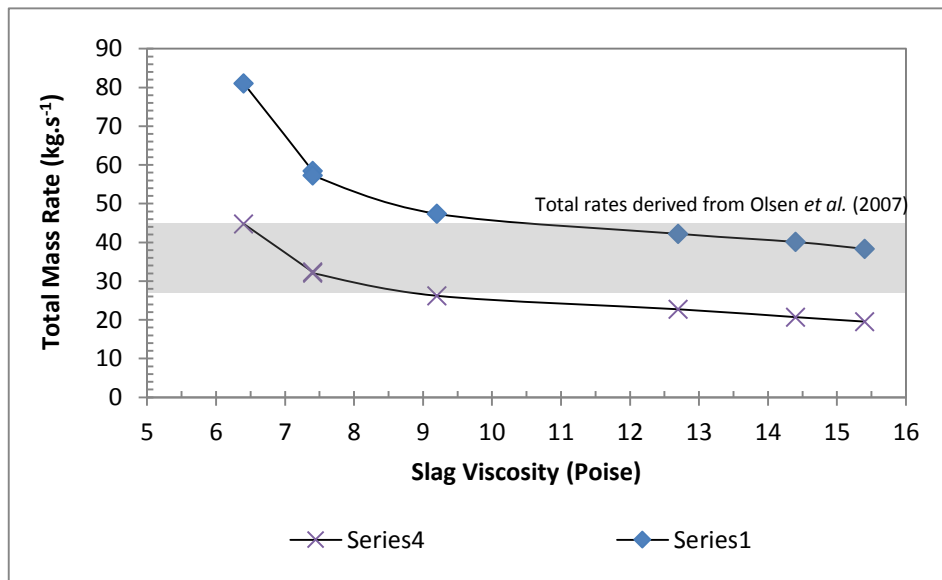
Figure 47 Total mass flow rate as a function of viscosity for typical SiMn and HCFeMn slags, for slag heights of 0 and 0.5 m, and slag fractions (SR) of 0.5 (effective viscosity with rule of mixtures).

6.2.2 Varying slag-metal ratio

The effect of varying the slag fraction was further investigated for the case where the slag height was at 0.5 m above the taphole and the metal at 0 m. The model by Pal (2001) was first used to estimate the mixed fluid effective viscosity, selecting slag as the continuous phase containing dispersed metal at fractions up to 0.5. The total volumetric flow rates estimated are illustrated in Figure 48 as functions of

83

the volumetric slag fraction (SR). The results essentially vary between those listed in Table 20 (for SR = 0.5) and those in Table 21 (for SR = 1). Similarly to what has been established before, the mixed fluid viscosity was estimated to decrease with the increasing slag fraction, resulting in higher flow rates. As with the iron blast furnace model, slag fractions from around 0.5 were considered. Pal (2001) indicates that this is the value from which the average mixed fluid viscosity equation is valid (Equation [39]) for emulsions with similar viscosity ratios. Figure 48 shows that only some of the estimated total flow rates were within the range of rates derived from Olsen *et al.* (2007).

Using the simple rule of mixtures to estimate the average viscosity resulted in viscosity decreasing with increasing metal fraction, and therefore tapping rates increasing relative to the values at a slag fraction of 1 (Figure 49). For slag fractions above 0.5, the total tapping rates were estimated to be mostly within or above the range of typical rates derived from Olsen *et al.* (2007). At slag fractions below 0.5, the total tapping rates were estimated to be significantly higher, as would be expected for mixtures containing predominantly low-viscosity metal.

Figure 48 Total volumetric flow rate as a function of the volumetric slag fraction for typical SiMn and HCFeMn slags, for a slag height 0.5 m (effective viscosity with model by Pal (2001)).

Figure 49 Total volumetric flow rate as a function of the volumetric slag fraction for typical SiMn and HCFeMn slags, for a slag height 0.5 m (effective viscosity by the rule of mixtures).

6.2.3 Varying taphole length and diameter

Results presented previously (Table 20 to Table 23) indicated that the estimated pressure drops over the taphole are small in relation to those over the coke bed. To establish the sensitivity of the estimated flow rate to each of the taphole dimensions, the taphole diameter was varied around the baseline value of 0.1 m and the length of 0.6 m. As a basis, the slag height was set at 0.5 m above the taphole, the metal height at 0 m, and the volumetric slag fraction (SR) at 1, this being the case for which the highest flow rates and pressure drops across the taphole were obtained (Table 21). Estimated volumetric flow rates are shown in Figure 50 and Figure 51, together with the range of typical flow rates derived from Olsen *et al.* (2007), which in this case are only the slag rates, since the slag fraction was set at 1 as basis for this model application.

Figure 50 illustrates that the tapping flow rates were estimated to increase significantly with taphole diameter in a linear fashion. A doubling in the taphole diameter from 0.075 to 0.15 m resulted in the doubling in the estimated flow rates. Flow rates can therefore be expected to increase by this amount in relation to taphole wear. The estimated Reynolds numbers increased for the taphole diameters considered, but remained well below 2100, maintaining the laminar flow estimation. For the scenarios where the volumetric flow rates were estimated to be greater than around 0.007 $m^3.s^{-1}$, the entry lengths for developed laminar flow were found to be greater than the taphole length of 0.6 m.

Figure 51 illustrates the estimated tapping flow rates as a function of taphole length. Small decreases of approximately 6% were obtained by increasing the taphole length from 0.3 to 3 m.

Figure 50 Total volumetric flow rate as a function of the taphole diameter for typical SiMn and HCFeMn slags, for a slag height 0.5 m and volumetric slag fraction of 1.
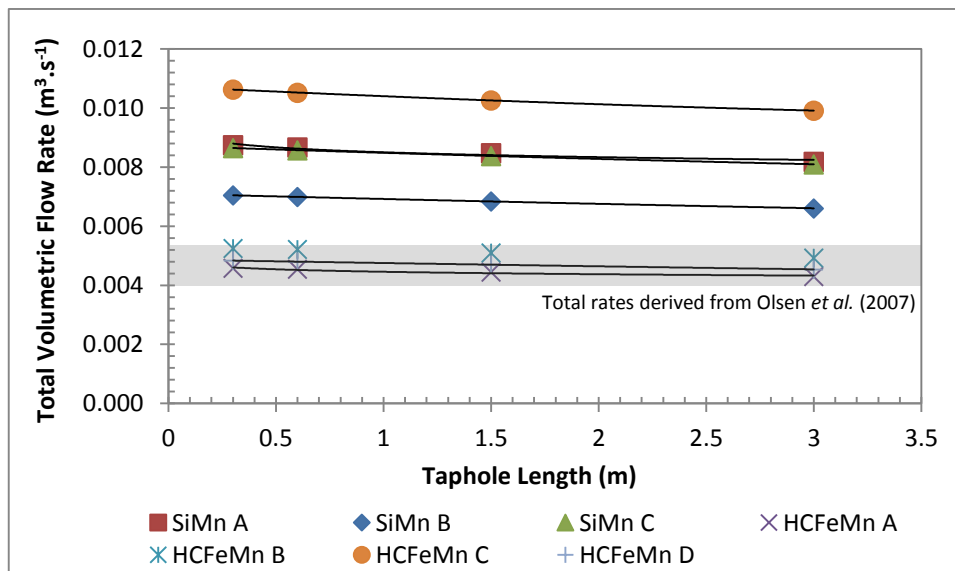
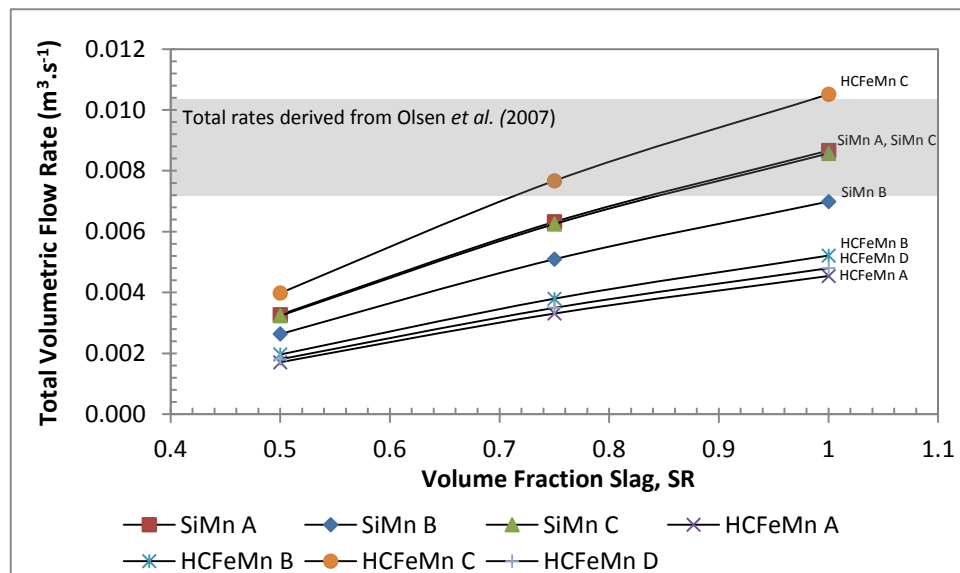
Figure 51 Total volumetric flow rate as a function of the taphole length for typical SiMn and HCFeMn slags, for a slag height 0.5 m and volumetric slag fraction of 1.

6.2.4 Varying coke bed void fraction and particle diameter

Relationships can be derived between the void fraction and the particle diameter for closely packed beds. Such a relationship was, however, not investigated for the coke bed of interest here, and the sensitivities of flow were determined separately for the variation in the coke bed void fraction and particle diameter. For this investigation, the slag height was set at 0.5 m above the taphole and the metal height at 0 m, with the slag fraction in the tapped stream as 1 (similar to results presented in Table 21). Estimated volumetric flow rates are shown in Figure 52 and Figure 53, together with the range of typical flow rates derived from Olsen *et al.* (2007), which in this case are only the slag rates, since the slag fraction was set at 1 as basis for this model application.

Figure 52 illustrates the flow rates to increase significantly with increasing coke bed void fraction, as can be observed during the tapping process as coke particles are consumed. Figure 53 illustrates the estimated tapping flow rates to decrease almost linearly with respect to coke bed particle diameters decreasing in size as coke particles are consumed during the tapping process. The Reynolds numbers were estimated to remain mostly below 2100, indicating laminar flow. Only for slag HCFeMn C, with the lowest viscosity, did the Reynolds numbers increase above 2100 from void fractions above 0.41, which indicated turbulent flow. The pressure drop over the taphole was estimated to increase for the higher flow rates, but remained small in relation to that over the coke bed.

Considering the void fraction and particle diameter separately, the above results indicate that these parameters have opposing effects on flow rate should the coke bed void fraction increase during the tapping process and particle diameter decrease. A scenario was also modelled where the coke bed was set to consist of finer particles, with a smaller particle diameter and larger void fraction. A baseline value of 0.3 for the coke bed void fraction was used, and 0.05 m for particle diameter, in line with the "coarse coke bed" of Kadkhodabeigi (2011). In this work a layer of "fine coke bed" was also defined, said to exist under the electrodes and having a larger void fraction of 0.5 and smaller particle diameter of 0.03 m (Kadkhodabeigi 2011). The results in Table 24 were obtained by changing these parameters simultaneously in relation to those for the "fine coke bed", with the slag fraction set at 1 and the slag height at 0.5 m above taphole. These results for the "fine coke bed" can be directly compared to those in Table 21, representing the "coarse coke bed" with the other conditions being the same. With significantly increased flow rates estimated for the "fine coke bed", it is evident that the increase in the void fraction from 0.3 to 0.5 is the major factor in obtaining higher flow rates. The decrease in particle diameter from 0.05 to 0.03 m would cause the flow rate to decrease somewhat.
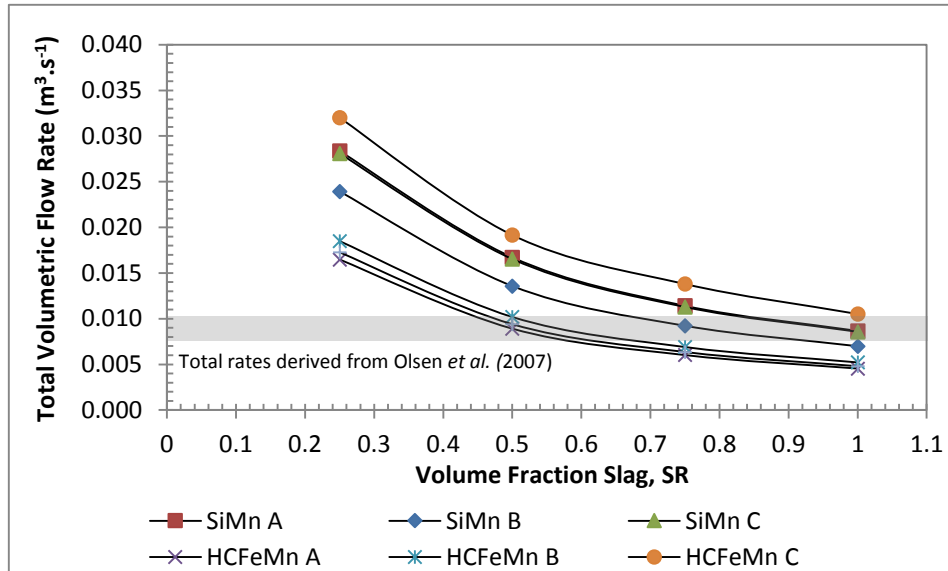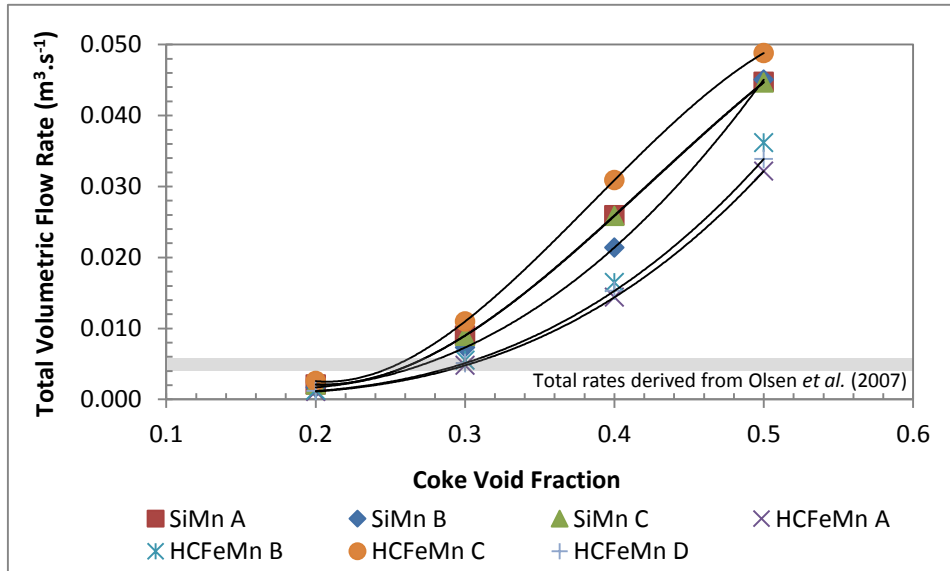
Figure 52 Total volumetric flow rate as a function of the coke bed void fraction for typical SiMn and HCFeMn slags, for a slag height 0.5 m and volumetric slag fraction of 1.
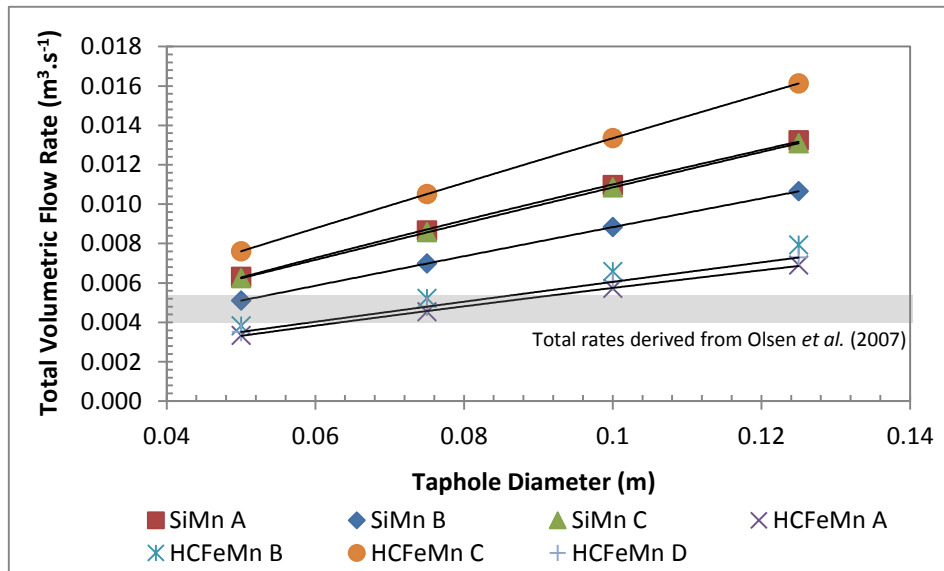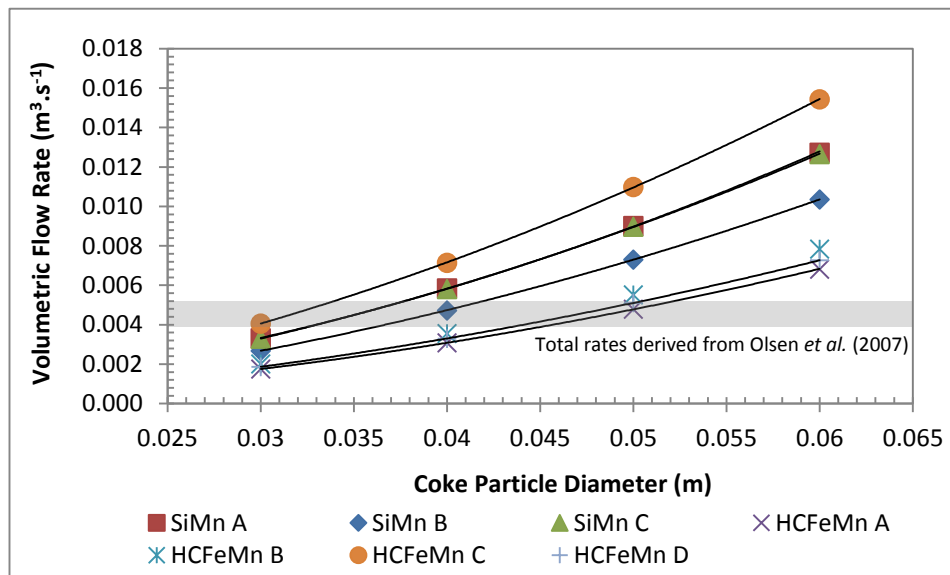

Figure 53 Total volumetric flow rate as a function of the coke bed particle diameter for typical SiMn and HCFeMn slags, for a slag height 0.5 m and volumetric slag fraction of 1.

Table 24 SiMn and HCFeMn SAF tapping flow model results for a coke bed void fraction of 0.5 and particle radius of 0.015 m, with slag height at 0.5 m above the taphole and metal at 0 m, and slag ratio SR = 1.

Parameter	Symbol	Units	SiMn process			HCFeMn process			
			SiMn A	SiMn B	SiMn C	HCFeMn A	HCFeMn B	HCFeMn C	HCFeMn D
Slag density	ρ_{slag}	kg.m⁻³	2774	2795	2745	3327	3017	3127	3317
Slag viscosity	μ_{slag}	Pa.s	0.74	0.92	0.74	1.54	1.27	0.64	1.44
Mixed fluid density	ρ_{avg}	kg.m⁻³	2774	2795	2745	3327	3017	3127	3317
Mixed fluid viscosity	μ_{avg}	Pa.s	0.74	0.92	0.74	1.54	1.27	0.64	1.44
Reynolds nr.	Re		1251	836	1232	400	503	1941	453
Friction factor	f		0.042	0.053	0.043	0.081	0.071	0.033	0.076
Coke bed pressure drop	ΔP_1	Pa	24 688	25 331	24 587	28 519	26 899	25 423	28 343
Taphole pressure drop	ΔP_2	Pa	3905	3365	3864	2783	2884	4899	2911
Total pressure drop	ΔP_{tot}	Pa	28 593	28 696	28 451	31 302	29 783	30 322	31 253
Fluid flow velocity	u	m.s⁻¹	3.336	2.753	3.323	1.852	2.118	3.972	1.968
Fluid volumetric rate	V	m³.s⁻¹	0.0262	0.0216	0.0261	0.0145	0.0166	0.0312	0.0155
Fluid mass rate	M	kg.s⁻¹	72.7	60.4	71.6	48.4	50.2	97.6	51.3
Laminar flow entry length	x_e	m	3.752	2.509	3.697	1.200	1.509	5.823	1.360

7   Summary

Results have been presented for the modelling of slag physicochemical properties, and the application thereof in the modelling of flow through the coke bed and taphole. The results are summarised as follows, addressing the most important findings.

7.1   Slag physicochemical properties

The operational practices followed, in combination with other factors such as ore composition and operating temperature, affect the chemical composition of the final slags tapped from the HCFeMn and SiMn smelting processes. Slag physicochemical properties such as viscosity and thermal conductivity, which are dependent on the slag temperature and chemical composition, influence the behaviour of fluid flow and heat transfer.

For the purpose of evaluating the influence of slag chemical composition on tapping, typical slag compositions were selected that represent the most common operating practices. Models for each relevant physicochemical property were researched and applied, and the influences of chemical composition and temperature for each were evaluated. Properties of the slags were calculated and compared at typical process temperatures of 1400°C for HCFeMn slags and 1600°C for SiMn slags.

The observations for each slag property relevant to the HCFeMn and SiMn slag compositions considered are summarised as follows:

- *Viscosity*: SiMn slags are operated above their liquidus temperatures, with no precipitated solids but a higher SiO_2 content that contributes to increased viscosity. HCFeMn slags are operated close to or below their liquidus temperatures, with precipitated solids increasing the viscosity. Overall, HCFeMn slags have higher viscosities than SiMn slags. For SiMn slags, viscosity decreases with increased basicity (due to network-breaking monoxides). In the case of HCFeMn slags, viscosity increases with increased basicity due to increased amounts of dispersed solids.

- *Thermal conductivity*: The thermal conductivities of SiMn slags are significantly higher than those of HCFeMn slags at a specific temperature. Because the thermal conductivity decreases with temperature around the typical operating temperatures, thermal conductivities of SiMn slags are only slightly higher than those of HCFeMn slags at the respective typical operating temperatures. For SiMn slags the thermal conductivities decrease slightly with increased basicity (decreased polymerisation), while for HCFeMn slags the thermal conductivities increase very slightly with increased basicity (increased liquidus temperatures).

- *Density*: The densities of SiMn slags are significantly lower than those of HCFeMn slags, as a result of thermal expansion and the difference in baseline temperatures used (1400°C for

HCFeMn slags and 1600°C for SiMn slags). The densities of HCFeMn slags (containing more monoxides) are also higher due to the lower partial molar volumes of the monoxides (especially MnO) compared with SiMn slags. For the same reason, density increases with basicity, while it decreases with temperature due to thermal expansion.

- *Heat capacity*: The heat capacities of liquid slags were found to be higher than those of solid slags. This is a contributing factor to the slightly higher heat capacities of the SiMn slags compared with the HCFeMn slags, due to the small amounts of precipitated solids in the latter.

7.2   Tapping flow modelling

Tapping flow models were formulated to evaluate the flow of slag and metal through the tapholes of SAFs producing HCFeMn and SiMn under typical operating conditions and using the modelled physicochemical properties. An analytical flow modelling approach was followed, based on work by Iida *et al.* (2008), who modelled fluid flow through the coke bed and taphole of a blast furnace using pressure drop equations. Improvements to this model were formulated and applied to the system under investigation. The observations for each of the specific aspects considered are summarised as follows:

- *Basic model application for an iron blast furnace*: Results from the application of the iron blast furnace model from Iida *et al.* (2008) validated the model application, with estimated taphole flow rates for varying coke bed fluid path lengths matching those reported. The pressure drop over the coke bed was found to be dominant in the model, with the path length assumed to strongly influence the estimated flow rate. The Reynolds numbers calculated with the estimated results indicated turbulent flow for the conditions considered.

- *Improved model application for an iron blast furnace*: The improved model was applied with the same set of iron blast furnace model parameters from Iida *et al.* (2008), estimating only a single results point with the model being independent of the coke bed fluid path length. The taphole fluid flow rate was similar to that obtained previously for a baseline coke bed fluid path length of 0.08 m. It was concluded that flow that would develop into laminar flow over the greater part of the taphole length, in contrast to the turbulent flow that was obtained using the basic model.

- *Viscosity variation with fractions of slag and metal tapped*: The mixed fluid viscosity was estimated using a model by Pal (2001). For this investigation the fluids were assumed to be sufficiently finely dispersed in one another, with slag selected as the continuous phase and metal as the dispersed phase in the emulsion. With this model, the effective viscosity of slag-metal mixtures was found decrease with the fraction of slag tapped (less dispersed metal). Slag fractions of 0.5 to 1 were considered, with the results indicating that the assumptions by Pal (2001) associated with the application of the mixed fluid viscosity are less likely to be valid for this system at lower slag fractions. Using the simple rules of mixture approach to estimate the

91

mixed fluid viscosity, it was possible to estimate viscosities over the full range of fractions from 0 to 1, and viscosity was found to decrease with the fraction of metal tapped.

- *Variation of slag-metal ratio in iron blast furnace tapping*: The tapping rate was estimated to generally increase with slag fraction as the mixed fluid viscosity decreases. Using the model by Pal (2001) to estimate the mixed fluid viscosity, laminar flow was estimated for slag fractions of 0.5 up to 0.53, for which the pressure drop over the coke bed was found dominant. This is in agreement with the work by Iida *et al.* (2008). From slag fractions of around 0.68 the pressure drop over the taphole became dominant, and turbulent flow was estimated. For slag fractions between 0.53 and 0.68 a discontinuity was found to exist in the estimated flow rates as a result of differences in laminar and turbulent flow friction factors for situations where the Reynolds numbers are close to 2100. When using the rule of mixtures to estimate the mixed fluid viscosity, turbulent flow was obtained over the slag fraction range of 0 to 1. Estimated flow rates agreed with those obtained using the viscosity model by Pal (2001), and were found to decrease up to a slag fraction of around 0.5, from which point the flow rate remained almost constant with increasing slag fractions.

- *Baseline SiMn and HCFeMn tapping*: A baseline was established for modelling the tapping of SiMn and HCFeMn slag and metal from a SAF, varying the slag fraction between 0.5 and 1 and the slag height above the taphole between 0 and 0.5 m. The highest slag flow rates were obtained for the greatest slag height above the taphole, with values comparable to typical values from the literature. Flow was estimated to be laminar in most cases for varying slag fractions and height, and the pressure drop dominant over the coke bed. Using the model by Pal (2001) to estimate mixed fluid viscosities resulted in lower flow rates being estimated at the lower slag fractions due to the increased effective viscosities, with total rates below typical tapping rates in most cases. The simple rule of mixtures approach resulted in lower viscosities being estimated at the lower slag fractions (the mixture containing predominantly metal), and significantly increased tapping rates that were mostly within or above the typical range of tapping rates.

- *Taphole diameter and length dependency*: For the scenario of tapping only slag when the height is at 0.5 m above the taphole, the volumetric flow rate was found to be highly sensitive to the taphole diameter. Doubling the taphole diameter from 0.075 to 0.15 m resulted in the doubling of the estimated flow rates. Flow rates were, however, estimated to decrease slightly with taphole length. In all the cases the flow remained laminar.

- *Coke bed void fraction and particle diameter*: The sensitivity was tested separately for the coke bed void fraction and particle diameter, ignoring at first the relationships between these parameters. Considering again the scenario of tapping only slag when the height is at 0.5 m

92

above the taphole, it was found that the volumetric flow rate would increase significantly with the coke bed void fraction, and also increase with the coke bed particle diameter. However, for a bed of finer coke particles with a larger void fraction and a smaller diameter, the flow rates were estimated to be higher, with the effect of the void fraction being dominant. Flow remained laminar in most cases, becoming turbulent only for HCFeMn C from void fractions of around 0.41.

8   Conclusions

A study was conducted to investigate the flow behaviour when tapping manganese-bearing slags from SAFs producing HCFeMn and SiMn, and determine the factors that affect tapping behaviour. Taking typical operating practices into account, slag physicochemical properties were modelled for typical slag compositions, and subsequently applied in a tapping flow model formulated to include the coke bed and taphole.

A model from the literature (Iida *et al.* 2008) for flow through the coke bed and taphole indicated turbulent flow through the taphole of an iron blast furnace when tapping a mixed stream with equal volumetric amounts of slag and metal. A tapping model was subsequently developed containing some corrections and improvements, and which modelled spherical-radial flow through the coke bed as being independent of the length of the fluid path through the coke bed. Applied using the same set of blast furnace model parameters, the improved model estimated flow rates to be of the same order as those reported by Iida *et al.* (2008), but estimated turbulent flow for mixtures of lower estimated viscosities.

The modelling work showed that significant differences can be expected in the flow rate behaviour of slag and metal from SiMn and HCFeMn processes, and for the different practices followed in the HCFeMn processes. The differences were found to be largely dependent on the physicochemical properties of the slags being tapped, as determined by their chemical composition and temperature, as well as on the fraction of slag tapped and physical properties of the taphole and coke bed.

The improved tapping flow model was applied with conditions resembling typical SiMn and HCFeMn processes, with the focus on tapping a stream of slag only. Notable differences were found in the flow rates estimated for the different slags considered, with the results being comparable to those reported by others (Kadkhodabeigi 2011). Generally, SiMn slags were found to have the lowest viscosities, resulting in higher tapping flow rates being achieved. The results indicate that the largest pressure drop exists over the coke bed, and under the base case conditions the pressure drop across the coke bed is approximately double that over the taphole.

Mixed fluid viscosities estimated with the model by Pal (2001) were found to increase with the amount of the dispersed metal phase, i.e. viscosity increased when tapping lower slag fractions. This, however, is based on the assumption that a sufficiently finely dispersed emulsion of slag and metal is formed, which is difficult to verify and leads to greater uncertainty in the results for lower slag fractions tapped. At slag fractions less than approximately 0.5 the mixtures will contain mostly metal of a lower viscosity. Estimated tapping rates are more in line with the expected rates assuming separated flow and using the rule of mixtures approach to calculate the mixed fluid viscosity, resulting in lower mixed fluid viscosities and higher total tapping rates.

94

It was also established that the taphole diameter has a significant effect on the tapping flow rates, and to a lesser extent the taphole length, with flow in both cases expected to remain laminar. The coke bed properties were also found to significantly affect the flow, with void fraction having a greater effect than particle diameter. For a single case, it was estimated that a coke bed with finer particles and a higher void fraction would be more permeable, with higher flow rates achievable.

9   References

- AMERICAN SOCIETY FOR TESTING AND MATERIALS. 1999. *Specification for Ferroalloys. 1999 Annual Book of ASTM Standards,* Sect. 1, vol. 01.02 Ferrous Casting: Ferroalloys. ASTM, Philadelphia, PA.

- AUNE, R.E., HAYASHI, M., NAKAJIMA, K., AND SEETHARAMAN, S. 2002. Thermophysical properties of silicate slags. *Journal of Metals*, vol. 54, no. 11, pp. 62–69.

- BALE, C.W., BÉLISLE, E., CHARTRAND, P., DECTEROV, S.A., ERIKSSON, G., HACK, K., JUNG, I.H., KANG, Y.B., MELANÇON, J., PELTON, A.D., ROBELIN, C., AND PETERSEN, S. 2009. FactSage thermochemical software and databases - Recent developments. *Calphad*, vol. 33, no. 2, pp. 295–311.

- BENESCH, B., KUTHNICKI, R., AND JAWORSKI, M. 1984. *Archiv Hutnick*, vol. 29, pp. 277-283.

- BIRD, R.B., STEWART, W.E., AND LIGHTFOOT, E.N. 2007. *Transport Phenomena*. 2nd edn. John Wiley & Sons. pp. 182.

- BJÖRKVALL, J., SICHEN, D., AND SEETHARAMAN, S. 2001. Thermodynamic model calculations in multicomponent liquid silicate systems. *Ironmaking and Steelmaking*, vol. 28, no. 3, pp. 250–257.

- BRUN, H. 1982. Development of refractory linings for electric reduction furnaces producing Mn alloys at Elkem A/S PEA Plant, Porsgrunn, Norway. *Journal of the Institute of Refractories Engineers*, pp. 12.

- CHUBINIDZE, T.A. 1974. *Teoriya i Praktika Poluch i Primeneniya Kompleks Ferrosplavov*, pp. 31-35.

- CRAWLEY, A.F. 1974. Densities of liquid metals and alloys. *International Metallurgical Reviews*, vol. 19, no. 1, pp. 32-48.

- DECTEROV, S.A., GRUNDY, A.N., AND PELTON, A.D. 2009. A model and database for the viscosity of molten slags. *Proceedings of the Eighth International Conference on Molten Slags, Fluxes and Salts*, Santiago, Chile, 18-21 January 2009. pp. 423-431.

- DE KIEVIT, A., GANGULY, S., DENNIS, P., AND PIETERS, T. 2004. Monitoring and control of furnace 1 freeze lining at Tasmanian Electro-metallurgical Company. *INFACON X, Proceedings of the Tenth International Ferroalloys Congress*, Cape Town, South Africa, 1-4 February 2004. South African Institute of Mining and Metallurgy, Johannesburg. pp. 477-487.

- DESAI, B. AND LENKA, S. 2007. Quantification of blast furnace hearth drainage parameters through physical model study. *Ironmaking and Steelmaking*, vol. 34, no. 3, pp. 269-271.

- DUNCANSON, P.L. AND TOTH, J.D. 2004. The truths and myths of freeze lining technology for submerged arc furnaces. *INFACON X, Proceedings of the Tenth International Ferroalloys Congress*, Cape Town, South Africa, 1-4 February 2004. South African Institute of Mining and Metallurgy, Johannesburg. pp. 488–499.

- ENGH, T.A. 1975. Viskositetsmålinger I Slagger, Metallurgisk Institutt, NTH, Norway.

- ERIKSSON, R., HAYASHI, M., AND SEETHARAM, S. 2003. Thermal diffusivity of liquid silicate melts. *International Journal of Thermophysics*, vol. 24, no. 3, pp. 785-797.

- GHAJAR, A.J. AND MADON, K.F. 1992. Pressure drop measurements in the transition region for a circular tube with three different inlet configurations. *Experimental Thermal and Fluid Science*, vol. 5, pp. 129-135.

- GLASER, B., MA, L., AND SICHEN, D. 2013. Determination of experimental conditions for applying hot wire method to thermal conductivity of slag. *Steel Research International*, vol. 84, no. 7, pp. 649-663.

- HABASHI, F. 1997. *Handbook of Extractive Metallurgy*. Vol. 1, Wiley-VCH, pp. 420–434.

- HAYASHI, M., ISHII, H., SUSA, M., FUKUYAMA, H., AND NAGATA, K. 2001. Effect of ionicity of nonbridging oxygen ions on thermal conductivity of molten alkali silicates. *Physics and Chemistry of Glasses*, vol. 42, no. 1, pp. 6-11.

- HEARN, M.H., DZERMEJKO, A.J., AND LAMONT, P.H. 1998. "Freeze" lining concepts for improving submerged arc furnace lining life and performance. *INFACON VIII, Proceedings of the Eighth International Ferroalloys Congress*, Beijing, China, 7-10 June 1998. Southern African Institute of Mining and Metallurgy, Johannesburg. pp. 401-426.

- IIDA, M., OGURA, K., AND HAKONE, T. 2008. Analysis of drainage rate variation of molten iron and slag from blast furnace during tapping. *ISIJ International*, vol. 48, no. 3, pp. 412-419.

- JIMBO, I. AND CRAMB, A.W. 1993. The density of liquid iron-carbon alloys. *Metallurgical Transactions B*, vol. 24, no. 1, pp. 5-10.

- KADKHODABEIGI, M., TVEIT, H., AND JOHANSEN, S.T. 2010. Modelling the tapping process in submerged arc furnaces used in high silicon alloys production. *ISIJ International*, vol. 51, no. 2, pp. 193-202.

- KADKHODABEIGI, M. 2011. *Modeling of Tapping Processes in Submerged Arc Furnaces*. PhD thesis, NTNU, Trondheim, Norway.

- KONDRATIEV, A., JAK, E., AND HAYES, P.C. 2002. Predicting slag viscosities in metallurgical systems. *Journal of the Minerals, Metals & Materials Society*, vol. 54, no. 11, pp. 41–45.

- KOZAKEVITCH, P. 1949. *Revue de Metallurgie*, vol. 46, pp. 572-582.

- LIENHARD, J.H. IV AND LIENHARD, J.H. V. 2006. *A Heat Transfer Textbook.* 3rd edn, Phlogiston Press, Cambridge MA.

- LEU, C. 2010. *Computation Fluid Dynamic Simulation of Blast Furnace Hearth Drainage.* MS thesis, Purdue University, Hammond, Indiana.

- MILLS, K.C. AND KEENE, B.J. 1987. Physical properties of BOS slags. *International Materials Reviews*, vol. 32, pp. 1-23.

- MILLS, K.C., YUAN, L., AND JONES, R.T. 2011. Estimating the physical properties of slags. *Journal of the Southern African Institute of Mining and Metallurgy*, vol. 111, pp. 649–658.

- MØLNÅS, H. 2011. *Compatibility study of carbon-based refractory utilised in silicomanganese production furnaces.* MS thesis, Norwegian University of Science and Technology, Trondheim, Norway.

- NASCH, P. M. AND STEINEMANN, S.G. 1995. Density and thermal expansion of molten manganese, iron, nickel, copper, aluminum and tin by means of the gamma-ray attenuation technique. *Physics and Chemistry of Liquids*, vol. 29, no. 1, pp. 43-58.

- NISHIOKA, K., MAEDA, T., AND SHIMIZU, M. 2005. A three-dimensional mathematical modelling of drainage behavior in blast furnace hearth. *ISIJ International*, vol. 45, no. 5, pp. 669-676.

- OLSEN, S.E., TANGSTAD, M., AND LINDSTAD, T. 2007. *Production of Manganese Ferroalloys.* Tapir Academic Press, Trondheim.

- PAL, R. 2001. Novel viscosity equations for emulsions of two immiscible liquids. *Journal of Rheology*, vol. 45, no. 2, pp. 509-520.

- ROSCOE, R. 1952. The viscosity of suspensions of rigid spheres. *British Journal of Applied Physics*, vol. 3, pp. 267–269.

- SEETHARAMAN, S., MUKAI, K., AND SICHEN, D. 2004. Viscosities of slags – an overview. *Proceedings of the Seventh International Conference on Molten Slags, Fluxes and Salts*, Cape Town, South Africa, 25-28 January 2004. South African Institute of Mining and Metallurgy, Johannesburg. pp. 31-42.

- SHAO, L. 2013. *Model-based Estimation of Liquid Flows in the Blast Furnace Hearth and Taphole.* D.Tech thesis, Åbo Akademi University, Turku, Finland.

- *Slag Atlas*. 1995. 2nd edn. Verlag Stahleisen, Dusseldorf.

- STEENKAMP, J.D., TANGSTAD, M., AND PISTORIUS, P.C. 2011. Thermal conductivity of solidified manganese-bearing slags – A preliminary investigation. *Proceedings of the Southern African Pyrometallurgy Conference*, Johannesburg, South Africa, 6-9 March 2011. Southern African Institute of Mining and Metallurgy, Johannesburg. pp. 327–343.

- TANG, K. AND TANGSTAD, M. 2007. Modelling viscosities of ferromanganese slags. *INFACON XI, Proceedings of the Eleventh International Ferroalloys Congress*, New Delhi, India, 18-21 February 2007. Macmillan India, Delhi, pp. 344-357.

- VERSTEEG, H.K. AND MALALASEKERA, W. 2007. *An Introduction to Computational Fluid Dynamics – The Finite Volume Method*. 2nd edn. Prentice Hall, Englewood Cliffs, New Jersey.

- ZHANG, G. AND CHOU, K. 2010. Model for evaluating density of molten slag with optical basicity. *Journal of Iron and Steel Research International*, vol. 17, no. 4, pp. 1-4.

10 Declaration on plagiarism

<div align="center">

UNIVERSITY OF PRETORIA

Faculty of Engineering, the Built Environment and Information Technology

Department of Materials Science and Metallurgical Engineering

</div>

The University places great emphasis upon integrity and ethical conduct in the preparation of all written work submitted for academic evaluation.

While academic staff teach you about systems of referring and how to avoid plagiarism, you too have a responsibility in this regard. If you are at any stage uncertain as to what is required, you should speak to your lecturer before any written work is submitted.

You are guilty of plagiarism if you copy something from a book, article or website without acknowledging the source and pass it off as your own. In effect you are stealing something that belongs to someone else. This is not only the case when you copy work word-by-word (verbatim), but also when you submit someone else's work in a slightly altered form (paraphrase) or use a line of argument without acknowledging it. You are not allowed to use another student's past written work. You are also not allowed to let anybody copy your work with the intention of passing it off as his/her work.

Students who commit plagiarism will lose all credits obtained in the plagiarised work. The matter may also be referred to the Disciplinary Committee (Students) for a ruling. Plagiarism is regarded as a serious contravention of the University's rules and can lead to expulsion from the University.

The declaration which follows must be appended to all written work submitted for Literature Survey NSC412 and NSC421. No written work will be accepted unless the declaration has been completed and attached.

I (full names)   : Jacques Muller

Student number : 99029473

Topic of work   : Pyrometallurgical modelling

Declaration

1.   I understand what plagiarism is and am aware of the University's policy in this regard.
2.   I declare that this report is my own original work. Where other people's work has been used (from a printed source, internet or any other source), this has been properly acknowledged and referenced in accordance with departmental requirements.
3.   I have not used another student's past written work to hand in as my own.
4.   I have not allowed, and will not allow, anyone to copy my work with the intention of passing it off as his or her own work.

Signature:

Date: 2015/03/09

<div align="center">

© University of Pretoria

</div>